

Development of Liquid Propellant Tanks for a Suborbital Launch Vehicle

Vulinhlanhla Salvation Mchunu

Submitted in fulfilment of the academic requirements for the degree of Master of Science in
Mechanical Engineering, College of Agriculture, Engineering and Science, University of
KwaZulu-Natal.

Durban, South Africa

July 2022

Supervisor: Dr Jean-Francois Pitot de la Beaujardiere

Co-Supervisor: Prof Michael J. Brooks

Declaration 1 – Plagiarism

I, Vulinhlanhla Salvation Mchunu, declare that:

- i. The research reported in this dissertation/thesis is my original work, except where otherwise indicated.
- ii. This dissertation/thesis has not been submitted for any degree or examination at any other university.
- iii. This dissertation/thesis does not contain other persons' data, pictures, graphs, or information unless expressly acknowledged as being sourced from other persons.
- iv. This dissertation/thesis does not contain other persons' writing unless specifically acknowledged as being sourced from other researchers. Where other written sources have been quoted, then:
 - a. Their words have been re-written, but the general information attributed to them has been
 - b. referenced;
 - c. Where their exact words have been used, their writing has been placed inside quotation marks and referenced.
- v. Where I have reproduced a publication of which I am an author, co-author, or editor, I have indicated in detail which part of the publication was actually written alone and have fully referenced such publications.
- vi. This dissertation/thesis does not contain text, graphics or tables copied and pasted from the Internet unless specifically acknowledged, and the source is detailed in the dissertation/thesis and the References sections.

Signed: Date: 09/01/2023
Mr Vulinhlanhla Salvation Mchunu

As the candidate's supervisor, I agree to the submission of this thesis.

Signed: Date: 09/01/2023
Dr Jean-Francois Pitot de la Beaujardiere

As the candidate's co-supervisor, I agree to the submission of this thesis.

Signed: Date: 09/01/2023
Prof Michael J. Brooks

Acknowledgements

To the Almighty God for giving me the strength and ability to pursue this master's degree and make it this far.

To my supervisors, Dr Jean Pitot and Prof Michael Brooks, and to Prof Glen Snedden, for continuous support and guidance throughout my journey in pursuit of this master's degree. I cannot forget to mention that I had weekly progress meetings with all my supervisors for the whole two years. That is the highest level of determination and consistency.

To the STEVE and ASReG teams, thank you for all the support and for providing extra hands when needed.

To the Discipline of Mechanical Engineering workshop team, much thanks for the technical advice you offered me regarding the propellant tanks' design and manufacturing considerations.

To the South African National Space Agency (SANSA), great thanks for supporting me financially for the duration of my master's studies.

To Fabricon Holdings for helping with the material testing phase of this research, and to ND Engineering for sponsoring the manufacturing and pressure testing for the test propellant tank.

To the Department of Science and Innovation, for funding ASReG's research as it seeks to enable South African space access.

Lastly, I would like to express my sincere gratitude to my family for all their support and prayers throughout my studies. To my mom, Busile, thank you for being how Rebecca was to Isaac.

Abstract

Having developed several hybrid sounding rockets, the Aerospace Systems Research Group (ASReG) at the University of KwaZulu-Natal is currently investigating the development of an indigenous launch vehicle for micro satellites. As part of this effort, a liquid propellant rocket engine called the South African First Integrated Rocket Engine (SAFFIRE) is in the advanced design phase. SAFFIRE combusts liquid oxygen and kerosene propellants to generate thrust. Following ground tests, the first version of the SAFFIRE engine will be incorporated into a single-stage launch vehicle to test its flight performance during the suborbital flight.

This study aimed to develop a design procedure and subsequent engineering designs for propellant tanks suitable for use by this launch vehicle, known as the Suborbital Test Vehicle (STEVE). The liquid oxygen and kerosene propellant tanks were designed according to NASA propellant tank design guidelines based on the mechanical properties of half-hard 301L stainless steel – the alloy selected as the material of construction for both tanks. This material has various advantageous characteristics, including its compatibility with liquid oxygen, its high strength once work-hardened and its increased strength and ductility at cryogenic temperatures.

As part of the study, comprehensive material testing was conducted to establish a suitable tank welding procedure and to evaluate the achievable weld efficiency. For the best-performing welding procedure assessed, mean weld efficiencies with respect to yield strength and tensile strength were determined to be 70 % and 81 %, respectively. A trial propellant tank was fabricated using the selected welding procedure and subsequently subjected to a destructive hydrostatic pressure test. The outcomes of this test provided a clear indication of the modes and progression of tank failure and served to inform final design work.

In terms of propellant tank layout, a tandem configuration with the liquid oxygen tank positioned above the kerosene tank was selected, in order to improve the stability characteristics of the vehicle and to minimise total feedline length. To reduce vehicle drag and mitigate aerodynamic heating effects, the liquid oxygen feedline was configured to pass coaxially through the kerosene tank via a tunnel tube. The incorporation of elliptical tank ends in both tank designs was dictated by pre-existing tooling made available by the tank end manufacturer. Based on these design characteristics, the anticipated tank loading conditions and the mechanical properties of the as-welded 301L stainless steel alloy, a minimum wall thickness requirement of 2 mm was determined for both tanks via finite element analysis.

List of Contents

1. Introduction	1
1.1. The Aerospace Systems Research Group	1
1.1.1. The Phoenix Programme	1
1.1.2. The SAFFIRE Programme	2
1.1.3. Suborbital Test Vehicle, STEVE	4
1.2. Research Aims and Objectives	5
1.3. Dissertation Outline	5
2. Literature Review	7
2.1. Introduction	7
2.2. Propellants	7
2.3. Suborbital Launch Vehicle	8
2.4. Orbital Launch Vehicles	10
2.4.1. The Atlas Launch Vehicle Family	10
2.4.2. Saturn V	11
2.4.3. SpaceX Starship	13
2.5. Propellant Tank Configurations	15
2.5.1. Tank Geometry	15
2.5.2. Tank Pressurisation Systems	17
2.5.3. Anti-Slosh Baffles	20
2.6. NASA Propellant Tank Design Guidelines	22
2.6.1. Internal Loading of The Tank	23
2.6.2. Propellant Tank Flight Loading	24
2.7. Propellant Tank Material	28
2.7.1. General characteristics of 300 Series Stainless Steel	28
2.7.2. 301 Stainless Steel Properties	29
2.7.3. Work Hardenability	30
2.7.4. Metal Spinning	32
2.7.5. Welding Operations	35
2.8. Summary	41
3. Propellant Tank Design Methodology	43

3.1.	Propellant Tank Design Process.....	43
4.	Preliminary Propellant Tank Design.....	47
4.1.	Introduction.....	47
4.2.	Propellant Tank Configuration and Design Specifications.....	47
4.3.	301L SS Mechanical Properties.....	49
4.4.	Propellant Tank Analytical Design.....	50
4.5.	Summary.....	52
5.	Material Testing.....	53
5.1.	Introduction.....	53
5.2.	Welding of 301 SS.....	53
5.2.1.	Welding by Fabricon.....	54
5.2.2.	Welding by ND Engineering.....	55
5.3.	Tensile Testing Procedure.....	56
5.4.	Tensile Test Results.....	58
5.4.1.	High Heat Input Welding Parameters.....	59
5.4.2.	Low Heat Input Welding Parameters.....	61
5.5.	Summary.....	63
6.	Final Propellant Tank Designs.....	64
6.1.	Introduction.....	64
6.2.	Propellant Tank CAD.....	64
6.3.	Propellant Tank Flight Loading.....	66
6.3.1.	Vehicle Inertial and Aerodynamic Loads.....	67
6.3.2.	Vehicle Bending Load.....	69
6.4.	Finite Element Analysis Setup.....	75
6.5.	Finite Element Analysis Results.....	79
6.5.1.	LOX Tank FEA Results.....	79
6.5.2.	Kerosene Tank FEA.....	81
6.6.	Tank Buckling.....	84
6.7.	Summary.....	85
7.	Propellant Test Tank Manufacture.....	87
7.1.	Introduction.....	87
7.2.	Tank End Spinning.....	87

7.2.1.	Tank End 3D Scan.....	89
7.3.	Tank Cylindrical Section Rolling.....	92
7.4.	Tank Strut Laser Cutting and CNC Bending.....	93
7.5.	Tank Welding.....	93
7.6.	Summary	96
8.	Propellant Tank Testing	97
8.1.	Introduction.....	97
8.2.	Pressure Test Procedure	97
8.3.	Pressure Test Results.....	99
8.4.	Summary	106
9.	Conclusion.....	107
9.1.	Satisfaction of Aims and Objectives	107
9.2.	Recommendations.....	109
9.3.	Future Work.....	110
	References	112
A.	Appendix I.....	120
B.	Appendix II.....	123
C.	Appendix III	126

List of Tables

Table 1-1: Phoenix – 1B Mk I and Mk IIr specifications and performance results	2
Table 1-2: CLV total vehicle specifications	3
Table 1-3: STEVE current design parameters	4
Table 2-1: Saturn V design specifications	12
Table 2-2: Anti-Slosh baffles design parameters	21
Table 2-3: Chemical composition for 300 series stainless steels	29
Table 2-4: 301 SS mechanical properties.....	31
Table 4-1: SAFFIRE engine parameters	48
Table 4-2: Propellant tank design specifications.....	49
Table 4-3: 301L SS mechanical properties.....	50
Table 4-4: Tank design input variables.....	50
Table 4-5: Tank theoretical thickness.....	51
Table 5-1: TIG welding parameters	53
Table 5-2: Tensile test results for unwelded 301L specimens	59
Table 5-3: Tensile test results for welded 301L specimens – high heat input	60
Table 5-4: Tensile test results for welded 301L specimens – low heat input.....	61
Table 6-1: Theoretical tank wall thickness based on assumed weld efficiency	64
Table 6-2: Description of the vehicle’s numbered sections.....	70
Table 6-3: LOX tank mesh independence study.....	76
Table 6-4: Simulation loads for the propellant tanks.....	78
Table 7-1: Tank Diameter 3D Scan Results	90
Table 8-1: Hydrostatic testing pressures	98
Table 8-2: Pressure test results	100
Table B-1: LOX tank design input <i>parameters</i>	123
Table B-2: CP Data for STEVE	125

List of Figures

Figure 1-1: The Phoenix – 1B Mk I (a) and Mk IIr (b) hybrid sounding rockets	1
Figure 1-2: Rendered SAFFIRE engine	3
Figure 1-3: Suborbital Test Vehicle configuration	4
Figure 2-1: Specific vacuum impulse versus propellant mixing ratio	7
Figure 2-2: Annotated artist's impression of the Spica I rocket	9
Figure 2-3: Spica rocket ethanol tank	9
Figure 2-4: Atlas IIAS booster stage and Atlas I	10
Figure 2-5: Atlas test vehicle tank's skin joints	11
Figure 2-6: Saturn V and stage S-IC components	12
Figure 2-7: The Starship spacecraft and super-heavy rocket integration	13
Figure 2-8: Starship spacecraft propellant tank configuration	14
Figure 2-9: Typical tank configurations for large turbopump-fed liquid propellant rocket engines	15
Figure 2-10: Various tank end shapes are spherical and elliptical	16
Figure 2-11: A typical tank with a common bulkhead	16
Figure 2-12: Regulated pressurisation system	18
Figure 2-13: Blowdown pressurisation system	19
Figure 2-14: Anti-slosh ring baffles in the Ares I US liquid hydrogen tank model	21
Figure 2-15: Pressure vessel nomenclature	22
Figure 2-16: Schematic of aerodynamic lift forces	25
Figure 2-17: The Schaeffler Diagram for typical stainless steel	28
Figure 2-18: Cold worked 301 SS mechanical properties	31
Figure 2-19: Cold worked 301 SS mechanical properties versus temperature	32
Figure 2-20: Setup of the spinning process	33
Figure 2-21: Springback phenomenon	34
Figure 2-22: Rolling process	34
Figure 2-23: A representation of a laser welding setup	35
Figure 2-24: Types of welds offered by laser	36
Figure 2-25: Most common laser joint types	36
Figure 2-26: Tungsten Inert Gas (TIG) welding setup	37
Figure 2-27: Skip welding	38
Figure 2-28: Effect of carbon control on carbide precipitation in 304 SS	39
Figure 3-1: STEVE propulsion system components	44
Figure 3-2: Development of the metallic liquid propellant tank design procedure	45
Figure 4-1: Elliptical tank end mandrel	47

Figure 4-2: STEVE booster section details.....	48
Figure 4-3: Kerosene tank.....	51
Figure 5-1: First weld trial by Fabricon	54
Figure 5-2: Skip welding technique implemented	55
Figure 5-3: Welding by ND Engineering	56
Figure 5-4: Sheet type test sample.....	56
Figure 5-5: Instron tensile testing machine.....	57
Figure 5-6: Tensile test samples	58
Figure 5-7: Welded tensile test sample	58
Figure 5-8: Unwelded specimen tensile test results	59
Figure 5-9: Welded specimen tensile test results – high heat input.....	60
Figure 5-10: Failure of the specimens	61
Figure 5-11: Welded specimen tensile test results – low heat input.....	62
Figure 6-1: Propellant tank integration	65
Figure 6-2: STEVE propellant tanks	65
Figure 6-3: Kerosene tank cross-section.....	66
Figure 6-4: Loads experienced by the LOX tank	67
Figure 6-5: STEVE flight acceleration profile.....	68
Figure 6-6: STEVE flight velocity profile	68
Figure 6-7: Inertial load on the kerosene tank	69
Figure 6-8: STEVE lift forces diagram	70
Figure 6-9: Air density vs time profile	71
Figure 6-10: Dynamic pressure vs time profile	71
Figure 6-11: STEVE angle of attack profile	72
Figure 6-12: Nose cone and rocket’s body normal force	73
Figure 6-13: STEVE angle of attack profile at induced jet stream.....	73
Figure 6-14: Fins normal force and the centre of pressure	74
Figure 6-15: STEVE shear force diagram at 2 ° angle of attack	75
Figure 6-16: Simulation stages of ANSYS static structural analysis	76
Figure 6-17: LOX tank mesh independence study.....	77
Figure 6-18: LOX tank mesh	77
Figure 6-19: LOX tank simulation setup	78
Figure 6-20: LOX tank equivalent stress due to the internal pressure loading (a) and combined loading (b).....	79
Figure 6-21: LOX tank hoop stress due to the internal pressure loading (a) and combined loading (b).....	80

Figure 6-22: LOX tank total deformation due to the internal pressure loading (a) and combined loading (b).....	80
Figure 6-23: LOX tank safety factor against the internal pressure loading (a) and combined loading (b).....	81
Figure 6-24: Kerosene tank equivalent stress due to the internal pressure loading (a) and combined loading (b).....	82
Figure 6-25: Kerosene tank hoop stress due to the internal pressure loading (a) and combined loading (b).....	82
Figure 6-26: Kerosene tank total deformation due to the internal pressure loading (a) and combined loading (b).....	83
Figure 6-27: Kerosene tank safety factor against internal pressure loading (a) and combined loading (b).....	83
Figure 6-28: Total deformation due to buckling for the LOX (a) and kerosene (b) tanks	84
Figure 7-1: Spinning process typical setup at Metspin.....	88
Figure 7-2: 301L SS test tank elliptical end	88
Figure 7-3: PC-DMIS 3D scan setup	89
Figure 7-4: Tank end geometry generated by PC-DMIS.....	90
Figure 7-5: 3D scan results for tank 1	90
Figure 7-6: 3D scan results for tank end 2 and 3.....	91
Figure 7-7: 3D scan results for tank end 2.....	91
Figure 7-8: Trial 500 mm cylindrical section	92
Figure 7-9: Tank skirt/support	93
Figure 7-10: Welding tank's cylindrical section showing post-weld geometry (LHS) and tack welds (RHS).....	94
Figure 7-11: Test propellant tank showing final construction (LHS) and top tank end (RHS).....	94
Figure 8-1: Pressure test setup showing the tank prior to the test (LHS) and during the testing procedure (RHS).....	99
Figure 8-2: Tank end 1 and tank end 3 post-test.....	101
Figure 8-3: Tank end 2 geometry after pressure testing	102
Figure 8-4: Tank skirt flange welded to the test stand	103
Figure 8-5: Test tank fails on the seam weld	104
Figure 8-6: Test tank weld failure and heat-affected zone (HAZ).....	104
Figure A-1: Ellipse ratio, k versus knuckle stress factor k , compression stress $-K$ and parameter E'	120
Figure A-2: 301L SS material certificate.....	121
Figure A-3: Radiographic test of the longitudinal weld.....	122
Figure B-1: Rocket's COM (CG) and COP (CP) position during flight.....	125

List of Symbols

Symbol	Description	Units
e	Eccentricity	-
e_w	Weld efficiency	-
ν	Poisson's ratio	-
E'	Ellipse ratio	-
C_b	Buckling coefficient	-
C_d	Coefficient of drag	-
k	Ratio of tank radius to tank end minor radius	-
K	knuckle stress factor	-
a	Acceleration of the vehicle	m/s ²
A	Cross-sectional area	m ²
A_c	Surface area of the cylindrical tank section	m ²
A_e	Surface area of the ellipsoidal tank end	m ²
A_s	Surface area of the spherical tank end	m ²
A_x	Axial load	N
b	Elliptical tank end minor radius	m
D	Aerodynamic drag force	N
E	Young's modulus of elasticity	Pa
F_a	Critical axial compressive load	N
l_c	Length of the cylindrical tank section	m
m_c	Mass of the cylindrical tank section	kg
m_e	Mass of the ellipsoidal tank end	kg
m_s	Mass of the spherical tank end	kg
M	Bending moment	N.m
P	Maximum working pressure of the tank	Pa
P_{cr}	Critical pressure as a result of external loading	Pa
ρ	Density of the material	kg/m ³
r	Cylindrical tank section radius	m
R_i	Inner radius	m
R_o	Outer radius	m
S_c	Critical axial compressive stress	Pa
S_u	Tensile strength	Pa
S_w	Maximum allowable working stress	Pa
S_y	Yield strength	Pa
T	Vehicle's thrust	N
t_c	Cylindrical tank section wall thickness	m
t_{cr}	Crown wall thickness	m

Symbol	Description	Units
t_e	Ellipsoidal tank end equivalent wall thickness	m
t_k	Knuckle wall thickness	m
t_s	Spherical tank end equivalent wall thickness	m
V	Shear force	N
V_c	Cylindrical tank section volume	m ³
V_e	Ellipsoidal tank end volume	m ³
V_s	Spherical tank end volume	m ³
V_x	Velocity of the vehicle	m/s
w_y	Uniform distributed load	N/m
σ_e	Equivalent stress	Pa
σ_1	Hoop stress	Pa
σ_2	Circumferential stress	Pa

List of Abbreviations

Abbreviation	Description
ASReG	Aerospace Systems Research Group
ASTM	American Society for Testing and Materials
C	Carbon
CAD	Computer Aided Design
CLV	Commercial Launch Vehicle
CMMS	Coordinate Measuring Machines
DC	Direct Current
FEA	Finite Element Analysis
FTS	Flight Termination System
GMA	Gas Metal Arc
GOX	Gaseous Oxygen
GSE	Ground Support Equipment
GTAW	Gas Tungsten Arc Welding
HAZ	Heat Affected Zone
HYROPS	Hybrid Rocket Performance Simulator
LEO	Low Earth Orbit
LH ₂	Liquid Hydrogen
LHS	Left Hand Side
LOF	Lack of Fusion
LOX	Liquid Oxygen
MAG	Metal Active Gas
MIG	Metal Inert Gas
Mk	Mark
Nd: YAG	Neodymium-Doped Yttrium Aluminium Garnet
OF	Oxidiser to Fuel
RHS	Right Hand Side
RP-1	Rocket Propellant 1 (Refined Propellant 1)
SA	Submerged Arc
SAFFIRE	South African First Integrated Rocket Engine
SN	Serial Number
SS	Stainless Steel
TIG	Tungsten Inert Gas
UDL	Uniform Distributed Load

1. Introduction

1.1. The Aerospace Systems Research Group

The Aerospace Systems Research Group (ASReG) at the University of KwaZulu-Natal (UKZN) embarked on a mission to develop hybrid sounding rockets in pursuit of addressing South Africa's launch needs and Africa at large since the year 2009. This research group also aims to inspire students to pursue postgraduate studies and to generate interest in rocket propulsion, flight dynamics and airframe design in South Africa.

1.1.1. The Phoenix Programme

The Phoenix programme entailed the development of hybrid sounding rockets. The rockets that have been designed, manufactured, and flight-tested successfully include the Phoenix – 1A, Phoenix – 1B Mk I and Phoenix – 1B Mk IIr. The Phoenix – 1A hybrid rocket was the first vehicle to be developed and flight-tested. The rocket experienced nozzle failure during the flight test reaching 2.5 km (Chowdhury, 2012). The Phoenix – 1B Mk I and Mk IIr hybrid sounding rockets were flight tested at the beginning of 2021, reaching an altitude of 11.3 km and 17.9 km, respectively (Balmogim, 2017) (Broughton, 2018). Both vehicles broke the African record of 10.7 km are shown in Figure 1-1.



Figure 1-1: The Phoenix – 1B Mk I (a) and Mk IIr (b) hybrid sounding rockets

These hybrid sounding rockets utilise nitrous oxide and paraffin wax for propulsion. This programme has been instrumental in the human capital development of rocket scientists specialising in rocket propulsion design. The oxidiser tanks for Phoenix – 1B Mk I and Phoenix – 1B Mk IIr vehicles were constructed of aluminium and composite materials, respectively (Balmogim, 2017) (Williams , 2019).

The key specifications and performance results for the Phoenix – 1B Mk I and Mk IIr hybrid sounding rockets are presented in Table 1-1.

Table 1-1: Phoenix – 1B Mk I and Mk IIr specifications and performance results (Broughton, 2018) (Balmogim, 2017)

Parameter	Units	Mk I	Mk IIr
Diameter	mm	164	170
Overall length	mm	4675	4920
Total mass	kg	88	90
Motor burn out	s	17	20
Apogee	mm	11 154	17 938
Max. speed	m/s	426	702
Max. acceleration	m/s ²	35.4	65.9

1.1.2. The SAFFIRE Programme

In developing an indigenous launch vehicle, the design of a liquid propellant rocket engine called the South African First Integrated Rocket Engine (SAFFIRE) is at an advanced stage. The engine employs liquid oxygen (LOX) and kerosene (RP-1) propellants to generate a thrust of 25 kN at sea level (Wunderlin, et al., 2021). To place a payload of 75 kg into LEO, the launcher’s booster stage must consist of nine clustered SAFFIRE engines. The SAFFIRE engine shown in Figure 1-2 will utilise a combination of film and ablative cooling, resulting in cost reduction and reduced design complexity.



Figure 1-2: Rendered SAFFIRE engine (Wunderlin, et al., 2021)

The commercial launch vehicle (CLV) design specifications that will utilise numerous SAFFIRE engines are presented in Table 1-2.

Table 1-2: CLV total vehicle specifications (Wunderlin, et al., 2021)

Parameter	Unit	Value
Diameter	m	1.5
Height	m	15.9
Dry mass	kg	1 565
Propellant mass	kg	11 165
Propellant mass fraction	-	0.877
Stages	-	2

The need for Low Earth Orbital-based services has increased substantially. Over the last 17 years (2000-2017), Africa has witnessed a growth of 9942% in demand for high-speed broadband and telecommunications (Miniwatts Marketing Group, 2020). As the global population penetration for internet usage is 58.4% compared to 35.2% for the African continent, further growth in telecommunications can be expected. The primary reasons countries invest in commercial launch vehicles include financial profit, impact on national development and strategic advantage. An indigenous launch vehicle should be established in accordance with the capability and competencies of the South African aerospace sector to make the program realistic and realisable from an engineering perspective (Wunderlin, et al., 2021).

1.1.3. Suborbital Test Vehicle, STEVE

Following ground tests, the first version of the SAFFIRE engine will be incorporated into a single-stage rocket or launch vehicle to evaluate its flight performance during a suborbital flight. The proposed vehicle for conducting a flight test of the SAFFIRE engine is called the Suborbital Test Vehicle (STEVE), shown in Figure 1-3. This test vehicle is designed to be a scaled-down model of the proposed commercial launch vehicle (CLV) by four. The vehicle consists of separate oxidiser and fuel tanks, pressurant tanks, a roll control system, and a payload bay. The propellant tanks are pressurised by helium gas, and the roll control system utilises nitrogen gas to stabilise the vehicle.

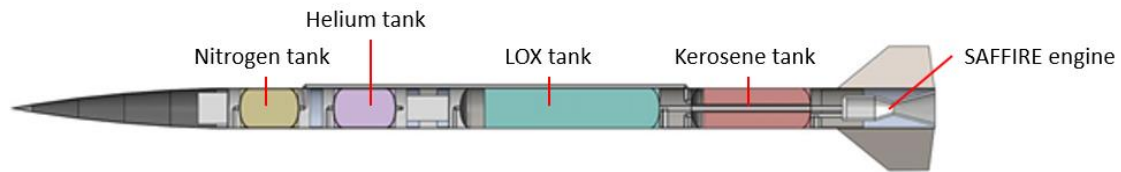


Figure 1-3: Suborbital Test Vehicle configuration

The vehicle's current design parameters are listed in Table 1-3.

Table 1-3: STEVE current design parameters

Parameter	Unit	Value
Total mass	kg	679
Propellant mass rate	kg/s	10
OF ratio	-	2.39
Burn time	s	40
Diameter	mm	386
Length	m	9
Maximum altitude	m	100 000
Mach number	-	5
Maximum acceleration	m/s ²	77

1.2. Research Aims and Objectives

This research project aims to design, manufacture, and test propellant tanks for a Suborbital Test Vehicle (STEVE). The development of the propellant tanks will assist in constructing a launch vehicle (STEVE) to function as a suborbital platform for testing the flight performance of SAFFIRE engines.

The tanks' design requires determining end geometries and dimensions, selecting a suitable construction material, and specifying appropriate loading conditions. Propellant tanks constitute a significant percentage of a launch vehicle's structural mass, and their mass must be minimised to maximise vehicle performance (Huzel & Huang, 1967). Austenitic stainless steel 301 has been selected for the construction of STEVE's propellant tanks.

Propellant tanks are subjected to loading from sources including internal pressure, inertial forces, bending moments induced by vehicle side accelerations, and aerodynamic forces (Huzel & Huang, 1992). Finite element analyses (FEA) play a vital role in the design of rocket components and enable the determination of the structural efficiency of propellant tanks based on loading and boundary conditions (Basu, et al., 1996).

The development of liquid propellant tanks for a suborbital launch vehicle will be achieved by satisfying the following objectives:

1. Develop the design procedure for metallic liquid propellant tanks
2. Propose a suitable design for propellant tanks
3. Manufacture a test propellant tank
4. Conduct pressure tests on the test tank to verify the design procedure of metallic liquid propellant tanks for a suborbital launch vehicle

1.3 Dissertation Outline

Chapter 2 consists of an in-depth literature review on existing suborbital launch vehicles and launch vehicles, different propellant tank configurations and design considerations, NASA propellant tank design guidelines, austenitic stainless steel selection for the tank construction and its properties. Forming operations for tank manufacture are also included.

Chapter 3 details the design methodology for the STEVE propellant tanks. This chapter gives a step-by-step procedure for developing the STEVE tanks.

Chapter 4 focuses on the preliminary design of the propellant tanks. The initial wall thickness and geometry of the tanks are determined. The propellant tank is only subjected to internal pressure.

Chapter 5 describes the material testing procedure and results to experimentally determine the weld efficiency of 301 stainless steel. This will pave the way to settling on the final design input parameters. The tensile testing results are also included in this section. The tank welding procedure is developed in this section.

Chapter 6 presents the final propellant tank design. This chapter evaluates the propellant tank wall thickness against the flight loads. This was executed by performing a finite element analysis using the ANSYS Workbench software program.

Chapter 7 details the manufacturing process of the test tank. The tank ends, and the tank's cylindrical section are manufactured through the spinning and rolling techniques, respectively. The chapter also includes the 3D scan results of the tank ends varying thickness due to the thickness reduction occurring during the spinning process.

Chapter 8 describes the pressure testing procedure of the propellant tanks, utilising water as the testing medium. This test aims to determine the weakest point in the tank, whether it is the longitudinal weld or the tank ends, and also the yielding point of the tank. The tank is pressurised to destruction.

Chapter 9 consists of the conclusion, recommendations, and future work. The conclusion indicates whether the research objectives were achieved or not and to what extent. Recommendations are given for the various stages of the tank development. This project's further steps and development are incorporated in the future work subsection.

2. Literature Review

2.1. Introduction

This section reviews the literature related to the design and manufacture of liquid propellant tanks for launch vehicles to make informed design decisions.

2.2. Propellants

The proposed propellants for STEVE are liquid oxygen (LOX) and kerosene. LOX is widely used as an oxidiser with kerosene, liquid hydrogen, gasoline, and alcohols (Sutton & Biblarz, 2001). Due to its high performance, it is desirable for large rocket engines. LOX's nontoxic and noncorrosive nature makes it desirable as it does not cause deterioration of the tank's inner surfaces (Braeuning, 2008) (Sutton & Biblarz, 2010).

The selection of propellants is based on the performance parameters such as the specific impulse, the characteristic velocity, and the exhaust velocity. The typical physical hazards considered when selecting propellants include corrosion, explosion, ignition, health, and material compatibility. The density of the propellant is directly proportional to the tank's volume, and a denser propellant will require a smaller tank volume (Sutton & Biblarz, 2010).

Figure 2-1 shows the relationship between the specific impulse and propellant mixture ratio for various bipropellants (Martinez, 2020). Kerosene provides a lower specific impulse than cryogenic hydrogen, but it is usually better than hypergolic propellants (Sutton & Biblarz, 2010). The combination of LOX with kerosene (RP-1) was employed in the Atlas, Delta II and Soyuz (Russia) launch vehicles (Braeuning, 2008) (Sutton & Biblarz, 2010).

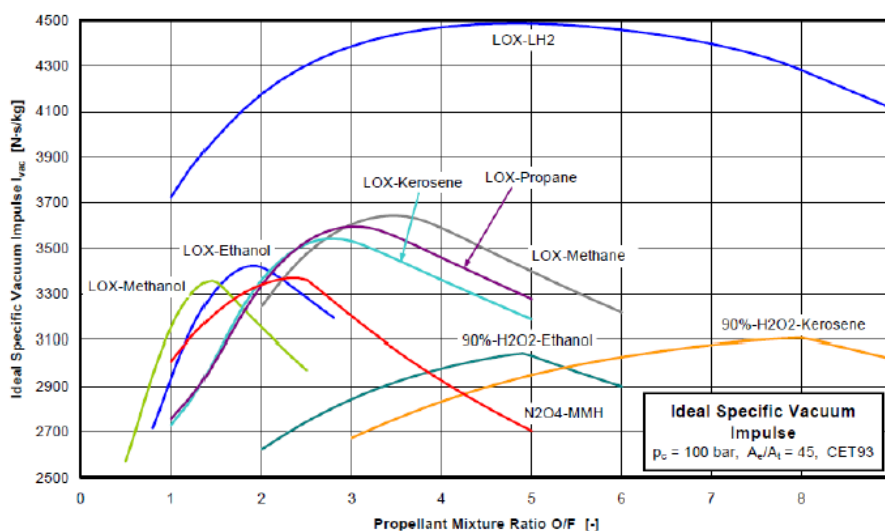


Figure 2-1: Specific vacuum impulse versus propellant mixing ratio (Martinez, 2020)

2.3. Suborbital Launch Vehicle

Since STEVE is intended to be a suborbital launch vehicle, an intensive study was conducted to review the characteristics of current and recent suborbital launch vehicles. The review criteria were vehicles with propellant tanks constructed from stainless steel and/or vehicles combusting liquid oxygen and kerosene to generate thrust. Due to material science advancement, it was found that most of the recent liquid propellant tanks for suborbital launch vehicles are made from composite materials. The Spica suborbital rocket developed by Copenhagen Suborbitals was considered for review as it is the latest sounding rocket made from stainless steel.

Spica Rocket

The Spica rocket was designed and constructed by Copenhagen Suborbitals, a Danish crowd-funded organisation. This rocket is meant to house an astronaut in the Apollo-inspired capsule Tycho Deep Space II (TDSII) (Wood, 2015). The Spica rocket has an outer diameter and an overall length of 955 mm and 13 m, respectively. A bi-propellant engine produces a thrust of 100 kN burning ethanol and liquid oxygen. A pressure-fed, blow-down method is employed to feed propellants into the engine with an active pressurisation system.

This rocket is currently under construction and is expected to achieve a 105 km altitude within 3.10 minutes. Motor burn-out occurs at 90 seconds of the vehicle's flight, with the vehicle reaching a maximum velocity of 1 000 m/s (Mach 2.9).

As illustrated in Figure 2-2, the fuel feedline runs outside the vehicle (Wood, 2015). The propellant tanks are manufactured from a 304 stainless steel sheet of 3mm thickness. The tanks are strain hardened after manufacture by pressurising them above their design pressure, consequently improving the strength of the material. The tank operating pressure ranges between 20 and 21 bar (Pedersen, 2019).



Figure 2-2: Annotated artist's impression of the Spica I rocket (Wood, 2015)

The strain-hardened Spica rocket ethanol tank with slight deformation is shown in Figure 2-3 (Pedersen, 2019). The anti-slosh baffles are made in segments to allow the tank's diameter to stretch during the strain hardening process (Pedersen, 2019). The tank's seam is welded using a semi-automated TIG welding process.

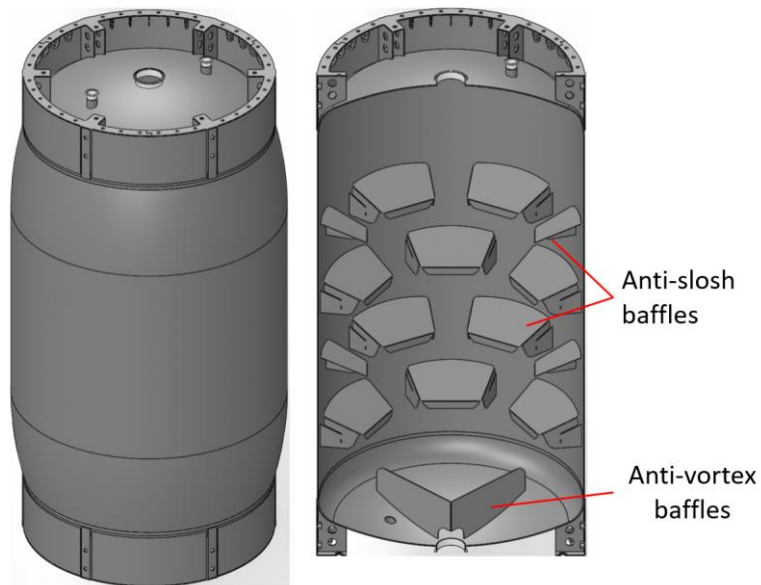


Figure 2-3: Spica rocket ethanol tank (Pedersen, 2019)

2.4. Orbital Launch Vehicles

Since the design of STEVE is part of the process of developing an indigenous launch vehicle for Africa as a whole, it is of value to review launch vehicles powered by LOX and kerosene, with propellant tanks made from stainless steel. These include the Atlas I & II, Saturn V and the Starship launch vehicles, which will now be reviewed. The launch vehicle's design specifications, performance and unique attributes will also be highlighted.

2.4.1. The Atlas Launch Vehicle Family

The Atlas B launch vehicle was first launched in the late 1950s, and Mercury-Atlas 7 vehicle made history in the 1960s for sending four United States astronauts to orbit the Earth on America's first manned orbital missions. The Atlas I, II, and III space launchers employed lightweight pressure-stabilised balloon-type propellant tanks fabricated from stainless steel (Henson & Jone, 2018). To prevent balloon tanks from collapsing under their own weight during transport or on the launch pad, they require stabilisation via mechanical tension ("stretch") or internal pressure.

The propellant tank made from 301 stainless steel for the Atlas IIAS booster stage consisted of a common bulkhead (elliptical) separating the forward LOX tank and the aft RP-1 (kerosene) tank (Douglass, et al., 1974). Positive pressure was maintained on the fuel tank to prevent buckling failure. Shown in Figure 2-4 is the Atlas I on the launch pad; the forward LOX tank is frost-covered, while the aft fuel tank is frost-free, exposing the 301 stainless steel tank material (Niesley, 1981).

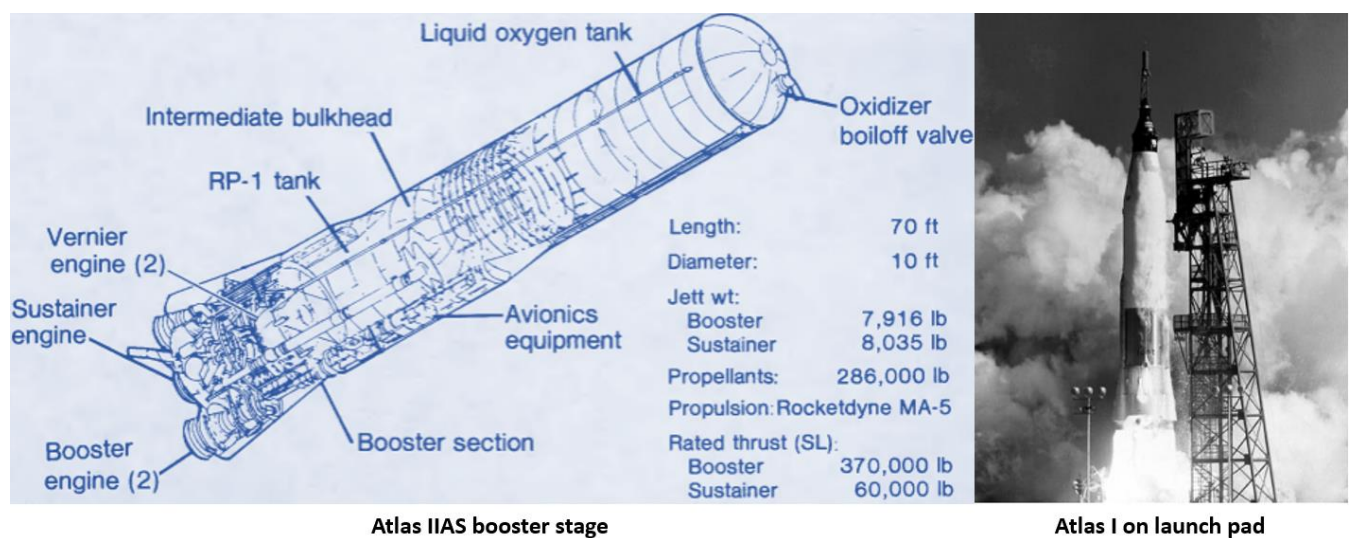


Figure 2-4: Atlas IIAS booster stage (Henson & Jone, 2018) and Atlas I (Niesley, 1981)

The pressure applied by the pressurisation system is enough for propellant feed and for keeping the tanks stable under flight loads (Douglass, et al., 1974) (Henson & Jone, 2018). The tank's cylindrical sections for the Atlas and Centaur vehicles are made from extra full-hard 301 stainless steel with thickness as thin as 0.25 mm (Niesley, 1981) (Henson & Jone, 2018). For better formability, the tank ends, or transitions for the Atlas I vehicle were manufactured from half and three-quarter hard 301 stainless steel. The tank's longitudinal seam was resistance butt welded with the doubler spot-welded at several rows. The longitudinal welds were reinforced with a plate/sheet referred to as the doubler, as shown in Figure 2-5 (Miller, 1969).

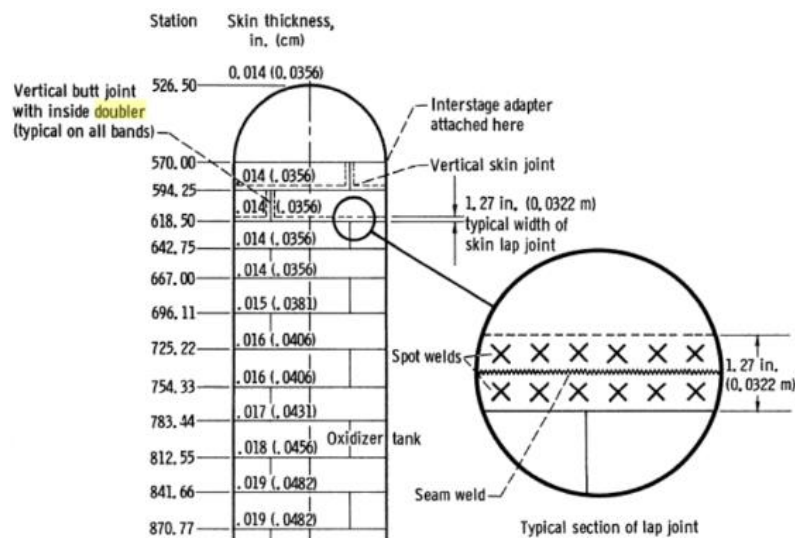


Figure 2-5: Atlas test vehicle tank's skin joints (Miller, 1969)

2.4.2. Saturn V

The Saturn V rocket was developed and launched several times from 1967. This vehicle was designed to support the NASA Apollo program for moon exploration by humans. The "V" refers to the five F-1 engines that propelled the first stage (Michael, 2009). The vehicle consisted of three stages, S-IC, S-II and S-IVB, as illustrated in Figure 2-6 (Smithsonian, 2018). The first stage, S-IC, was powered by LOX and RP-1, whereas the other two stages used LOX and LH₂. The stage S-IC is of interest in this project as it used the same propellants, and its feedlines configuration eliminated the need to run them externally of the vehicle. The air gap between the kerosene tank internal duct and LOX feedline was sufficient to prevent kerosene gelling or evaporation of LOX. These two risks can result in combustion instabilities, affecting the engine's performance. The summary of Saturn V specifications is presented in Table 2-1.

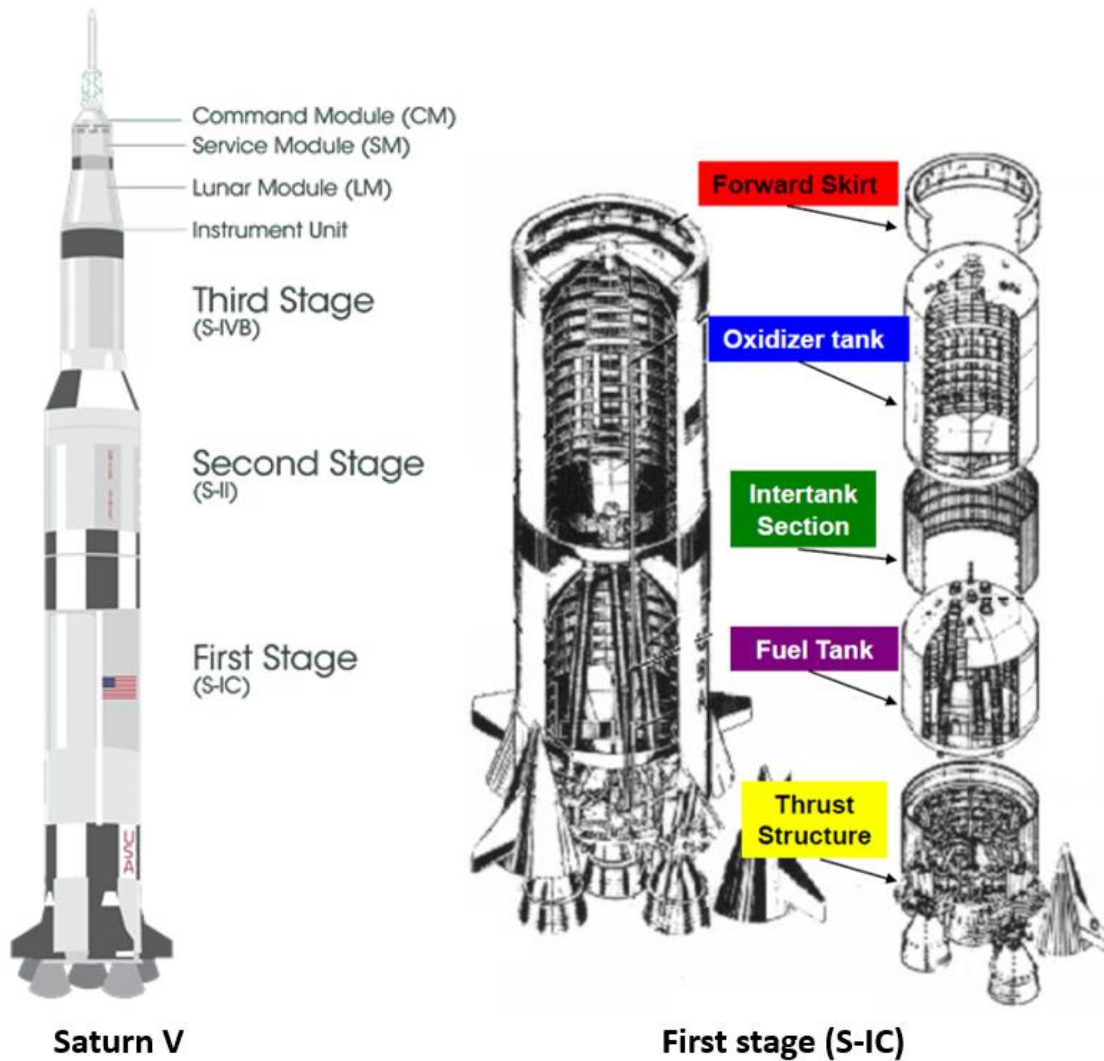


Figure 2-6: Saturn V (Smithsonian, 2018) and stage S-IC components (Marshall, 1969)

Table 2-1: Saturn V design specifications (Smithsonian, 2018) (SVFEW Group, 1967)

Parameter	Saturn V		
	Stage S-IC	Stage S-II	Stage S-IVB
Diameter (m)	10.1	10.1	6.6
Length (m)	42.0	24.9	17.9
Propellants	LO ₂ /RP-1	LO ₂ /LH ₂	LO ₂ /LH ₂
Pressurant	GHe/GOX	GO ₂ /GH ₂	GHe
OF Ratio	2.3	5.5	5.0
Burn time (s)	151 - 168	366 - 384	156 – 347 (consist of 2 burns)
Thrust (kN)	33 904	5083	1 000 – 1 800
Altitude (km)	59.5	185.0	Translunar trajectory (moon)

The first stage, S-IC propulsion, consists of the LOX fed through five feedlines passing through the tunnel of the RP-1 tank made from aluminium 2219 (Clark, 2015). The RP-1 tank was pressurised by gaseous helium and preheated by the F-1 engine heat exchangers. At the same time, the LOX tank was pressurised by gaseous oxygen (GOX), which was tapped off from the engine before entering the combustion chamber (Clark, 2015).

2.4.3. SpaceX Starship

SpaceX has developed a launch system, Starship, capable of transporting people and significant amounts of cargo to the Moon and Mars (Nicholson, 2019). SpaceX's Starship system incorporates the Super Heavy booster and Starship spacecraft (collectively referred to as Starship). It is a fully reusable launch system designed to cater for Earth orbit requirements and interplanetary missions (SpaceX, 2020).

The Starship system is shown in Figure 2-7 and has a height and diameter of 122 m and 9.1 m, respectively (Cotton, 2020) (SpaceX, 2020). Once operational, Starship will offer a greater payload capacity than any other launch system constructed to date (Berger & Mahlmann, 2019).

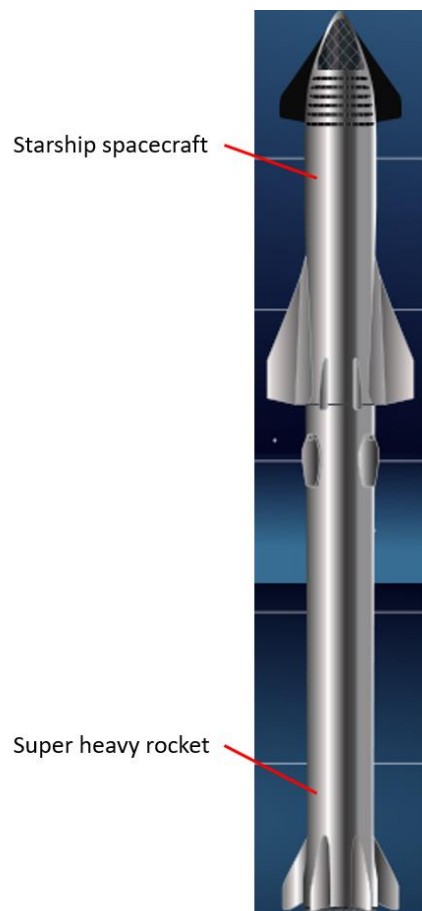


Figure 2-7: The Starship spacecraft and super-heavy rocket integration (SpaceX, 2020)

The Starship spacecraft, which will burn a cryogenic fuel (liquid methane) and a cryogenic oxidizer (LOX), has undergone several design iterations, ranging from versions SN1 to SN20. The propellant tanks for prototypes SN1 to SN6 were manufactured from 301 stainless steel (Cotton, 2020). The strength and ductility of 301 stainless steel increases at cryogenic temperatures (-273 °C to -150 °C). Interestingly, the fracture toughness of this alloy is higher at cryogenic than ambient temperatures (Nicholson, 2019).

The cost of materials also influenced SpaceX's decision to use 301 stainless steel to construct the Starship as it was found to cost \$2 500 less per ton than carbon fibre which was \$130 000 per ton (Nicholson, 2019). Although tanks fabricated from carbon fibre would provide mass savings due to their high strength-to-weight ratio, the manufacturing process is comparatively slow, and 35 % of the material used ends up as unusable scrap (Whitwam, 2019).

301 stainless steel has a higher melting point (about 1500 °C) than other steels. It is about five times that of carbon fibre or aluminium, meaning the vehicle will require less shielding from aerodynamic heating and radiation (Whitwam, 2019). The prototypes starting from SN8 were made from 304L stainless steel and were first integrated with the nosecone and aerodynamic control surfaces for flight testing (Cotton, 2020).

Starship employs a common bulkhead propellant tank with LOX above the liquid methane tank, as shown in Figure 2-8 and encapsulates small header propellant tanks used for the landing burn (SpaceX, 2020) (Scroochy, 2020). These header tanks are critical to prevent sloshing before the burn, failing which the engines could ingest air bubbles causing combustion instabilities (Scroochy, 2020). The positions of the propellant tanks have been interchanged during various prototype development to balance the mass of Raptor engines and control surfaces at the bottom.

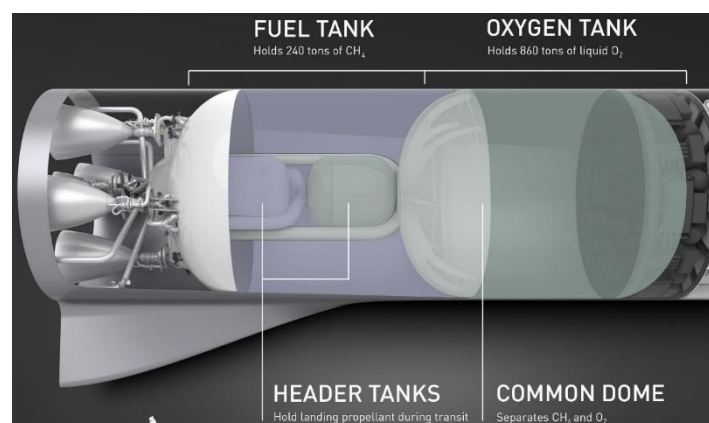


Figure 2-8: Starship spacecraft propellant tank configuration (SpaceX, 2020) (Scroochy, 2020)

2.5. Propellant Tank Configurations

2.5.1. Tank Geometry

The design, shape, and position of propellant tanks can affect how the vehicle's centre of gravity shifts in flight. Tanks can be configured as spherical, tandem and concentric, as illustrated in Figure 2-9 (Sutton & Biblarz, 2010). A propellant tank (including a gas pressurizing tank) should ideally be spherical because it produces the lowest tank mass for a given volume. However, large spherical tanks required for the main propulsion systems are not efficiently integrated with the vehicle fuselage. Cylindrical tanks with elliptical or spherical ends are used due to the massive amounts of propellant required for launch vehicle propulsion and integrate better with the vehicle's aerostucture (Sutton & Biblarz, 2010). Whether it runs within or externally of the tanks, the layout of the pipe from the top propellant tank is another factor to be considered when designing a propellant tank.

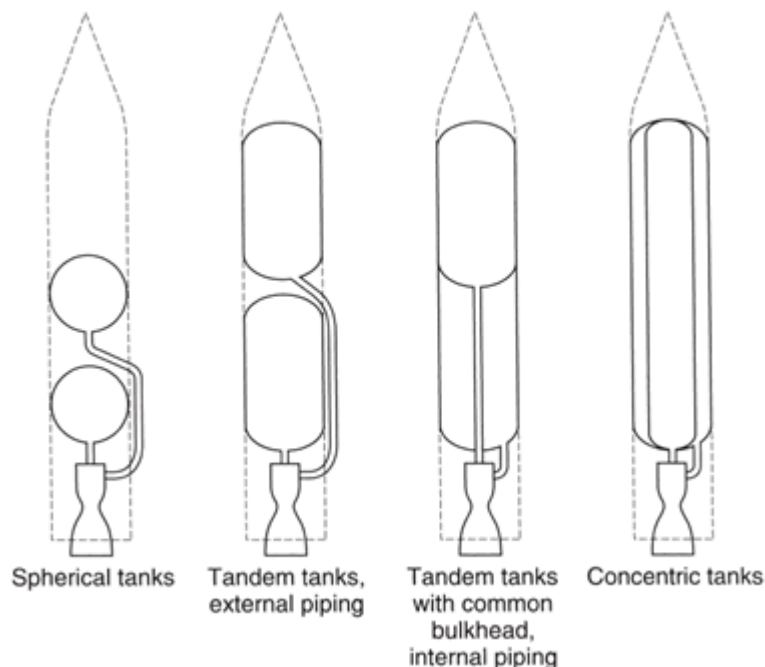


Figure 2-9: Typical tank configurations for large turbopump-fed liquid propellant rocket engines (Sutton & Biblarz, 2010)

The most common configuration for launch vehicles is tanks in tandem arrangement. In this configuration, an “intertank” structure separates the tanks and feedlines from the upper tank run externally or internally within the tank below (Sutton & Biblarz, 2001). Because LOX has a higher density than kerosene, it is often placed above the fuel in rockets combusting these propellants to improve the vehicle's stability margin (Borogove, 2021).

Large spherical tanks required for the main propulsion systems are not efficient to be integrated with the vehicle fuselage. In comparison, the tandem tanks result in a shorter rocket

which will experience less stress due to reduced cross-sectional area (i.e., less drag) (Honkawa, 2020). Furthermore, tank mass is higher in tanks where the tank end enclosures are "flatter"; that is, the ratio of radius to end height is higher, as illustrated in Figure 2-10 (Tam, et al., 2006).

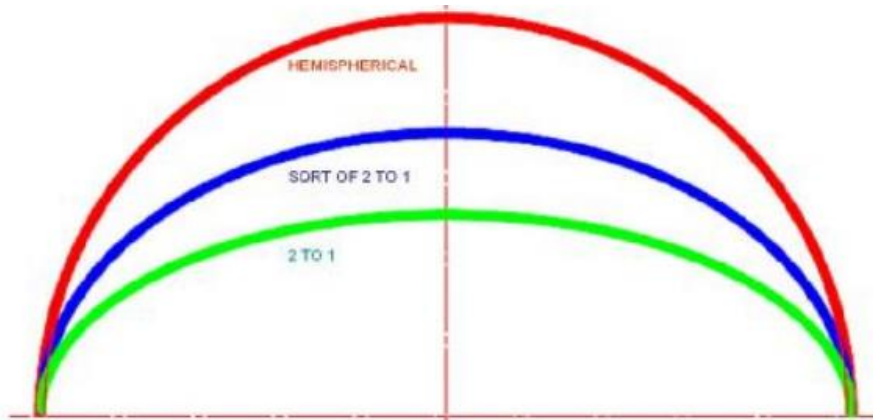


Figure 2-10: Various tank end shapes are spherical and elliptical (Tam, et al., 2006)

The common bulkhead tank configuration depicted in Figure 2-11 reduces the vehicle's height, while the separate propellant tanks configuration results in a heavier vehicle with a reduced payload mass capacity (Tam, et al., 2006). This is due to the need for an additional bulkhead and an inter-tank structure between the two tanks (Dumont, et al., 2011). The use of a common bulkhead also allows for a shorter stack. This allows more design flexibility in balancing aerodynamic and mass concerns (Slugg, 2020).

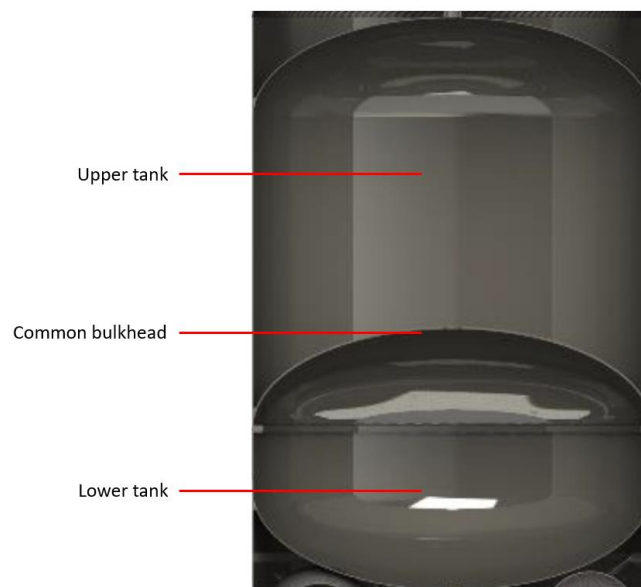


Figure 2-11: A typical tank with a common bulkhead (Gyasi-Agyei, 2021)

From the standpoint of interchangeability, a significant drawback of the shared bulkhead design is that if one of the two tanks develops an irreparable problem, both tanks must be discarded (Slugg, 2020). There is also a risk of explosion should the common bulkhead leak, fracture, or burst. When cryogenic propellants are stored in tanks with a common bulkhead, the temperature difference across the common bulkhead causes propellant evaporation, which affects engine performance (Dumont, et al., 2011). As a result, the common bulkhead requires highly effective insulation. The use of a common bulkhead in a reusable vehicle poses challenges to the vehicle's reliability and inspectability (Lepsch, et al., 1995). To reduce risk and operational complexity, the separate-tank configuration is currently preferred. The fundamental design difficulty of the common bulkhead propellant tank is to prevent buckling because both compartments are pressurised (Tam, et al., 2006).

Previous research on the optimal geometric configuration of the propellant tanks for launch vehicles conducted at UKZN considered cylindrical tanks with spherical ends (CS), cylindrical tanks having elliptical ends (CE), and combinations of CS(LOX)/CE (kerosene) and CS (kerosene)/CE(LOX) (Gyasi-Agyei, 2021). A cylindrical tank with spherical ends (CS) results in a tank with the lowest mass. In contrast, a cylindrical tank with elliptical ends (CE) results in a tank with the lowest height (Gyasi-Agyei, 2021). A spherical common bulkhead tank with spherical ends yielded the smallest tank mass. In contrast, a configuration featuring a spherical common bulkhead with elliptical ends resulted in the lowest tank heights. The common bulkhead configuration offers tank mass and height reductions of 23 % and 17 %, respectively (Gyasi-Agyei, 2021).

2.5.2. Tank Pressurisation Systems

The pressurisation system of a liquid rocket engine entails using pressurant gas to drive propellants into the engine. The pressurant can either be contained in a separate tank or in the propellant tank ullage space. Tank operating pressure in pressurisation system configurations has been observed to range between 13 and 90 bar, with pressurant vessel pressures ranging between 69 and 690 bar (Sutton & Biblarz, 2001).

Tank pressurisation systems can be implemented using a high-pressure inert gas, a heated high-pressure inert gas, gas is created by a chemical reaction, evaporation of a cryogenic liquid propellant, or self-pressurisation of cryogenic propellants (Hearn, 1982) (Huzel & Huang, 1992) (Hearn, 1995). The most common method is to employ a high-pressure inert gas, helium, nitrogen, or air.

Gaseous nitrogen condenses instantly at the interface of LOX, forming a liquid layer, according to research conducted in the 1960s (Greenfield, 1960) (Bowersock, et al., 1960). The liquid nitrogen diffuses into the LOX, contaminating it. Helium is preferable over nitrogen because of its lower molecular weight, which gives it a weight advantage in the system (Sutton & Biblarz, 2001). Helium also has a lower temperature of condensation than any other pressurant.

The pressurising gas is held separately from the propellants in the regulated system, which uses a pressure regulator to maintain a consistent tank pressure (Huzel & Huang, 1992) (Hearn, 1982). The regulator is typically driven by a pilot valve with a narrow control band and might have an internal or external sensing element (Tomlinson & Keller, 1973). To reduce the ullage-pressure differential in the tanks, most launch vehicles use a shared pressure regulator to pressurise both the oxidiser and fuel tanks, as shown in Figure 2-12 (Lee & Ramirez, 1975) (Hearn, 1995). This approach also keeps the engine thrust and propellant mixture ratio relatively consistent.

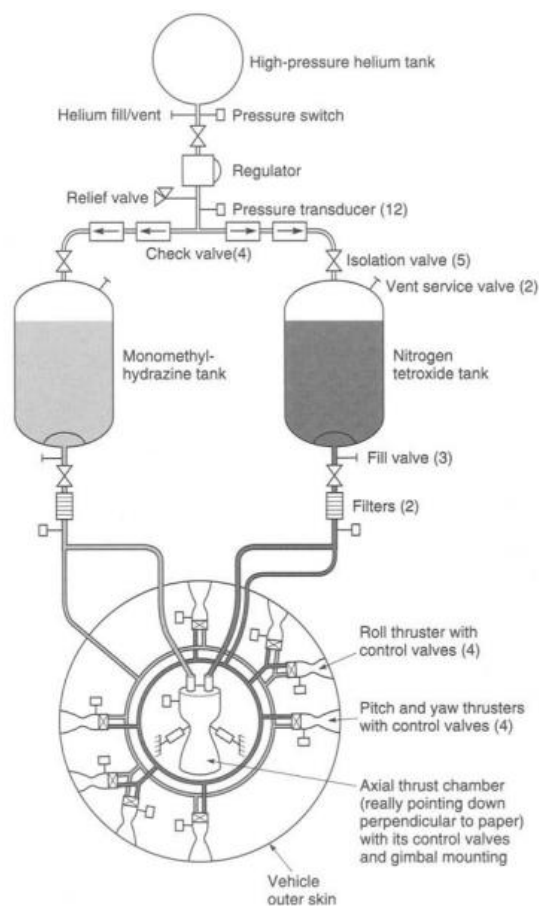


Figure 2-12: Regulated pressurisation system (Hearn, 1995)

Disadvantages of the regulated system include a greater number of active components (Hearn, 1982). An increased number of potential leak sites and greater complexity and cost. A relief valve safeguards against a major regulator malfunction to prevent excessive propellant tank pressures.

The size of the propellant tanks is increased to accommodate the pressurising gas in the blowdown pressurisation system shown in Figure 2-13 (Hearn, 1995) (Sutton & Biblarz, 2010). The ullage pressure decay that occurs during propellant outflow characterises the blowdown system of operation. There is no need for a regulator, isolation valve, or pressurant tank in this system (Lee & Ramirez, 1975).

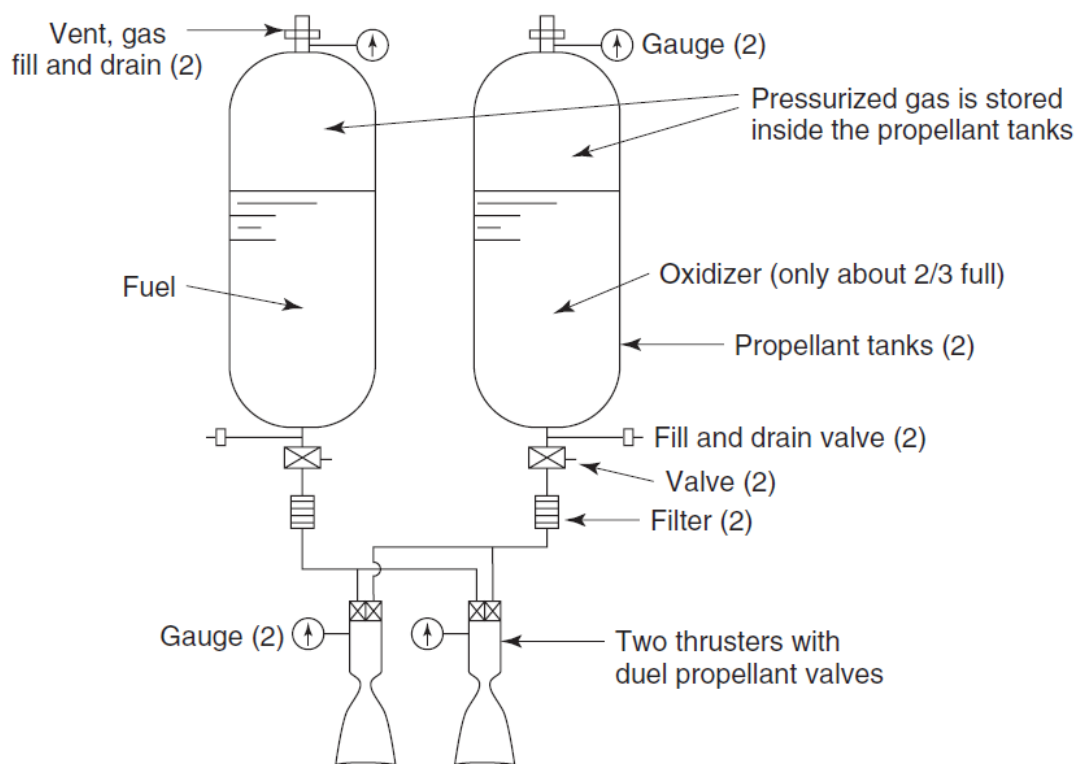


Figure 2-13: Blowdown pressurisation system (Sutton & Biblarz, 2010)

Pressurant gas solubility is an essential factor in blowdown systems where the propellant and pressurant are in contact (Hearn, 1982). As the propellants are expended, the pressure and thrust decrease in this system. As a result, a pressure-fed blowdown is not feasible for missions where the engine is intended to perform at a set chamber pressure (Sutton & Biblarz, 2001).

2.5.3. Anti-Slosh Baffles

The oscillations and side accelerations of vehicles in flight can cause the liquid in the tank to shift highly dynamically or “slosh” (Morton, et al., 1990). When a vehicle is experiencing side accelerations, zero-g, or negative-g during flight, emptying the propellant tank can be challenging (Sutton & Biblarz, 2010). While the tank is partially empty, sloshing can uncover the tank outlet, allowing gas bubbles to enter the propellant discharge lines (Morton, et al., 1990), potentially resulting in severe combustion problems (Pocha, 1986).

The sloshing forces can interact with the launch vehicle's structure when the sloshing frequency matches the dynamic control frequency. This can result in structural component failure or a significant divergence from the vehicle's intended flight path (Yang, 2015). As a result, it is critical to provide enough damping of fluid motion and slosh forces in the propellant tank and create methodologies for accounting for damping in vehicle performance analysis.

Under these conditions' special devices and special types of tanks are required. In tanks experiencing modest side accelerations, a series of internal baffles are often used to reduce the extent of sloshing and propellant vortexing. The vortexing phenomenon is similar to the effects of Coriolis force in bathtubs being emptied and can be intensified if the vehicle spins or rotates in flight (Sutton & Biblarz, 2010) (Yang, et al., 2017). This effect may result in propellant flowing into the engine with vapour or gas, which has the potential to cause combustion instabilities or result in engine failure.

The geometry, position and number of baffles are usually determined experimentally using an equivalent mass-pendulum-dashpot mechanical model (Pérez, et al., 2012). A tank model for Ares I for the United States (US) Orion spacecraft featuring anti-slosh ring baffles is shown in Figure 2-14 (Pérez, et al., 2012). presents the experimental data of sloshing ring baffles for various launch vehicles concerning tank diameter (D), the distance between the baffles (h), baffle width (w) and the ratio of tank radius to baffle width (w/R). From the data reviewed, the spacing of baffles is equivalent to the tank's diameter, and the common value of the baffle's geometric ratio is 0.1.



Figure 2-14: Anti-slosh ring baffles in the Ares I US liquid hydrogen tank model (Pérez, et al., 2012)

An investigation conducted by NASA in the late 1960s, titled “*Effectiveness of Flexible and Rigid Ring Baffles for Damping Liquid Oscillations in Large-scale Cylindrical Tanks*”, considered 762 mm and 2840 mm diameter rigid tanks fitted with rigid and flexible annular ring baffles (Stephens & Scholl, 1967) as present on Table 2-2. The slosh model for Ares I US spacecraft LOX and LH₂ propellant tanks' anti-slosh baffles parameters are also incorporated (Pérez, et al., 2012). The models consist of either mass-spring-dashpot systems or mass-pendulum-dashpot systems and are designed such that they have the same resultant pressure force, damping, moment, and frequency as the actual systems

Table 2-2: Anti-Slosh baffles design parameters (Stephens & Scholl, 1967) (Pérez, et al., 2012)

Description	Propellant	Reference	Diameter (mm)	h (mm)	Width (mm)	w/R
Large-Scale Cylindrical Tanks	N/A	Effective of Flexible and Rigid	2840	2840	142	0.1
Large-Scale Cylindrical Tanks	N/A	Effective of Flexible and Rigid	762	558	38.1	0.1
Ares I US	LOX	Validation of Slosh Model	1122	718	46	0.082
Ares I US	LH2	Validation of Slosh Model	1092	1115	112	0.204

2.6. NASA Propellant Tank Design Guidelines

Propellant tanks are used not only to store propellants, which make up roughly 90% of the rocket's launch weight but also serve as the primary bearing structures of a launch vehicle (Xin, et al., 2019). High-efficiency tank design is critical to maximising payload capacity.

The NASA propellant tank design guidelines recommend that the propellant tank's wall thickness be determined based on stresses due to internal pressure loads and discontinuities (Huzel & Huang, 1967). Internal pressure usually presents worst-case loading for propellant tanks which do not form part of the vehicle fuselage (Douglass, et al., 1974). For optimum tank design, the tank's wall thickness is obtained by combining local membrane (circumferential and longitudinal), bending and discontinuity stresses. The typical nomenclature associated with a pressure vessel is illustrated in Figure 2-15 (Huzel & Huang, 1967).

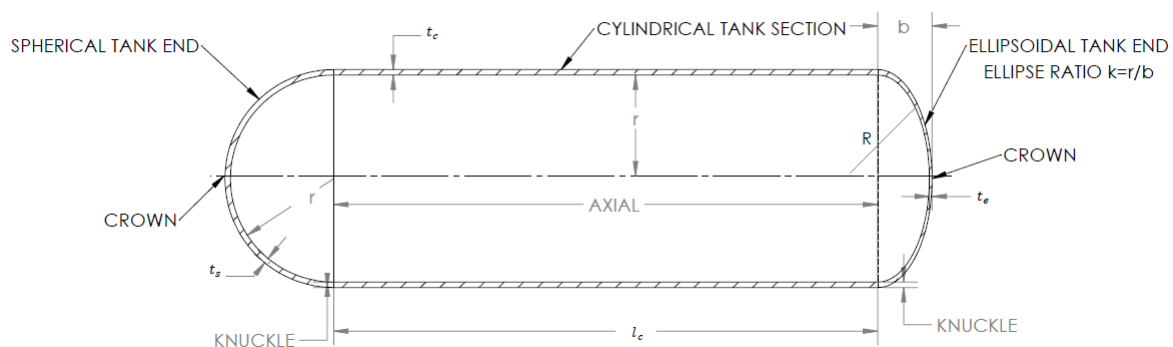


Figure 2-15: Pressure vessel nomenclature (Huzel & Huang, 1967)

The combination of usable propellant volume and other volume requirements determines a propellant tank's size or capacity. The total volume of the tank incorporates the propellant and ullage volume. The term "ullage" refers to the extra volume occupied by the gas above the propellant in sealed tanks. The ullage volume typically ranges from 3% to 10% of the tank volume.

The volume of the tank's cylindrical section volume (V_c), ellipsoidal tank end volume (V_e) and spherical tank end volume (V_s) are calculated according to equations 2-1, 2-2 and 2-3, respectively.

Where l_c is the length of the tank's cylindrical section, r is the tank's radius and b elliptical tank end minor radius.

$$V_c = \pi r^2 l_c \quad 2-1$$

$$V_e = \frac{2\pi r^2 b}{3} \quad 2-2$$

$$V_s = \frac{2\pi r^3}{3} \quad 2-3$$

The safety factors against the yield (S_y) and tensile (S_u) strengths of the material are 1.1 and 1.35, respectively. The allowable stress (S_w) on the tank is then taken to be the lowest value obtained from equations 2-4 and 2-5.

$$S_w = \frac{S_y}{1.1} \quad 2-4$$

$$S_w = \frac{S_u}{1.35} \quad 2-5$$

2.6.1. Internal Loading of The Tank

The tank's wall thickness (t) is obtained by applying the allowable working stress on the hoop and circumferential stress equations (Huzel & Huang, 1967). These equations are derived from pressure vessel theory and accommodate the weld efficiency (e_w), safety factor and knuckle stress factor (K) as per equations 2-6 to 2-12. The weld efficiency for the steels is assumed to range from 85% to 95% (Huzel & Huang, 1967).

The propellant tank parameters shown in Figure 2-15 are obtained using the following equations:

$$t_c = \frac{Pr}{S_w e_w} \quad 2-6$$

$$t_k = \frac{KPr}{S_w e_w} \quad 2-7$$

$$t_{cr} = \frac{PRr}{2S_w e_w} \quad 2-8$$

$$k = \frac{r}{b} \quad 2-9$$

$$R = kr \quad 2-10$$

$$t_e = \frac{(t_k + t_{cr})}{2} = \frac{Pr \left(K + \frac{k}{2} \right)}{2S_w} \quad 2-11$$

$$t_s = \frac{Pr \left(K + \frac{1}{2} \right)}{2S_w} \quad 2-12$$

In the above equations, t_c is the thickness of the tank's cylindrical section, t_k is the knuckle wall thickness, t_{cr} is the crown wall thickness, t_e is the ellipsoidal tank end wall thickness, t_s is the spherical tank end wall thickness, and P is the tank design internal pressure.

The mass of the tank components, such as the cylindrical section and tank ends, are calculated as per equations 2-13, 2-14 and 2-16. The factor, E' , is calculated using equation 2-16. It can also be attained graphically using Figure A-1 in appendix I.

$$m_c = 2\pi r l_c t_c \rho \quad 2-13$$

$$m_e = \frac{\pi r^2 t_e E' \rho}{2k} \quad 2-14$$

$$E' = 2k + \frac{1}{\sqrt{k^2 - 1}} \ln \frac{k + \sqrt{k^2 - 1}}{k - \sqrt{k^2 - 1}} \quad 2-15$$

$$m_s = 2\pi r^2 t_s \rho \quad 2-16$$

2.6.2. Propellant Tank Flight Loading

The internal pressure load is used to estimate the thickness of the tank, which is then validated against other external loads experienced by the vehicle during flight. During the flight, launch vehicles are subjected to a combination of the following loads (Huzel & Huang, 1967) (Puhn & Ollusky, 1965):

- Axial thrust loads
- Bending moments induced by vehicle side accelerations, wind loads, and changing centre of gravity during flight
- Thrust vector control forces
- Aerodynamic forces
- Vibration
- Loads generated by the mounting arrangement of the engine
- Thermal loads

The inertial loading results from the axial thrust loads and aerodynamic drag forces. They result in compressive loading of vehicle structures, including propellant tanks. Aerodynamic lift forces cause the bending of a vehicle's airframe, as illustrated in Figure 2-16 (Newlands, et al., 2016). To analyse the lateral bending dynamics of a rocket, experimental research has demonstrated that the airframe can be conceptualized as a nonuniform (in stiffness and mass distribution) beam (Wood, 1961). The shear force and bending moment act normally to the neutral axis of the vehicle's beam approximation model. They are obtained by reaction forces

that can be computed at simple support positions at the intersection of the vehicle's components.

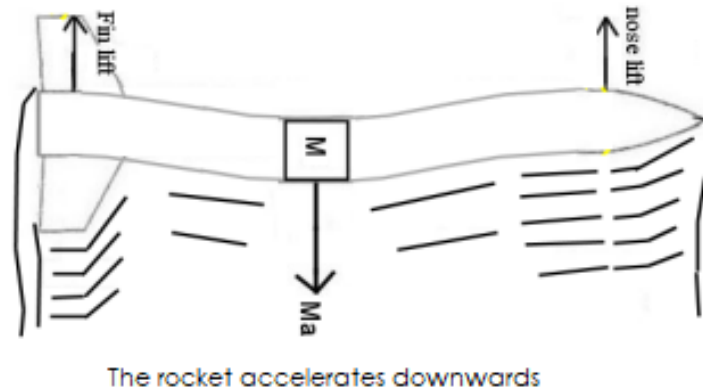


Figure 2-16: Schematic of aerodynamic lift forces (Newlands, et al., 2016)

Static vehicle mass on the launch pad, maximum dynamic pressure, maximum thrust, maximum axial acceleration, the combination of maximum dynamic pressure and maximum angle of attack, and re-entry are some of the primary load conditions used in vehicle structural analysis (Cerro, 1996). The axial load (A_x) at a given point, x , measured from the vehicle's nosecone tip, is computed as per equation 2-17 (Newlands, et al., 2016). The drag force computed according to equation 2-18 is highest at maximum dynamic pressure. Vehicle angle of attack induces lift forces on the nosecone and fins (in the case of finned vehicles), causing shear forces (V) and bending moments (M) on the vehicle. These can be computed at various locations using equations 2-19 and 2-20, respectively (Hutchinson, 2004).

$$A_x = -T + D_{nosecone,fuselage,fins} + a_x \sum_{x_0}^x m_x \quad 2-17$$

$$D_{nosecone,fuselage,fins} = 1/2 C_d \rho A V_x^2 \quad 2-18$$

Where T is the engine thrust, $D_{nosecone,fuselage,fins}$ is the aerodynamic drag, a_x is the acceleration of the vehicle and m_x is the mass of the vehicle's components at the location, x . Where C_d , A , V_x are the vehicle's drag coefficient, cross-sectional area, and velocity, respectively. ρ is the air density at the respective altitude.

$$V = - \int w_y dx \quad 2-19$$

$$M = \int V dx \quad 2-20$$

Where w_y is the uniform distributed load of the vehicle's components.

Tank Buckling

Propellant tanks must also be designed against buckling due to loads acting externally. Huzel and Huang (1967) state that a cylindrical tank can undergo buckling if the pressure due to the flight loads is greater than the internal tank pressure (Huzel & Huang, 1967). Baker and Sechler's buckling criteria are useful for evaluating buckling unpressurised and pressurised tanks (Roylance, 2001) (Douglass, et al., 1974).

The NASA propellant tank design guidelines determine the critical stress due to loads acting on the cylindrical section and tank ends. A tank is considered short if the cylindrical section length (l_c) conforms to equation 2-21; otherwise, long if equation 2-23 is satisfied. Equations 2-22 and 2-24 are used to compute the critical pressure due to external loading in the tank's cylindrical section for short and long tanks, respectively. The critical pressure (P_{crc}) is the minimum internal pressure that the propellant tank should have to prevent buckling due to external loading.

$$l_c < 4.9r \sqrt{r/t_c} \quad 2-21$$

$$P_{crc} = 0.807 \frac{Et_c^2}{l_c r} \sqrt{\left(\frac{1}{1-\nu^2}\right)^3 \frac{t_c^2}{r^2}} \quad 2-22$$

$$l_c \geq 4.9r \sqrt{r/t_c} \quad 2-23$$

$$P_{crc} = \frac{Et_c^3}{4(1-\nu^2)r^3} \quad 2-24$$

In the above equations, E is Young's elastic modulus, and ν is Poisson's ratio of the material.

Equations 2-25 and 2-26 are used to calculate the critical pressure resulting from external loading on ellipsoidal and spherical tank ends, respectively.

$$P_{cre} = \frac{C_b 2Et_e^2}{R^2} \quad 2-25$$

$$P_{crs} = \frac{0.342Et_s^2}{r^2} \quad 2-26$$

Here, C_b is the buckling coefficient defined as a function of r/t_e , such that $0.05 \leq C_b \leq 0.10$.

Materials that possess high strength under compressive bulking conditions have a high elasticity modulus to density ratio and high compressive yield strength to density ratio (Shanley, 1960) (Bert & Hylar, 1962). Hence, the critical axial compressive stress (S_c) can be raised using a material with a higher elasticity modulus (E) as per equation 2-27. This equation computes the critical axial stress for the tank's cylindrical section.

$$S_c = \left[9 \left(\frac{t_c}{r} \right)^{1.6} + 0.16 \left(\frac{t_c}{l_c} \right)^{1.3} \right] E \quad 2-27$$

The ability of the tank's cylindrical section to withstand axial loads can be improved by the pressure stabilisation technique (Huzel & Huang, 1967). Pressure stabilisation of the tank reduces the minimum thickness of the cylindrical section required to withstand the external or flight loads. Equation 2-28 shows that the tank's internal pressure (P) is directly proportional to the critical axial compressive load, F_a .

$$F_a = \pi r^2 P \quad 2-28$$

Sechler's buckling criteria account for the critical axial stress when the tank is unpressurised or pressurised (Roylance, 2001). Equation 2-27 refers to the unpressurised tank condition. Tank pressurisation improves the tank's critical axial stress, as illustrated by equation 2-29.

$$S_c = (K_o + K_p) \frac{E t_c}{r} \quad 2-29$$

$$K_o = 9 \left(\frac{t_c}{r} \right)^{1.6} + 0.16 \left(\frac{t_c}{l_c} \right)^{1.3} \left(\frac{t_c}{r} \right)^{0.3} \quad 2-30$$

$$K_p = 0.191 \left(\frac{p}{E} \right) \left(\frac{r}{t_c} \right)^2 \quad 2-31$$

Pressurisation also minimises tank failures associated with excessive bending loads during flight. However, if the pressure drops below the critical value, which prevents failure under axial and bending loads, this will result in catastrophic failure of the tank by collapsing (Huzel & Huang, 1967). Alternately, the tank's cylindrical section can be designed to be self-supporting (Huzel & Huang, 1967). This can be made by fixing longitudinal and circumferential members or honeycomb structures to the cylindrical skin. The members may either be

stiffeners attached to the tank wall by welding or integrated with the wall by machining or chemically milling a thicker metal sheet.

2.7. Propellant Tank Material

2.7.1. General characteristics of 300 Series Stainless Steel

The composition of alloys determines the crystal structure and hence the properties of stainless steel. The phases present in the crystal structure of stainless steel are martensite, austenite and ferrite, as illustrated by the Schaeffler diagram in Figure 2-17 (Leffler, 1996). The Schaeffler diagram shows that 301 SS composes both martensite and austenite structures unlike 304 SS, which has a stable austenitic structure. The austenitic structure of 300 series stainless steel is promoted by the inclusion of nickel, carbon, and nitrogen.

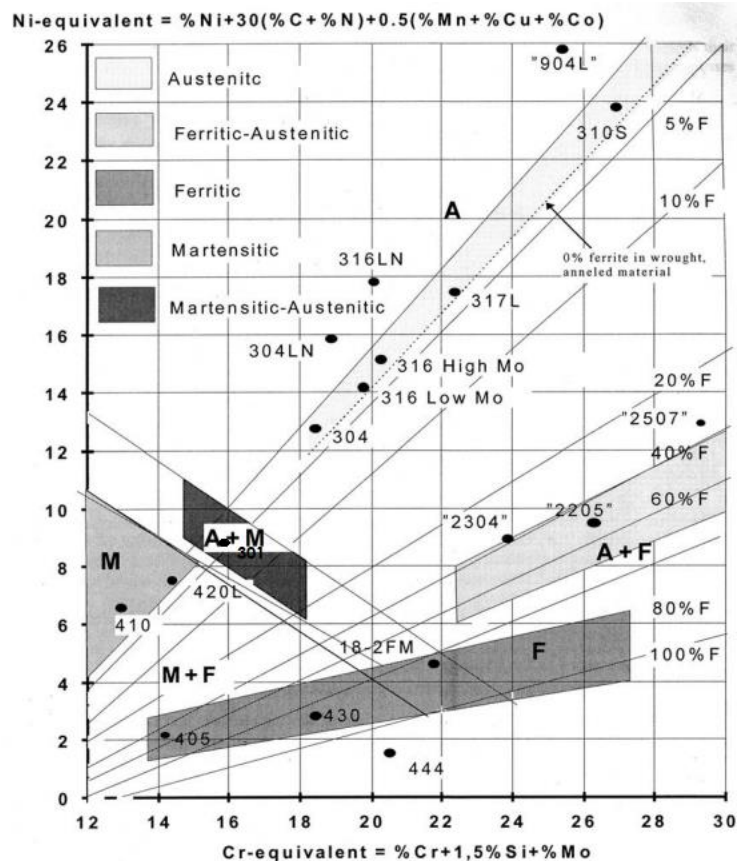


Figure 2-17: The Schaeffler Diagram for typical stainless steel (Leffler, 1996)

The chemical composition of 301, 301L, 304 and 304L stainless steels are presented in Table 2-3. Chromium refines the grain structure, improving toughness, ductility, corrosion resistance and hardness while increasing the critical temperatures range (Budynas & Nisbett, 2015). The combination of molybdenum and chromium alloying elements improves resistance to chloride penetration (Nickel Development Institute, 1991).

Table 2-3: Chemical composition for 300 series stainless steels (Nickel Institute, 2021)

Element	301 SS	301L SS	304 SS	304L SS
Carbon (C)	0.15	<0.03	0.08	0.03
Manganese (Mn)	2.00	2.00	2.00	2.00
Phosphorus (P)	0.045	0.045	0.045	0.045
Sulphur (S)	0.030	0.030	0.030	0.030
Silicon (Si)	1.00	1.00	1.00	1.00
Chromium (Cr)	16.00/18.00	16.00/18.00	18.00/20.00	18.00/20.00
Nickel (Ni)	6.00/8.00	6.00/8.00	8.00/12.00	8.00/12.00

Although the Schaeffler-DeLong diagram was created for welding, it can also be used for heat treatments. The austenitic structure is characterised by ductility and toughness (Nickel Institute, 2021). The minimum nickel content required to stabilise the austenitic structure at room temperature and below is 8 %. Type 304 SS is sometimes referred to as 18/8 as it contains 18 % and 8% of chromium and nickel, respectively. Austenitic stainless steels with higher nickel content, such as 304 SS, are more stable (Christian, et al., 1965).

2.7.2. 301 Stainless Steel Properties

The material proposed for the propellant tank manufacture in this research project is 301 stainless steel from the 300 series group, referred to as austenitic stainless steel. The selection of stainless steels for manufacturing propellant tanks for launch vehicles is based on the following factors (Douglass, et al., 1974) (Kendall, 1964):

- Strength to weight ratio (room and cryogenic temperature)
- Toughness (room and cryogenic temperature)
- Compatibility with liquid oxygen
- Formability
- Weldability
- Availability
- Comparative cost

This stainless steel alloy can be hardened, strengthened, and slightly magnetised through cold working and possesses excellent corrosive resistance (Nickel Development Institute, 1991). It is compatible with cryogenic propellants such as liquid oxygen and hydrogen. Naturally, propellant tanks cannot be made of materials susceptible to catastrophic chemical reactions with powerful oxidisers (Kendall, 1964). Various tests of ignition of LOX or GOX contained in

thin-walled 301 stainless steel LOX tanks proved that this austenitic stainless steel has no risk of ignition (Christian, et al., 1963) (Kimzey, 1970).

2.7.3. Work Hardenability

Because of its superior work-hardening qualities, type 301, also referred to as metastable stainless steel, is the most commonly utilized stainless steel at high-strength levels in aeroplanes and missiles (Muraca & Whittick , 1972). Heat treatment will not harden the alloy; nevertheless, cold work will harden it rapidly. At room temperature, tensile strengths can be increased to 1900 MPa (INCO, 1962) (Muraca & Whittick , 1972).

Cold working improves hardness, elasticity, and strength properties, conversely reducing ductility. This makes forming operations more challenging, depending on the degree to which cold work is to be performed (INCO, 1962) (Bullens, 1949) (Nickel Development Institute, 1991). The ratios of alloying elements (chromium, nickel, carbon, etc.) in the steel impact its response to cold working. The increase of nickel present in the steel makes it more stable while reducing the rate of cold working (Muraca & Whittick , 1972). 301 SS has better elongation than 304 with increased cold working (Hanson, 1961) (Gasparini, 2018). Hence, the lower the nickel composition, the greater the rate of cold work.

301 SS is best suited to applications where high strength and good corrosion resistance are required. When annealed, metastable stainless steels have an austenitic structure, but during plastic deformation, they partially transition to martensite (Hedström, 2005). The martensite structure is harder and stronger than the austenitic structure, resulting in composite strengthening and, as a result, increased strain hardening (Hedström, 2005).

Of interest, the minimum values of yield and tensile strengths at various work-hardening conditions ($\frac{1}{4}$, $\frac{1}{2}$, $\frac{3}{4}$ hard) are the same for 201, 301, 304, and 316 stainless steels, with only the elongation different amongst them (ASTM, 2003). 301 SS has superior elongation in all cold working conditions (Gasparini, 2018). The relationship between the mechanical properties of 301 SS and cold work percentage is illustrated in Figure 2-18 (ATI, 2014). Table 2-4 shows the minimum mechanical properties of work-hardened 301 SS at various rates.

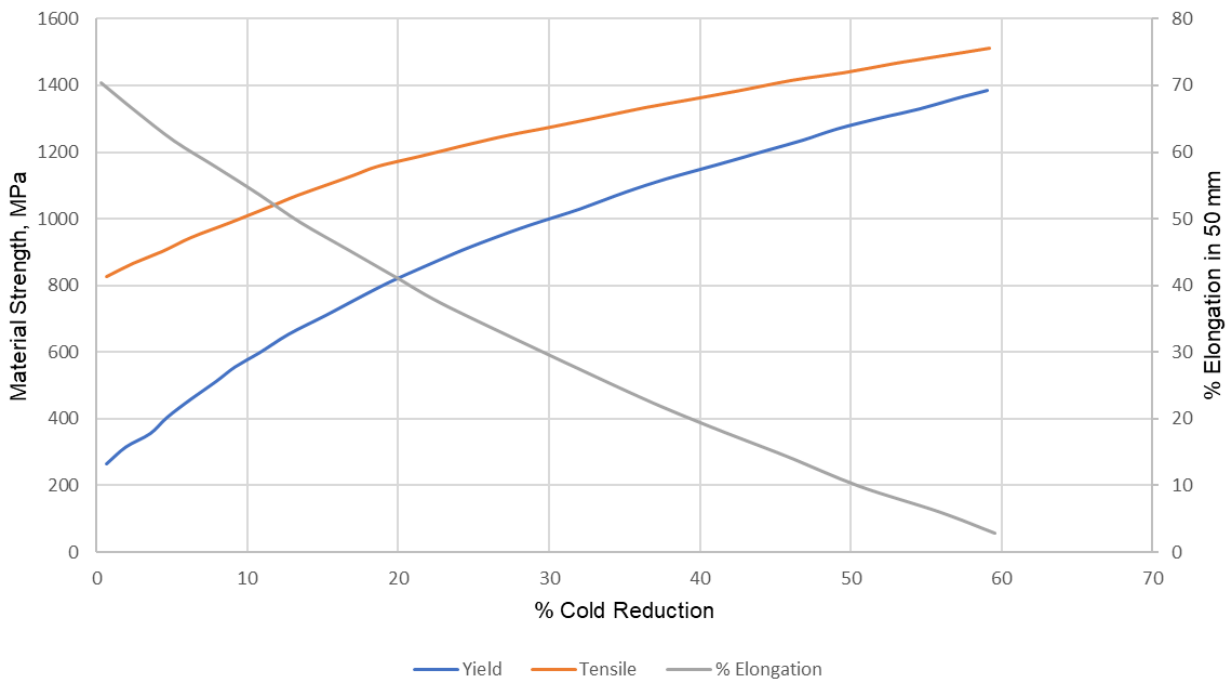


Figure 2-18: Cold worked 301 SS mechanical properties (ATI, 2014) (Nickel Institute, 2021)

Table 2-4: 301 SS mechanical properties (ASTM, 2003) (Stal, 2018)

Hardened State	Yield Strength (MPa)	Tensile Strength (MPa)	Elongation in 2 in. or 50 mm (%)
Annealed	205	515	40
¼ Hard	515	825	25
½ Hard	760	1035	18
¾ Hard	930	1205	12
Full Hard	965	1275	9

Austenitic stainless steels exhibit better ductility and toughness at high strengths than other steels, which are retained even at cryogenic temperatures (Nickel Development Institute, 1991). Austenitic stainless steels possess superior toughness at cryogenic temperature than at room temperature (Mann, 1978). Figure 2-19 indicates how the yield and tensile strengths of 301 stainless steel increase with a decrease in temperature for both cold worked and annealed metal (McClintock & Gibbons, 1960). In contrast, elongation is reduced for both annealed and cold-worked cases.

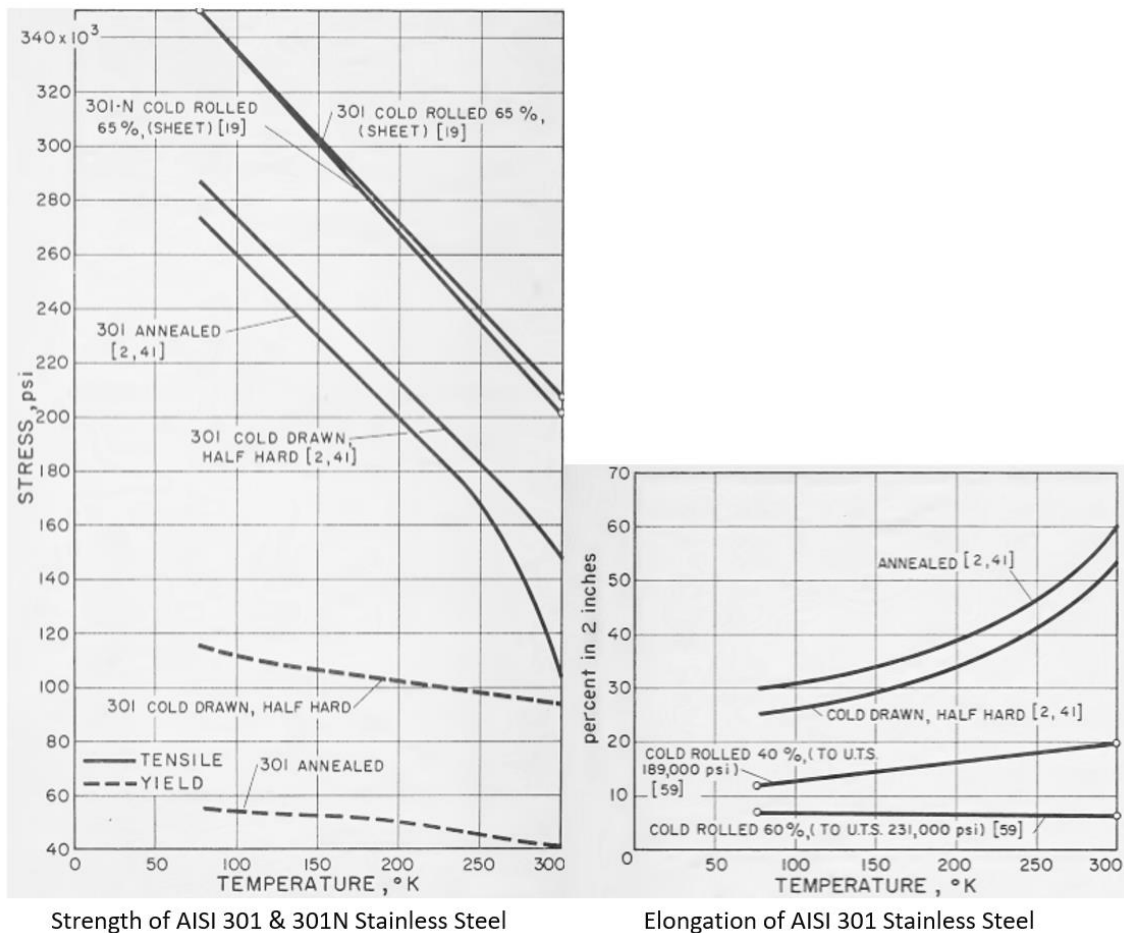


Figure 2-19: Cold worked 301 SS mechanical properties versus temperature (McClintock & Gibbons, 1960)

2.7.4. Metal Spinning

Tank domed ends can be shaped and formed by spinning, drawing, forging, and segmenting (Douglass, et al., 1974). Although available equipment is limited, the shear spinning method gives better thickness control and is suitable for thick material. Large sizes can be fabricated through segmenting, but this method imposes high tooling, welding, and inspection costs.

The metal spinning process involves gradually shaping a circular metal sheet over a mandrel under the application of localised pressure by a roller that moves axially over the sheet's outer surface to produce a symmetrical component (Šugár, et al., 2016). The workpiece is forced back towards the mandrel with a type of spinning tool, and a part is produced taking the form of the mandrel geometry as shown in Figure 2-20 (Boyer & Gall, 1985) (Lange, 1985) (GI Metal Spinning, 2019). Benefits of the spinning process include simplified tooling, low tool costs, good internal and external surface quality, tight dimensional accuracy, and good mechanical properties of the components produced (Hiuhu, 2015). Different sheet sizes can

be processed, with blank diameters ranging from 300 mm to 10 m and thicknesses ranging from 0.4 mm to 25 mm (Hiuhu, 2015).

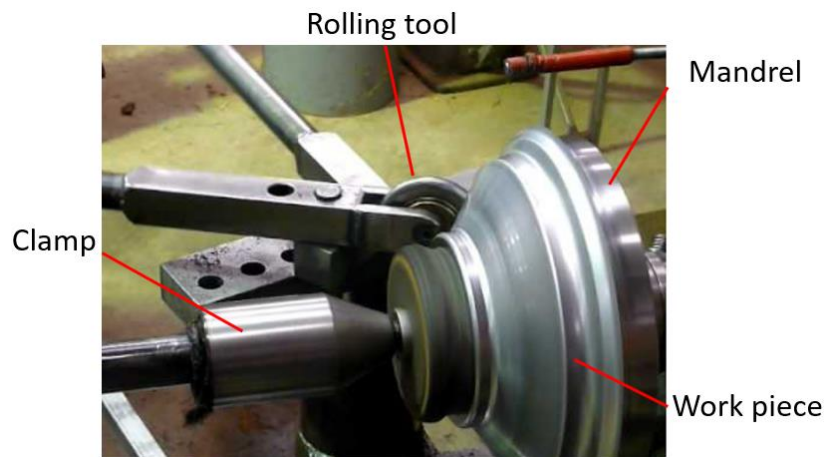


Figure 2-20: Setup of the spinning process (*GI Metal Spinning, 2019*)

The number of tool passes, the offset of each pass from the other, the tool feed ratio, the shape of the produced part, roller nose radius, friction, and the first tool pass trajectory are all factors that influence the thickness distribution of spun parts, according to current experimental studies (Wang, et al., 2011) (Sugar, et al., 2012) (El-Khabeery, et al., 1991). To reduce thinning during the metal spinning process, it is proposed that a greater number of less aggressive passes be used (Polyblank & Allwood, 2015).

Metals harden as they are worked, which sometimes necessitates annealing the piece partway through a spinning operation, but often this is not necessary (Fletcher, 1995) (Yaoyi SS, 2021). Although the cold working of the alloy increases its strength and hardness properties, its ductility is reduced. Forming operations becomes more challenging in proportion to the rate of cold work performed on the material (Muraca & Whittick , 1972).

Springback

When a metal is cold formed, the part returns to its original shape after removing the forming tool, as illustrated in Figure 2-21 (Fritz, 2020). This tendency is termed “springback,” and cold forming operations must compensate for it to achieve the desired final shape (Fritz, 2020). The amount of springback will increase with increased strength and work hardening rate. Standard grades with low austenite stability, such as Type 301 and nitrogen alloyed grades, have improved yield strength and higher work hardening rates, resulting in a more considerable amount of springback (Fritz, 2020).

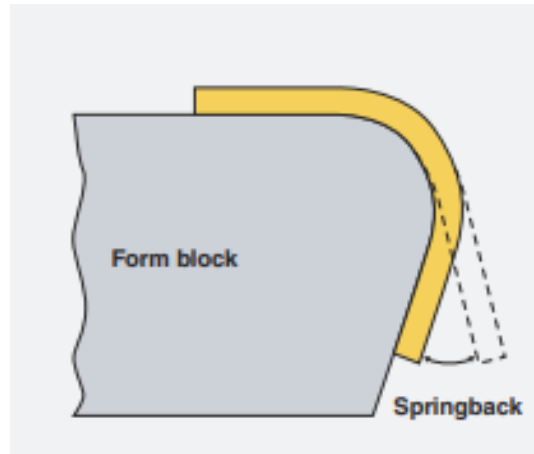


Figure 2-21: Springback phenomenon (Fritz, 2020)

Sheet Rolling

A given propellant tank's cylindrical section can be fabricated through rolling, welding, and shear spinning (Douglass, et al., 1974). Rolling and welding are common approaches because they are simple, low cost, and allow large sizes to be manufactured. The sheet rolling machine consists of the top roller being fixed while the bottom rollers are adjusted vertically to accommodate varying material thickness, as illustrated in Figure 2-22 (Fritz, 2020). The third roll is adjusted angularly to set the angle of the bend. During rolling operations, springback can be compensated for by using a larger bending angle to “over bend” the metal so that the desired final angle is obtained when the bending force is removed.

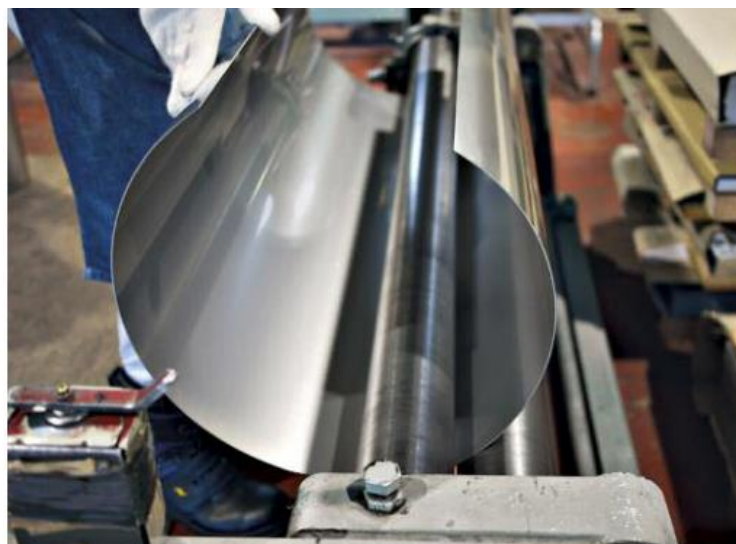


Figure 2-22: Rolling process (Fritz, 2020)

2.7.5. Welding Operations

Almost all stainless steel alloys can be welded by the major welding techniques used in industry. Such techniques include arc welding, resistance welding, friction welding, electron, and laser welding. In welded products, it is often essential to preserve corrosion resistance in the weld and the heat-affected zone (Nickel Development Institute, 1991). Typical challenges associated with welding austenitic stainless steel include hot cracking of the welded metal and heat-affected zone sensitisation.

Laser Welding

Laser welding is an autogenous process as no filler material is used to perform welding. Ideally, the metals to be welded should have an interference fit so that the beam does not escape through the joint, but this is not always possible. In laser welding, the joining of metals is achieved through a non-contact process meaning there is no contact between the materials being joined and the welding tool (Orlianski, 2020). The laser light heats and melts the material in its vicinity rapidly, forming the weld after the material cools. Laser welding is compatible with carbon steel, stainless steel, aluminium, and titanium. This joining method is common in the aerospace, automotive, medical, and manufacturing industries.

Austenitic stainless steels joined using gas tungsten arc welding (GTAW/TIG) are more likely to suffer carbide precipitation than those joined by laser welding. Laser welding ensures high weld quality and reduces thermal distortion by minimising heat input. Variables for laser welding include laser power, welding speed, type of shielding gas and defocusing distance. A typical laser welding setup is shown in Figure 2-23 (Guo, et al., 2015).

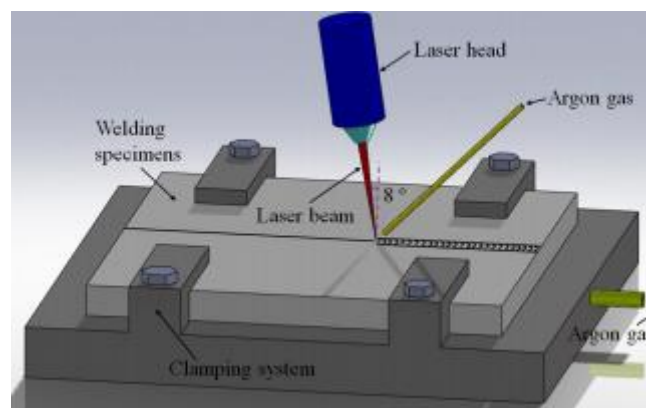


Figure 2-23: A representation of a laser welding setup (Guo, et al., 2015)

The laser operating mode depends on the power density at which the laser spot is focused on the weldment (Mazmudar & Patel, 2014). Three welding modes that can be employed are 1)

conduction mode, 2) conduction/penetration mode, and 3) penetration/keyhole mode, as illustrated in Figure 2-24 (Orlianski, 2020). In conduction mode, the weld achieved is shallow and wide as it is performed at low energy density.

The penetration/keyhole mode provides deep and narrow welds. In this mode, laser light is delivered efficiently into the material in the form of vaporised material filament called a “keyhole” (Orlianski, 2020). Energy transfer to the material does not depend on conduction to achieve penetration; therefore, heat into the material and the heat-affected zone is also reduced.

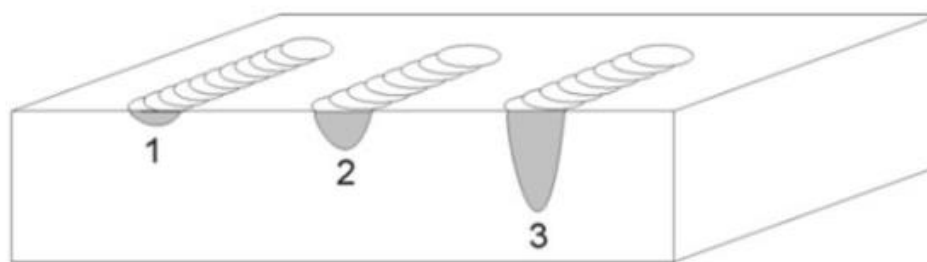


Figure 2-24: Types of welds offered by laser (Orlianski, 2020)

For better joining results, it is recommended that the gap between the materials to be joined should be less than 10 % of the smallest thickness of the weldment (Orlianski, 2020). Figure 2-25 illustrates the joint types attained through laser welding, including butt, lap, and fillet welds (Orlianski, 2020). Neodymium-doped yttrium aluminium garnet (Nd: YAG) laser welding can be performed as a pulsed or continuous wave (Orlianski, 2020). In pulsed laser welding, welds are created by individual pulses and high peak power. This type of laser is energy efficient and results in a small heat-affected zone.

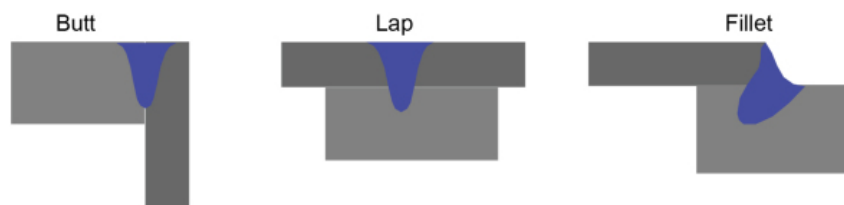


Figure 2-25: Most common laser joint types (Orlianski, 2020)

Tungsten Inert Gas (TIG) Welding

Tungsten Inert Gas (TIG) welding is an electric arc welding technique where fusion energy is generated by an electric arc bridging between the weld metal and a tungsten electrode (Raina & Awasthi, 2020). Inert shielding gas is employed during this process to protect the arc,

electrode, and weld pool from the atmospheric air, as illustrated in Figure 2-26 (Raina & Awasthi, 2020). Unlike other fusion welding processes like Metal Inert Gas (MIG) and Metal Active Gas (MAG), the electrode is not consumed during welding. TIG welding is distinguished by high-quality weld metal deposits, high precision, high-quality surfaces, and high strength (Sandberg & Laren, 2004). Welds can be performed manually or automatically.

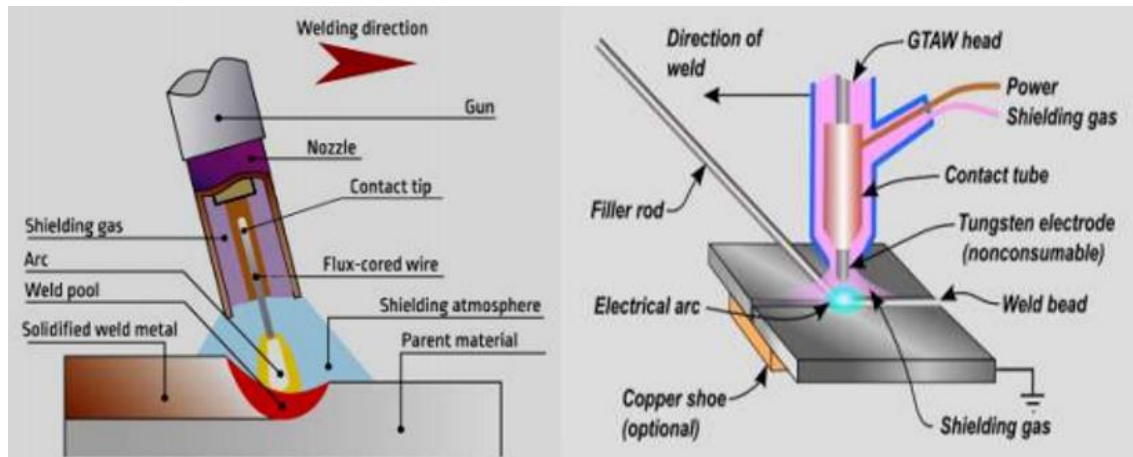


Figure 2-26: Tungsten Inert Gas (TIG) welding setup (Raina & Awasthi, 2020)

In welding stainless steel, shielding gases such as pure argon, helium, or mixes of the two are employed. Argon is the preferred shielding gas for manual welding and connecting sheets with a thickness of less than 1.6 mm (Pierre-Jean, 2007). Its use results in better penetration and less melt-through compared to helium at lower flow rates.

To achieve a high-quality weld with the strength above the parent material, the following considerations must be taken into account (Technoman, 2011):

- the distance between the torch and the joint to be formed
- usage of appropriate fluxes or gas protection for the welded material
- a heat energy level that is acceptable for the size of the joint being produced
- the rate at which the filler material is fed
- the potential for the joint to be tack welded

The toughness of 316L welds produced using tungsten inert gas (TIG), submerged arc (SA), and gas metal arc (GMA) welding methods was found to be 181 MPa.m^{1/2}, 103 MPa.m^{1/2}, and 161 MPa.m^{1/2}, respectively, in an experiment conducted at 4 K (-269 °C) by Whipple and Kotecki in 1981 (Whipple & Kotecki, 1981). Hence, the TIG welding method produces a weld with superior toughness under cryogenic conditions.

Due to the relatively low thermal conductivity of austenitic stainless steel alloys, approximately half that of carbon steels, welding heat is not dissipated swiftly through the alloy (Nickel Development Institute, 1991). Also, their coefficient of expansion is higher than carbon steel; hence they are prone to significant thermal expansion and contraction (Nickel Development Institute, 1991).

Heat concentration can be minimised using the skip-weld technique, lower weld current settings, appropriate cooling methods, or proper joint design. The skip welding method, illustrated in Figure 2-27, helps reduce warping and evenly distributes heat along the welded metal (Miller, 2017). Preheating is unnecessary for austenitic stainless steel, although post-heating may be necessary only to redissolve precipitated carbides.



Figure 2-27: Skip welding (Miller, 2017)

When austenitic stainless steel is heated within the 427 to 871°C temperature range, chromium carbide production and precipitation at grain boundaries in the heat-affected zone cause sensitisation (Kotecki & Armao, 2003) (Hitchcock & Jordan, 2007). To limit the quantity of carbon accessible to mix with chromium, low carbon base and filler materials are used to mitigate this problem. The degree of carbide precipitation increases in proportion to (Kotecki & Armao, 2003):

- Carbon content – Grades 301 and 302, for example, have a maximum carbon concentration of 0.15 percent, making them more susceptible to carbon precipitation than grade 304, which has a maximum carbon content of only 0.08 percent).
- Time at the critical mid-range temperatures – For instance, a few seconds at 649°C, for instance, can cause greater harm than a few minutes at 454°C or 788°C.

Carbon will diffuse and create carbide precipitates if austenitic stainless steels are held at intermediate temperatures (between 500°C and 950°C). The chromium carbide (Cr_{23}C_6)

precipitation occurs mainly at grain boundaries, resulting in a Cr deficient zone. Due to this Cr deficient zone (sensitisation), the steel will be more susceptible to intergranular corrosion (Hedström, 2005). Sensitisation can be minimised by reducing the carbon composition to restrict chromium carbides ($Cr_{23}C_6$) and increasing the Cr and Mo content (Lula, 1986). Reheating the steel to dissolve the chromium carbides is also an approach used.

The amount of carbon, the exposure temperature, and the time spent at this temperature determine the degree of sensitisation, as illustrated in Figure 2-28 (Hitchcock & Jordan, 2007). Sensitisation occurs from the temperature of 700 °C. It occurs most rapidly for an alloy with 0.062 % carbon content in as little as two to three minutes. An alloy (304L SS) with 0.030 % carbon content, on the other hand, can withstand a temperature of 600°C for eight hours without sensitisation (Hitchcock & Jordan, 2007). Hence, low carbon “L” grades are more weldable and produce quality welds.

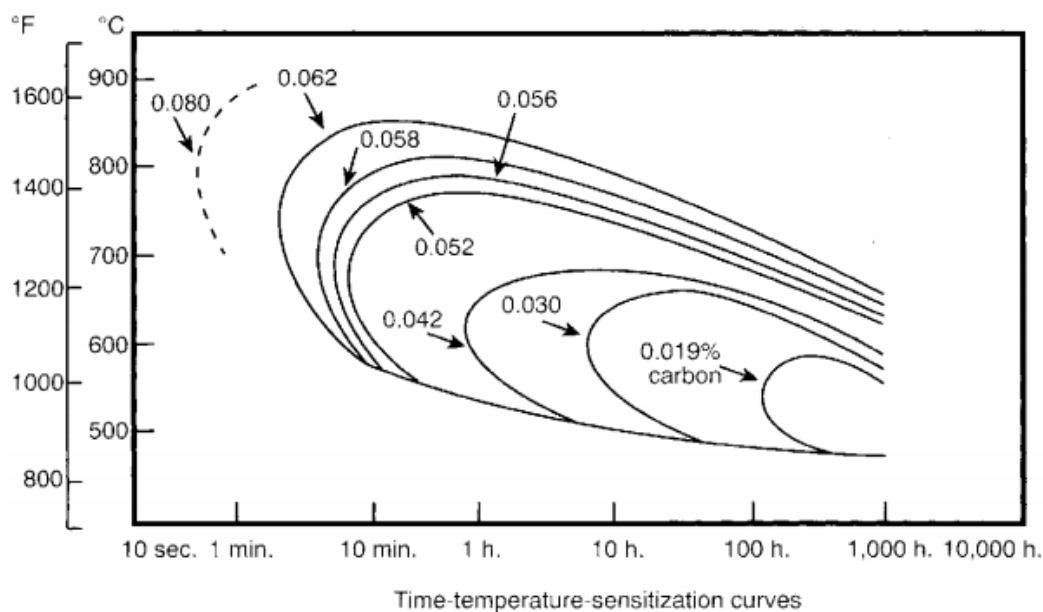


Figure 2-28: Effect of carbon control on carbide precipitation in 304 SS (Hitchcock & Jordan, 2007)

At cryogenic temperatures, sensitisation, or the precipitation of chromium carbides at the grain boundary, affects alloy toughness (Read, et al., 1980). As a result, cryogenic applications frequently use alloys with very low carbon content, such as 308L (0.04% C, max.) and 316L (0.03 percent C, max.). Using low carbon filler metals to prevent sensitization, balancing weld-metal chemistry to avoid ferrite, and inert-gas-shielded welding procedures or basic fluxes to reduce oxide inclusions can help improve weld-metal toughness (McHenry , 1983).

Filler metals for austenitic stainless steels should match the base metal and enable a microstructure with some ferrite to prevent hot cracking (Kotecki & Armao, 2003). 301 stainless steel is suitable for most welding techniques, with 308 stainless steel recommended as the filler metal/material, as it is in the case of grades 302, 304 and 305.

2.8. Summary

In general, launch vehicles most frequently employ spherical vessels for pressurant containment and tandem tanks to contain propellants. In the tandem tank arrangement, the propellant feedline from the tank above can run internally within or external to the tank below. The Saturn V booster stage, S-IC, had the LOX tank above the kerosene tank with the feedline from the top tank running internally through the kerosene tank. The air gap between the LOX feedline and the internal duct of the kerosene tank was enough to prevent gelling of kerosene.

The longer propellant tank and denser propellant are placed above the other propellant tank to reduce the length of feedlines and improve the vehicle's stability margin, respectively. The tandem tank configuration incorporating a common bulkhead allows for significant weight reduction as it eliminates the need for the intertank structure and an additional bulkhead. However, the use of a common bulkhead raises the risk of catastrophic launch vehicle failure in the event of propellant leakage. Also, if an irreparable fault occurs during the manufacture of the second constituent tank, then the first constituent tank must be scrapped as well. Furthermore, a common bulkhead requires insulation if a cryogenic/non-cryogenic propellant combination is used.

The selection of the tank end geometry depends on the available manufacturing technology and costs. Spherical tank ends typically result in lighter but longer tanks. Conversely, elliptical tank ends typically result in shorter but heavier tanks. In terms of engine performance, a regulated pressurisation system for the supply of propellants to the engine is more favourable than a blowdown pressurisation system, as the tank pressure decreases over time in a blowdown system, which results in a decaying engine chamber pressure. A shared pressure regulator is recommended to eliminate any pressure differential in the tanks.

Tank pressurisation also improves a tank's resistance to buckling failure. It further minimises the tank's thickness required to overcome buckling or compressive stress. The Atlas V launch vehicle utilised tank pressurisation to prevent its monocoque propellant tanks from collapsing. Helium is commonly used as a pressurant due to its lower density and condensation temperature compared to nitrogen.

The NASA design guidelines for propellant tanks introduce safety factors that ensure lightweight structures. The safety factors of design stress against yield and tensile strength are 1.1 and 1.35, respectively. Flight loads experienced by launch vehicles include

aerodynamic, inertial, and thrust loads—these result in compressive forces, shear forces and bending moments being applied to vehicle structural elements.

301 stainless steel has been used to manufacture propellant tanks for launch vehicles such as the Atlas launch vehicle family and the Starship. The Spica rocket propellant tanks are made from 304 stainless steel. Its strength is increased after cold working or while operating under cryogenic conditions. 301 SS has an unstable austenitic structure which enhances its work hardening rate during cold work.

301 SS can be spun and rolled into various geometries. The spinning process is commonly used for manufacturing tank ends. This forming operation typically reduces material thickness and increases material hardness, which may require intermediate annealing to permit further deformation. Unstable austenitic grades such as 301 tend to experience the springback effect during spin forming due to their high work hardening rates.

The Tungsten Inert Gas (TIG) welding technique is suitable for welding stainless steel, and it is widely employed. It also produces welds with superior toughness even at cryogenic temperatures. The skip-weld method can be employed to minimise heat input when welding stainless steel to mitigate warpage and distortion due to the material's comparatively low thermal conductivity and a high coefficient of expansion. Sensitisation of the heat-affected zone can be mitigated by using filler material with low carbon content to enable a microstructure with some ferrite. 308/308L SS is a recommended filler material for welding 301, 302 and 304 stainless steel.

3. Propellant Tank Design Methodology

This chapter explains in detail the steps and considerations taken in developing the design procedure for liquid propellant tanks for STEVE. This design methodology aims to meet the research objectives by determining the preliminary propellant tank design, conducting material testing, performing the final propellant tank design, manufacturing a test tank and pressure testing the test tank to destruction.

3.1. Propellant Tank Design Process

A propellant tank's design process entails determining the tank shape or configuration based on the vehicle structure constraints. Material selection is performed thereafter and involves considering mechanical properties, chemical compatibility, fracture toughness, accessibility, costs, and manufacturing factors (Douglass, et al., 1974). The detailed design of the propellant tank and its components follows material selection.

The main design objective for a propellant tank is to enable the vehicle to achieve its expected velocity increment with its design payload under conditions of maximum reliability (Huzel & Huang, 1967). Design considerations depend upon the propellant type, vehicle mission requirement, propulsion system design, construction materials, and fabrication methods.

The STEVE feed system consists of at least two propellant tanks for fuel and oxidiser, another tank for a pressurant gas, various valves, filters, and provisions for filling and emptying. The design of the tank depends on the feed system used. Figure 3-1 shows the propulsion components for the suborbital test vehicle. STEVE will use a regulated pressurisation system consisting of the pressurant tank, pressure regulator and propellant tanks. As a design specification, helium will be used as the pressurant gas and is to be stored above the propellant tanks in a high-pressure spherical tank. In addition, the required pressure regulator is to be positioned between the propellant tanks and the pressurant tank.

The pressurant tanks will be sized based on commercially available sizes to meet the required pressurant quantity and tank pressure.

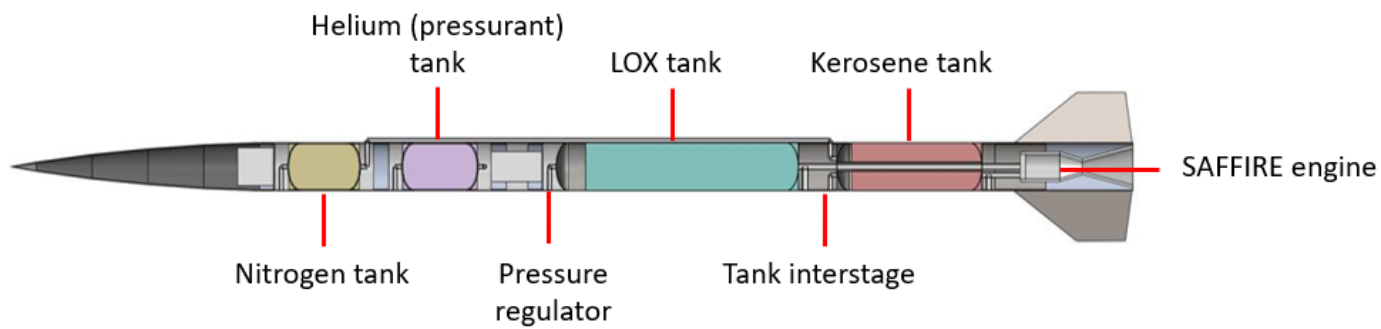


Figure 3-1: STEVE propulsion system components

This study's propellant tank design procedure comprised the following steps: generation of preliminary tank designs, material testing, manufacturing of the test tank, determination of the final tank design and pressure testing of the propellant test tank, as illustrated in Figure 3-2. The preliminary propellant tank design phase entailed the determination of the propellant tank's geometry, size and wall thicknesses based on simple analytical means.

The tank's geometry is cylindrical with elliptical ends to form an integral structure of the vehicle. The metal spinning company had an existing tool for spinning elliptical tank ends having a diameter of 386 mm. Having an existing tool was favourable as it reduced the manufacturing costs of the tank ends. Hence, the tool's availability for manufacture influenced the selection of the elliptical tank ends. This further determined the diameter of the tanks and, in turn, the diameter of the vehicle. This diameter was accepted because it was larger than the largest diameter envisaged for the SAFFIRE engine.

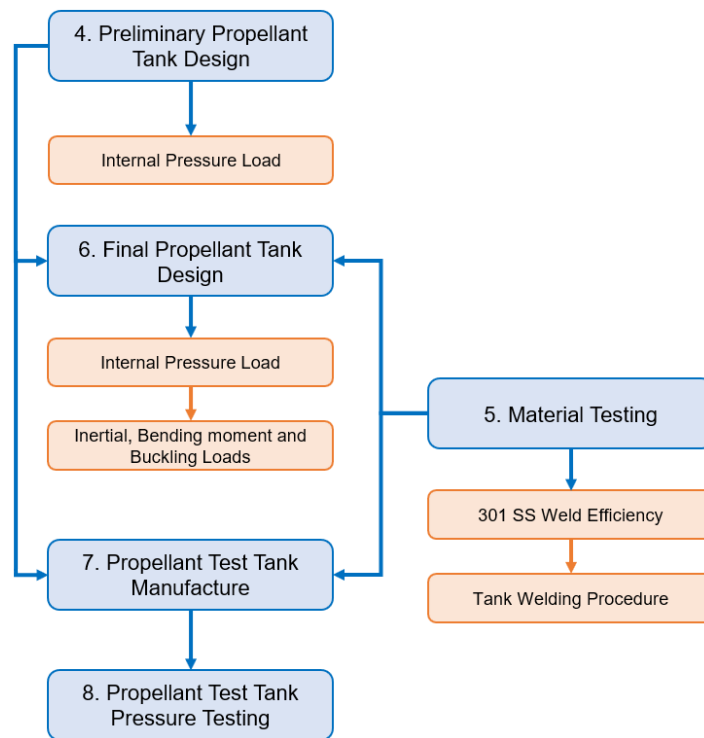


Figure 3-2: Development of the metallic liquid propellant tank design procedure

SAFFIRE engine performance parameters were used to determine the quantity of the propellants required to power the engine for the required burn time. Based on these quantities and the propellant densities, the lengths of the tanks were estimated. The chamber pressure and feed system type determined the tank's internal pressure. Using the NASA propellant tank design guidelines (Douglass, et al., 1974), the minimum wall thickness of each tank was estimated based on the specified internal pressure loading, the material properties of 301L SS, and certain geometric factors. This estimate relied on an assumed value for the expected weld efficiency of 301L SS.

Material testing was then undertaken to determine the proposed material's weld efficiency experimentally. The welding parameters and procedures were selected to cater for the difficulties of welding stainless steel and to produce high-quality welds. These parameters were determined from literature and other welding guidelines. The main challenges with welding stainless steels are thermal contraction and heat dissipation due to their high coefficient of expansion and low thermal conductivity, respectively, compared to other steels. Tensile tests were conducted on unwelded and welded specimens to compare the stress vs strain curves and determine the weld efficiency.

To determine the loads expected to be experienced by the propellant tanks during flight, six-degree-of-freedom flight dynamics simulations of the STEVE rocket were performed as part

of a separate postgraduate study (Sabbagha, 2022), using ASReG's Hybrid Rocket Performance Simulator (HYROPS) software (Chowdhury, 2012). Although HYROPS was initially developed for the simulation of hybrid rocket flight, its configuration flexibility allows it to simulate the flight of liquid rockets as well.

HYROPS allows individual modelling of a rocket's primary components, such as propellant tanks, pressurant tanks, propellants, nosecone, fins, payload bay, engine, and other components. The software also enables the incorporation of realistic wind profiles. The launch parameters required to perform the simulation include launch angle, direction and launchpad location. The output data or parameters include the flight profile, velocity vs time, acceleration vs time, thrust vs time, angle of attack vs time and stability vs time. Additional flight performance parameters can be computed from the simulator output data if required. In the case of this study, these flight performance parameters enabled the determination of flight loads used for more advanced finite element analyses.

The final propellant tank design was obtained once the actual weld efficiency of the material had been determined experimentally. The final tank wall thickness was obtained based on the above analyses incorporating the internal pressure and flight loads. The resulting stress predictions were evaluated against the weld and parent material strength to ensure that the designs met a minimum safety factor of 1.1 per NASA guidelines for propellant tanks for launch vehicles (Douglass, et al., 1974).

A propellant test tank was manufactured based on the preliminary propellant tank design and material testing results. The tank ends were manufactured using a metal spinning process. The tank's cylindrical section was rolled and subsequently welded using the TIG welding method. Weld Swagelok fittings were used to serve as tank ports for filling, pressurisation, venting and draining purposes.

Hydrostatic testing was performed on the test tank to evaluate its pressure-holding capacity and verify the design procedure used in its development. This test further verified the weld strength and the welding procedure specification. Water was used as the testing medium and was pressurised to reach key pressure thresholds to evaluate the occurrence and location of material yielding. These thresholds were calculated according to the weld and unwelded material yield and tensile strengths at annealed and $\frac{1}{4}$ hard conditions.

Final design recommendations for the liquid propellant tanks were then generated on the basis of the activities outlined above.

4. Preliminary Propellant Tank Design

4.1. Introduction

The preliminary propellant tank design aimed to indicate the required thickness of a 301L stainless steel sheet to commence the procurement process. An analytical design was performed to determine the tank's preliminary wall thickness based on the formulas prescribed by the NASA design guidelines for propellant tanks. This preliminary thickness was determined based on the internal pressure. The weld efficiency used in this analytical solution was based on the literature.

4.2. Propellant Tank Configuration and Design Specifications

The proposed propellant tanks will form an integral structure arranged in a tandem manner. Tanks will have a cylindrical section enclosed by elliptical ends, reducing the occupied space. The choice of an elliptical tank end was influenced by the availability of the mandrel, which reduced the manufacturing costs.

Metal Spinings (Pty) Ltd, a metal spinning company based in Randburg, had an existing elliptical mandrel of 386 mm diameter, shown in Figure 4-1. This diameter was accepted as it was larger than the diameter of the SAFFIRE engine. The volume of the tanks is determined by the engine performance parameters, namely the burn time and mass flow rate of propellants.



Figure 4-1: Elliptical tank end mandrel

For the sake of simplicity, a traditional tandem tank arrangement with separate bulkheads was selected. Typically, the tank housing the denser liquid propellant should be placed above that housing the less dense propellant to improve the vehicle's stability margin during flight (Borogove, 2021). For this study, LOX is the denser of the two propellants to be stored; hence the LOX tank was placed above the kerosene tank.

Due to the SAFFIRE engine’s oxidiser to fuel (OF) ratio, the volume of the LOX tank is significantly higher than that of the kerosene tank. In this regard, positioning the smaller kerosene tank beneath the larger LOX tank minimises feedline length and reduces overall weight. The resulting propellant tank configuration for the STEVE vehicle is illustrated in Figure 4-2. Here, the LOX and kerosene tanks are shown to be joined together by an “intertank” structure, with the LOX feedline running internally within the kerosene tank.

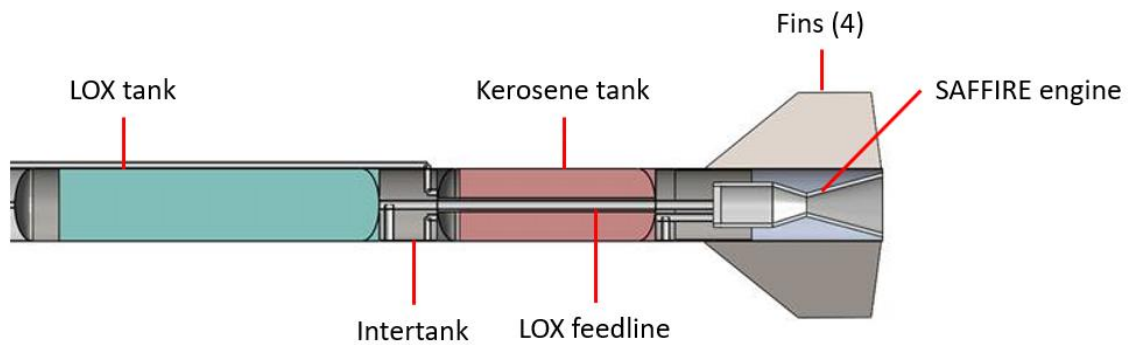


Figure 4-2: STEVE booster section details

The propellant tanks were designed to meet the propellant requirements of the SAFFIRE engine, whose performance parameters are detailed in Table 4-1.

Table 4-1: SAFFIRE engine parameters

Parameter	Unit	Value
Diameter	mm	292
Chamber pressure	bar	35
Total thrust (sea level)	N	27 610
Burn time	sec	30
LOX flow rate	kg/s	7.0
Kerosene flow rate	kg/s	2.9

Based on the above propellant flow rates, the LOX and kerosene feedline diameters were determined by a separate study to be 38 mm and 25 mm. Adding the pressure losses across the injector and the respective propellant lines (determined in a separate ASReG study) to the SAFFIRE engine’s design point chamber pressure of 35 bar, a propellant tank design pressure of 43.75 bar was determined for both tanks. The vent and pressurant ports are further prescribed to be 12.5 mm in diameter. The separate ports for venting and pressurisation were both considered. However, vent and pressurant ports at the top of each tank could be combined to minimise vehicle mass.

The propellant tank dimensions for STEVE presented in Table 4-2 are determined according to the engine performance parameters. The volume of the tanks was obtained based on the engine burn time of 30 s and oxidiser to fuel ratio of 2.9. Given the same tank diameter for both tanks and varying propellant densities, the oxidiser tank length is 1.79 times the length of the kerosene tank.

Table 4-2: Propellant tank design specifications

Parameter	Unit	Value
LOX tank volume	m ³	0.2054
Kerosene tank volume	m ³	0.1153
Tank diameter	mm	386
Ellipsoidal height	mm	96.5
LOX tank cylindrical length	mm	1720
Kerosene tank cylindrical length	mm	960
LOX tank total length	mm	1910
Kerosene tank total length	mm	1150

4.3. 301L SS Mechanical Properties

According to the propellant tank design guidelines in Chapter 2.6., the thickness of a tank is computed based on its working pressure. Internal pressure usually presents the worst-case loading for propellant tanks not part of the vehicle fuselage. In the final tank design, the preliminary thickness was evaluated against flight loads to determine the safe tank's thickness.

Half-hard 301L SS has been selected for use to fabricate the tanks due to its high elastic modulus to density ratio. The material's mechanical properties are illustrated in Table 4-3. The material certificate showing the chemical composition and mechanical testing results associated with the material used for tank fabrication is presented in Figure A-2, appendix I. The local suppliers and manufacturers of stainless steel only had the ½ hard 301L SS in stock. Hence, the preliminary tank design was performed according to this material.

Table 4-3: 301L SS mechanical properties

Mechanical property	Unit	Value
Density	kg/m ³	8 000
Modulus of elasticity (E)	GPa	193
Poisson's ratio (ν)	-	0.29
Yield strength	MPa	760
Tensile strength	MPa	1035

The maximum permissible stress on the tank is computed for both yield and ultimate strengths of the material; the lower value is then chosen for the design. The input variables for tank design for the formulas in Chapter 2.6.1 are shown in Table 4-4. The tank working pressure is computed as the sum of the chamber pressure at the design point and the pressure losses across the propellant feedline and injector. The weld strength is assumed to be 85 % of the parent material's strength. The weld efficiency of the austenitic steel typically lies between 85 and 95 percent (Huzel & Huang, 1967). The ellipse ratio is computed based on the geometry of the tank end as per equation 2-15.

Table 4-4: Tank design input variables

Variable	Unit	Value
Tank working pressure	bar	43.75
Weld efficiency (e_w)	%	85
Ellipse ratio (E')	-	5.52
Buckling coefficient (C_b)	-	0.100
SF_{yield}	-	1.100
$SF_{tensile}$	-	1.350

4.4. Propellant Tank Analytical Design

The minimum allowable wall thickness for each tank geometric region of the tanks was calculated using the material data and design input variables. The resulting thicknesses are presented in Table 4-5. The sample analytical calculations are included in appendix II. The standard commercially available sheet thickness closest to but exceeding the highest of these values is 1.5 mm. This thickness results in an actual safety factor of 1.15. The real safety factor could be increased, or the required wall thickness reduced, by using 301L SS, which is work-hardened to a higher degree, such as ½ hard, ¾ hard or full hard. A 1.5 mm thick, ½ hard 301L SS sheet was only available at Macsteel VRN, Johannesburg branch.

Table 4-5: Tank theoretical thickness

Parameter	Thickness (mm)
Cylindrical tank section (t_c)	1.438
Knuckle (t_k)	1.438
Crown (t_{cr})	1.438
Ellipsoidal tank end (t_e)	1.222
Available	1.500

The CAD geometry of the kerosene tank is illustrated in Figure 4-3. The tank consists of the LOX feedline tunnel tube, pressurant, vent, feedline, and dump ports. The LOX feedline goes through the tunnel tube with an air gap between the two to mitigate the excessive chilling and subsequent gelling of the kerosene contained in the tank. A tank skirt, composed of struts (6) and a flange made of 304 stainless steel, features at either end of the tank and connects the tank to vehicle hardware directly above and below it. The tank ports, made from 316 stainless steel, will be procured as off-the-shelf process fittings, and then welded to the tank.

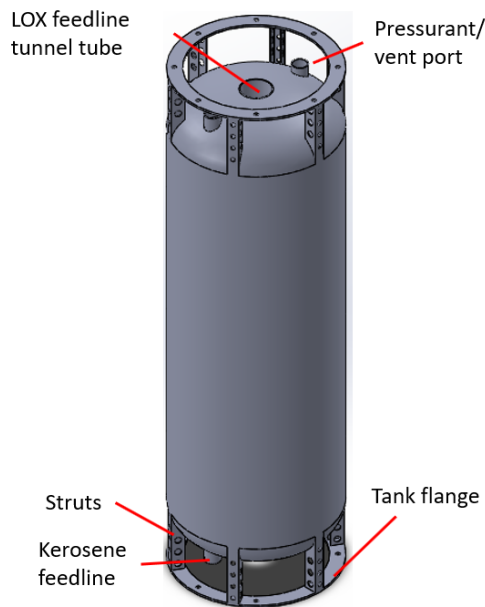


Figure 4-3: Kerosene tank

4.5. Summary

The preliminary propellant tank design phase entailed determining the tank's wall thickness based on the internal pressure loading only as per the NASA propellant tank design guidelines. A nominal tank wall thickness of 1.5 mm was found acceptable when a weld efficiency of 85 % was assumed. This preliminary thickness provided sufficient motivation for procuring a 1.5 mm thick 301L SS sheet for the study.

The volume of the propellant tanks was determined to meet the SAFFIRE engine design parameters, such as propellant mass rates and chamber pressure. The existing mandrel constrained the diameter of the tanks and geometry of the tank ends for the metal spinning process.

5. Material Testing

5.1. Introduction

In order to inspire confidence in the design results, the tank design input information must be accurate. A key parameter of concern is the weld efficiency that can practically be achieved for the design. For maximum design fidelity, weld efficiency should be determined experimentally based on the actual welding procedure employed. Beyond the welding procedure, other factors that affect the weld joint efficiency of pressure vessels are the welded joint type (butt or lap) and the wall thickness.

Two experimental exercises had to be undertaken to develop a final set of tank designs based on the preliminary design work described in Chapter 4: 1) an effective welding procedure needed to be determined, and 2) the associated weld efficiency needed to be quantified. These exercises are now discussed.

5.2. Welding of 301 SS

Chemical composition and physical properties influence the welding procedure of a metal. 301 SS has a thermal conductivity of half of the mild steels; as a result, heat is not dissipated from the weld zone quickly. This type of steel is also susceptible to distortion due to its comparatively high coefficient of expansion (Nickel Development Institute, 1991).

The proposed method for welding the propellant tanks is Tungsten Inert Gas (TIG) welding. The Lincon Electric Company provided guidelines for welding stainless steel based on sheet thickness and chemical composition. The document recommended welding parameters presented in Table 5-1 for joining a 1.5 mm thick 301 SS sheet using the TIG welding technique. The voltage control or heat input also affects the filler material deposition rate (Kotecki & Armao, 2003). 308L filler rod is recommended for welding 301 SS as it has ferrite, which prevents hot cracking.

Table 5-1: TIG welding parameters (*Kotecki & Armao, 2003*)

Current DC (-)	Electrode Diameter (in), mm	Gas Flow, Arg. (cfh), L/min	Filler-Rod Diameter (in), mm	Arc Speed (ipm), mm/sec
80 - 100	(1/16) 1.6	(10) 4.7	(1/16) 1.6	(12) 5.1

5.2.1. Welding by Fabricon

The welding of the tensile test samples was conducted on a 1.5 mm thick ½ hard 301L stainless steel sheet. This work was initially conducted by Fabricon, a company based in the south of Durban. It specialises in fabricating composite and steel pipes and pressure vessels in the petrochemical industry. Due to the welder experience, the heat input was reduced to 80 amperes (DC) with a power supply by dropping volt-ampere characteristic.

The welder could not adhere to the arc speed parameter, given that welding was manual and challenging to regulate. Instead, the welding current was selected to ensure sufficient weld penetration determined by inspection. Torch heat input (current) determines the required arc speed. The arc speed must be higher for higher heat input to avoid significant distortion and warpage.

The first weld trial was conducted as a single pass, i.e., the skip weld technique was not employed. Severe distortion in the sheets manifested as a result, as shown in Figure 5-1.

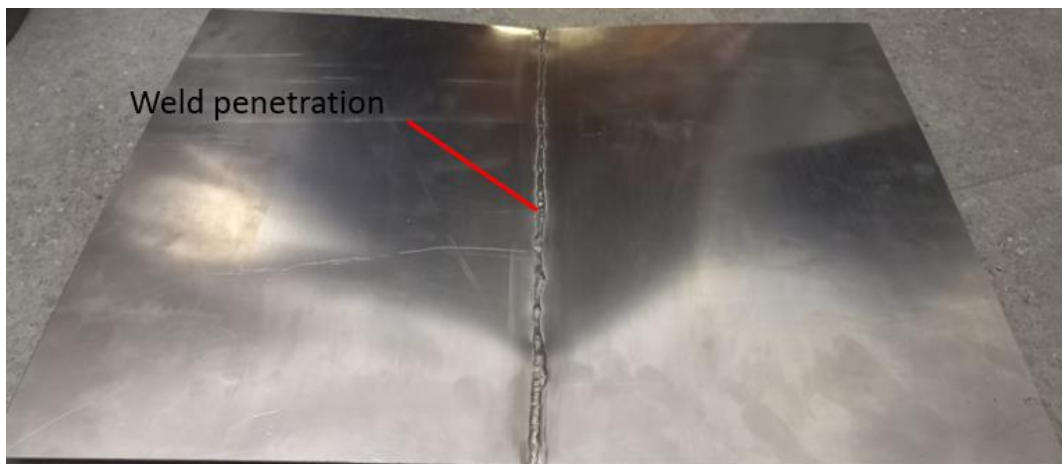


Figure 5-1: First weld trial by Fabricon

Emphasis was placed on measures to minimise distortion in the subsequent welding trial; these include the following (Kotecki & Armao, 2003) (Allen, 2021):

- The use of rigid jigs and fixtures restraining the sheets/parts being welded. Allowing the weld to cool in the fixture reduces distortion.
- Copper chill bars positioned near the weld zone aid in removing heat and preventing expansion-induced distortion. The arc must be kept away from the copper.
- Additional backup chill bars are always required for butt welding thin materials to mitigate distortion.

- Filler metal should not be deposited excessively as it rarely improves the weld's strength while it increases heat input and distortion.

In addition to the measures mentioned above, the skip welding technique was implemented in the manner shown in Figure 5-2. This method enables even heat distribution along the part. Each weld segment ranges between 40 and 50 mm.



Figure 5-2: Skip welding technique implemented

The use of copper bars and skip welding technique in the second welding trial reduced distortion and warpage significantly. The high thermal conductivity of copper helps dissipate heat faster away from the stainless steel. This further minimises the risk of hot cracking of the weld and sensitisation, hence improving the weld strength.

5.2.2. Welding by ND Engineering

ND Engineering is a company which specialises in manufacturing pressure vessels and boilers made from stainless steel. The company sponsored the manufacturing of the propellant test tank. Hence, the welding parameters were revised. The heat input was reduced to 38 – 40 Amperes (DC). This required the welder to weld at low speed to ensure the full penetration of the weld.

Welding using low heat input completely eliminated warpage and distorting the 301L SS sheet. Hence, the skip weld technique was not employed at these welding parameters. The welding conducted by ND Engineering is illustrated in Figure 5-3.



Figure 5-3: Welding by ND Engineering

5.3. Tensile Testing Procedure

A tensile test is a method used specifically for determining yield strength, tensile strength, yield point elongation, elongation, and area reduction of metallic materials. Tensile testing of welded (9) and unwelded (3) samples having a geometry illustrated in Figure 5-4 was conducted. The ASTM standard, E8/EM8 (ASTM Standard, 2013), specifies the dimensions of the sheet type test sample; these include the gauge length (G), width (W), length of the grip section and overall length (B) to be 50 mm, 12.5 mm, 50 mm and 200 mm, respectively.

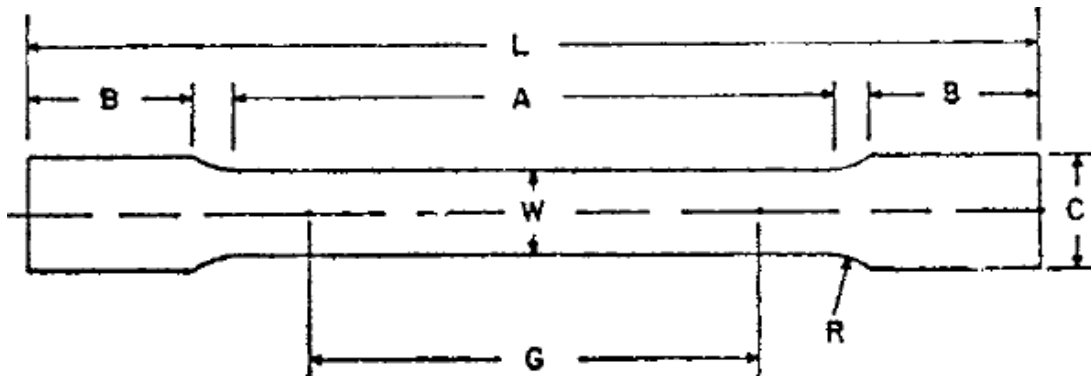


Figure 5-4: Sheet type test sample (ASTM Standard, 2013)

Standard E8/EM8 further outlines the parameters for conducting the tensile test. These include the speed of testing, which can be interpreted as the strain rate applied to the specimen, the crosshead speed, as well as the elapsed time for completing part or all of the test. For the tensile testing conducted in this study, specimen strain rate (mm/mm/min) was adopted to define the speed at which the specimen is deformed. This requires feedback from an

extensometer, which allows the testing machine to be operated in closed-loop control (ASTM Standard, 2013).

The apparatus required for conducting a tensile test is the Instron tensile testing machine, load cell (100 kN), and testing software (Instron), as illustrated in Figure 5-5. The Instron software acquires the test data and generates a stress vs strain curve for the tested sample. The tensile testing machine used for this test is computer-based; hence the load and strain ranges are automatically selected. The tensile testing machine can be observed in Figure 5-8 and Figure 5-9. Each specimen tested was given a unique identification in the form of a serial number, description (welded or unwelded), and test date. The strain rate used for the test was 0.015 mm/mm/min as per the E8/EM8 ASTM standard.

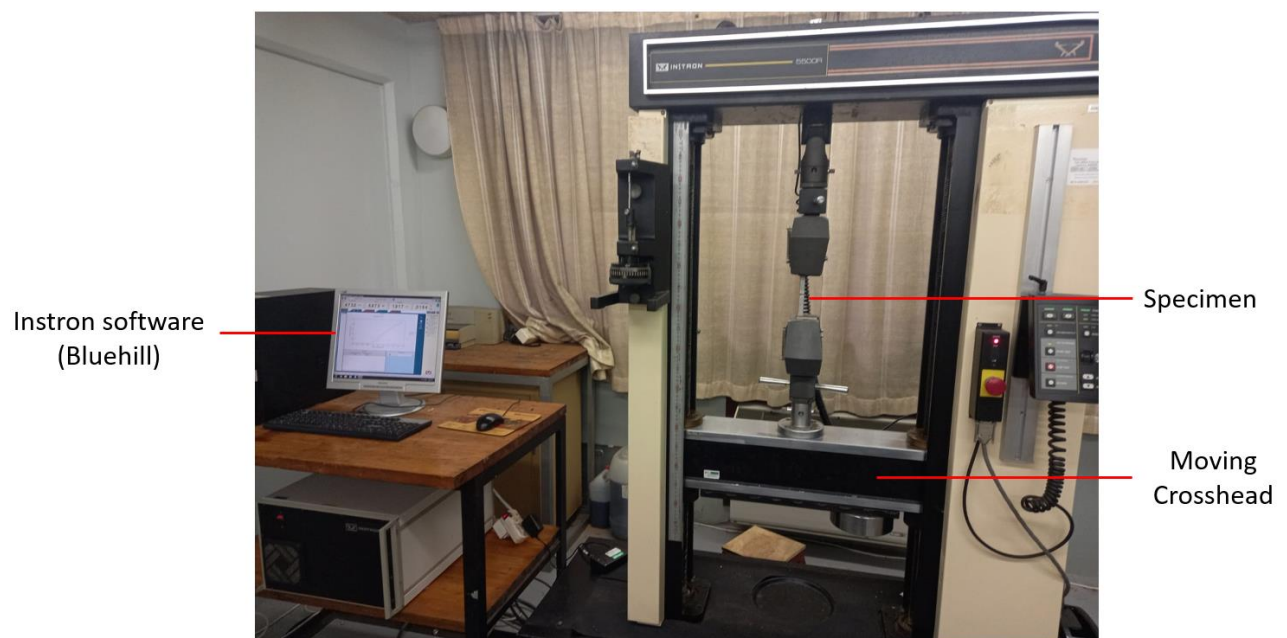


Figure 5-5: Instron tensile testing machine

Several possible issues, such as specimen misalignment and worn grips, must be considered during the test setup. Otherwise, off-centre loading may impose bending loads on the specimen. Careful attention must be given to the extensometers as they measure strain during tensile testing. Following the installation and zeroing of the extensometer, subsequent installations of the specimens should require no zero modification.

The welded and unwelded samples are shown in Figure 5-6. They were produced from two welded sheets of ½ hard 301L SS which were then cut out using laser and water-jet cutting for unwelded and welded tensile test specimens, respectively. Cutting using these

technologies does not overheat the samples, given that the cutting action is precise and rapid. Hence, the risk of annealing and alteration of the mechanical properties of the steel is averted.

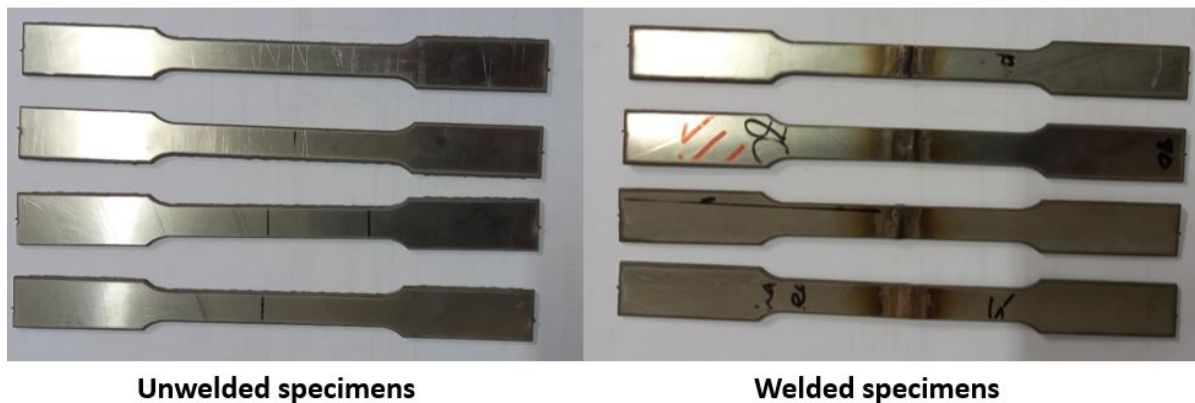


Figure 5-6: Tensile test samples

The welded tensile specimens are shown in Figure 5-7. The heat-affected zone is visible on these specimens between the weld region and the unwelded region. It appears in burnt or brownish colour, indicating depletion of the material's corrosion resistance property.



Figure 5-7: Welded tensile test sample

5.4. Tensile Test Results

To determine the weld strength and, by inference, weld efficiency, tensile tests were conducted on unwelded (6) and welded (9) specimens. The ASTM standard recommends a minimum of three samples when conducting the tensile test. The decision to have more welded specimens was to ensure that all the critical regions of the welds were captured. The region where the skip welds meet is considered critical as there is a risk of pinholes occurring.

The yield and tensile strength of the unwelded specimens correlate to the supplier's material certificate data, which can be accessed in Appendix I. The average yield and tensile strengths are 762 MPa and 1020 MPa, respectively, as illustrated in Table 5-2. The maximum tensile

strain is 25 %, as shown in Figure 5-8. This maximum extension of 16 mm correlates to the theoretical value for ½ hard 301 stainless steel (ASTM, 2003) (Stal, 2018).

Table 5-2: Tensile test results for unwelded 301L specimens

Sample No	Yield Strength (MPa)	Tensile Strength (MPa)	The extension (mm)
1	749	993	16.017
2	778	1036	16.299
3	760	1030	16.040
Average	762	1020	16.119

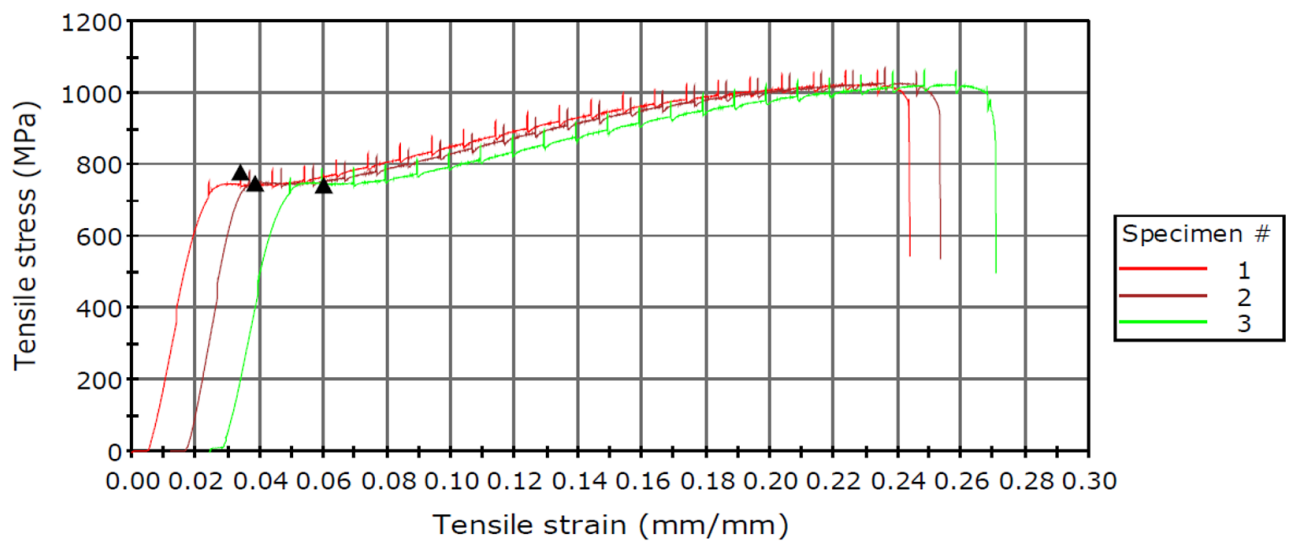


Figure 5-8: Unwelded specimen tensile test results

5.4.1. High Heat Input Welding Parameters

The high heat input welding parameters are associated with the 80 A (DC) current performed by Fabricon. The average yield and tensile strength for the welded specimens were found to be 528 MPa and 901 MPa, respectively, as presented in Table 5-3. The welded specimens were bent due to distortion during welding; hence the initial portion of each stress vs strain curve is horizontal as the sample straightens out, as shown in Figure 5-9.

Table 5-3: Tensile test results for welded 301L specimens – high heat input

Sample No	Yield Strength (MPa)	Weld efficiency against yield (%)	Tensile Strength (MPa)	Weld efficiency against Tensile (%)	Max. Extension (mm)
1	550	72	798	78	6.221
2	525	69	828	81	8.210
3	500	66	752	74	6.220
4	562	74	873	86	12.178
Average	534	70	813	81	8.207

There is about a 40 % to 50% reduction in tensile strain in the welded specimen. This is due to the discontinuity of the mechanical properties in the weld and heat-affected zone. Specimens 1 and 3 were taken at the intersection of the two skip welds, hence the lowest tensile strength and maximum tensile strain on these specimens as shown in Figure 5-9. This observation may be because the intersection point of the skip welds is heated twice, further reducing ductility and strength. The tensile test results in Table 5-3 show that the weld strength against yield and ultimate tensile strength of the parent metal is approximately 70 % and 81 %, respectively.

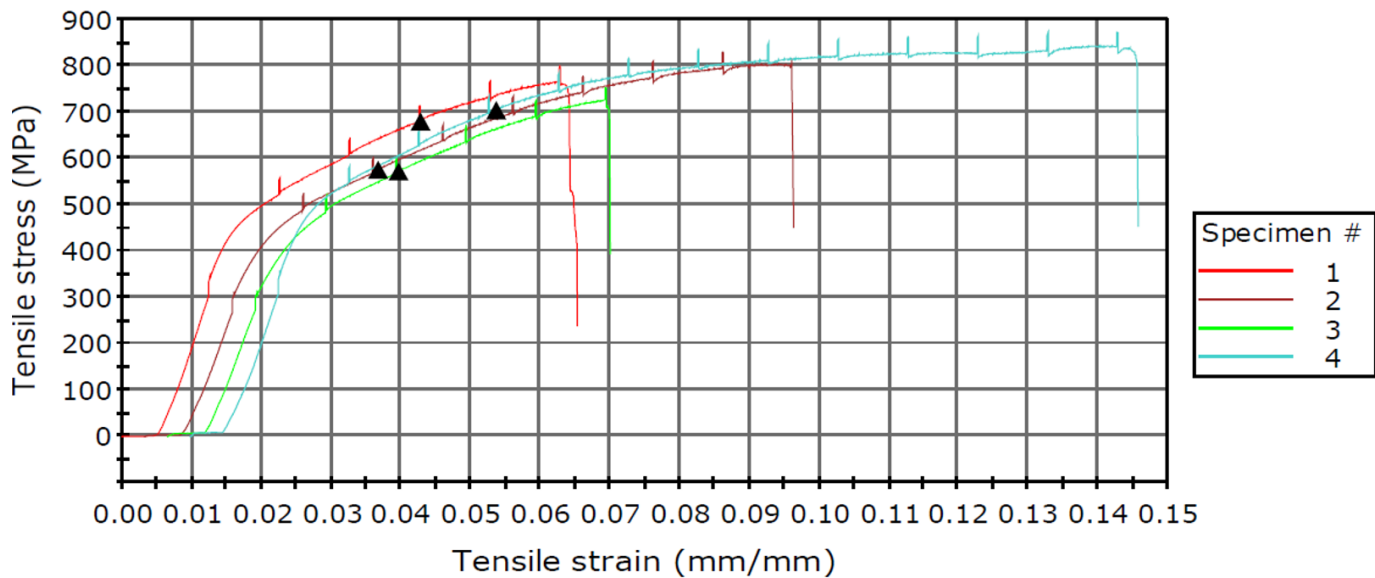


Figure 5-9: Welded specimen tensile test results – high heat input

All welded specimens failed in the heat-affected zone, experiencing a brittle fracture, implying that welding significantly reduced material ductility. From Figure 5-10, it can be observed that the reduction of the cross-sectional area was evenly distributed along the gauge length of the unwelded specimen. The specimen eventually failed along the shear plane (at an angle) of

the material's crystal structure. In contrast, the welded specimen failed along the horizontal plane in the heat-affected zone signifying a brittle fracture. There is minimal plastic deformation before fracture and occurs in some regions along the gauge length of the specimen.

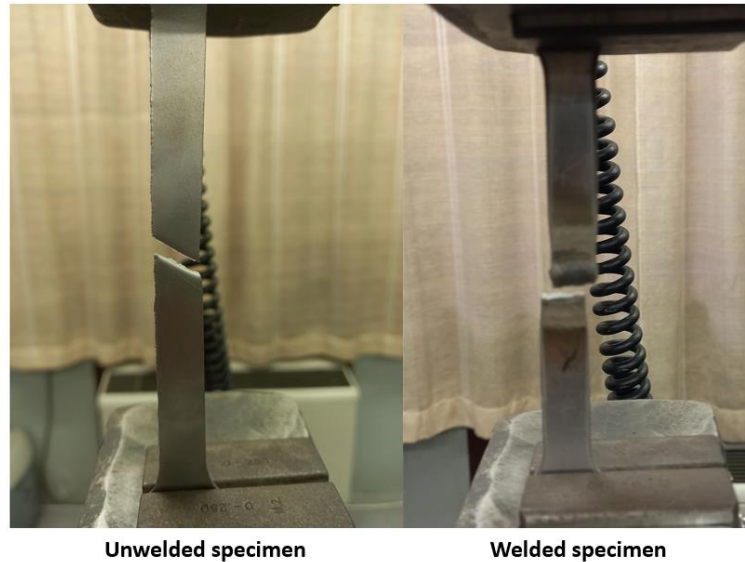


Figure 5-10: Failure of the specimens

5.4.2. Low Heat Input Welding Parameters

The low heat input welding parameters are associated with the 38 – 40 A (DC) current performed by ND Engineering. These welding parameters resulted in a weaker weld, although distortion and warpage of the welded 301L sheets were averted. The welded samples had an average maximum extension of 9.055 mm, as presented in Table 5-4. The mechanical properties of the specimens welded using low heat input parameters are within the same range as there are no outliers. This can be observed on the stress vs strain graph in Figure 5-11.

Table 5-4: Tensile test results for welded 301L specimens – low heat input

Sample No	Yield Strength (MPa)	Weld efficiency against yield (%)	Tensile Strength (MPa)	Weld efficiency against Tensile (%)	Max. Extension (mm)
1	420	55	762	75	8.441
2	405	53	802	79	9.438
3	410	54	770	75	9.448
4	400	52	760	75	8.467
5	400	52	792	78	9.479
Average	407	53	777	76	9.055

The tensile test results in Table 5-4 show that the weld strength against yield and ultimate tensile strength of the parent metal is approximately 53 % and 76 %, respectively. The specimens welded by low heat input parameters also failed in the heat-affected zone. The low strength of the welds produced through these parameters had the least weld penetration, which attributes to the weak welds. This results in a weld with a relatively small cross-sectional area.

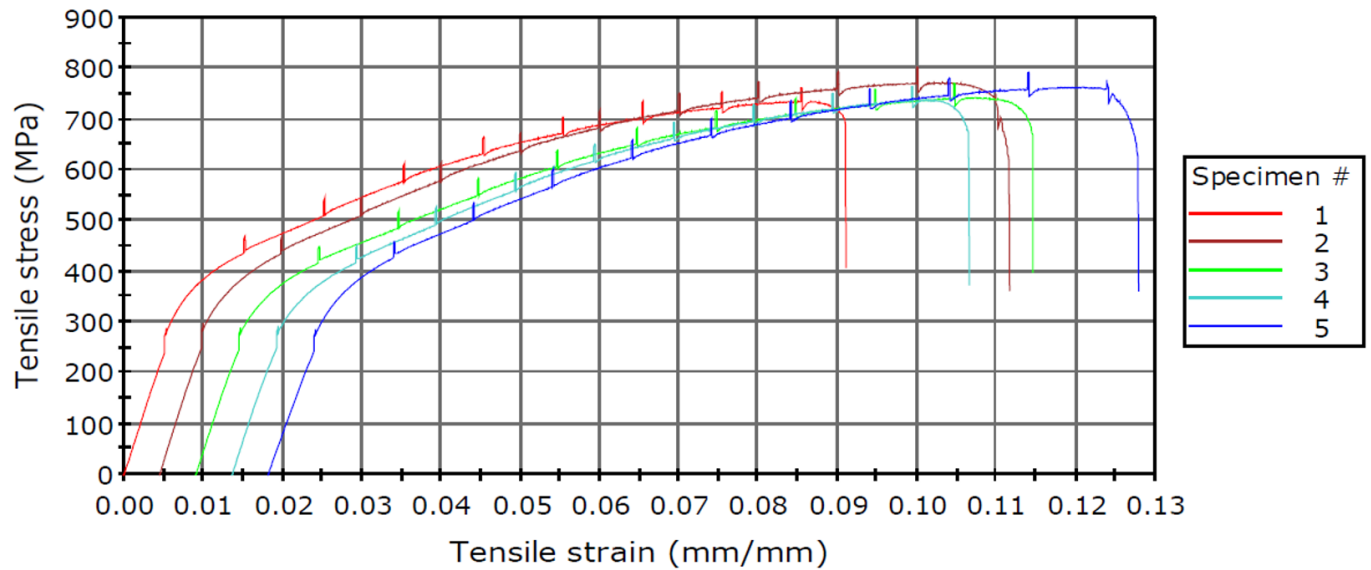


Figure 5-11: Welded specimen tensile test results – low heat input

5.5. Summary

Adequate heat dissipation proved to be the greatest challenge for welding the ½ hard 301L stainless steel. As a result, distortion and warping were visible in the sheets welded using high heat input parameters. More emphasis was placed on jiggling the sheets properly and reducing heat input to mitigate these phenomena. Using copper bars to dissipate heat rapidly and employing the skip weld method to minimise heat input reduced the significance of warpage and distortion. The tank's longitudinal weld would be more likely to experience warpage due to the relatively small thickness of the sheet welded. As a result, jiggling when performing this weld would be more crucial than when performing circumferential welds.

Warping and distortion result in localised stresses in the heat-affected zone. It must be highlighted that all the welded test specimens failed in this zone. This may be attributed to many other factors, including localised stresses and work-hardening properties reduced by heat input. Annealing or hammering may be employed to relieve these stresses. None of the fore-mentioned was used for this work as annealing would weaken the whole welded piece, not only the heat-affected zone.

A complication of hammering is that its effects cannot be accounted for analytically in the tank design. Also, the uniformity of this process cannot be monitored accurately throughout the weld and heat-affected zones. It is important to note that radiography was not used to detect internal defects in the welds, such as excessive porosity and defective fusion. This was due to the time constraints and unavailability of companies locally that could perform radiography when the samples were tested.

The tensile test results show the strength of the welded specimens by high heat input (80 A) to be approximately 70 % of the strength of the parent material in terms of yield strength and 81 % in terms of ultimate tensile strength. The low heat input resulted in welds strength of 53 % and 76 % against yield and tensile strength, respectively.

6. Final Propellant Tank Designs

6.1. Introduction

Following preliminary propellant tank design and material testing, the weld efficiency for 301L stainless steel was established, allowing the final propellant tank designs to be developed. These designs were developed to ensure the tanks operate safely when subjected to internal pressure and flight loads. Adequate resistance to buckling failure would also need to be established.

Table 6-1 shows the various wall thicknesses computed analytically, assuming weld efficiencies ranging from 70 to 85 percent. These thicknesses are computed considering only the internal pressure and the safety factor of 1.1 against the yield strength. The weld efficiencies below 70 % were not considered as they would result in heavier propellant tanks. The results show that a 2 mm sheet of ½ hard 301L stainless steel would suit the propellant tank design. The weld efficiency does not affect the elliptical tank end thickness as there is no weld joint in it. The different regions of the elliptical tank end are shown in Figure 2-15.

Table 6-1: Theoretical tank wall thickness based on assumed weld efficiency

Tank Region	Wall Thickness (mm)			
	70 %	75 %	80 %	85 %
Cylindrical tank section (t_c)	1.746	1.629	1.528	1.438
Knuckle (t_k)	1.746	1.629	1.528	1.438
Crown (t_{cr})	1.746	1.629	1.528	1.438
Ellipsoidal tank end (t_e)	1.222	1.222	1.222	1.222
Available sheet thickness	2.00	2.00	2.00	1.500

6.2. Propellant Tank CAD

The configuration of the final propellant tanks design includes the tank structure (cylindrical section and tank ends), tank skirts, and the intertank structure between the tanks, as shown in Figure 6-1. Figure 6-2 shows the separate tank's integral components aforementioned, including the anti-slosh and anti-vortex baffles. The anti-slosh baffles' width to tank radius ratio (w/R) was taken to be 0.1 based on the experimental data presented in Table 2-2 (Stephens & Scholl, 1967) (Pérez, et al., 2012). This results in a width, thickness and placement interval of 40 mm, 2 mm, and 386 mm, respectively. The ant-slosh baffle assembly must be welded together before being tack welded into the tank.

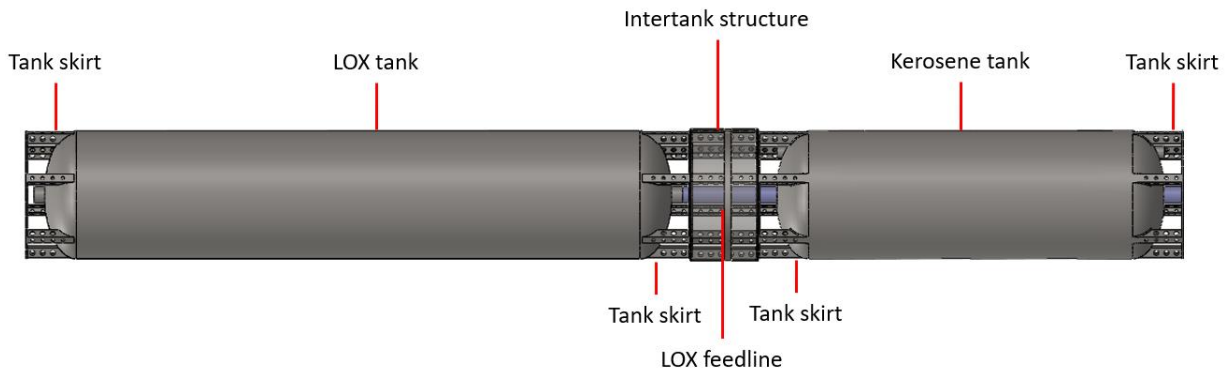


Figure 6-1: Propellant tank integration

The tank skirt and intertank structure consist of six struts equi-spaced circumferentially and a mating flange (two, in the case of the intertank structure). The number of struts was determined through an iterative finite element analysis process. Further description of the tank skirt is provided in Chapter 7 of this report. The tank port fittings and plumbing lines are to be made from 316L SS and chosen based on the working pressure of 43.75 bar. Weld fittings for the tank ports were adopted due to their ease of integration with feedlines and the tank structure.

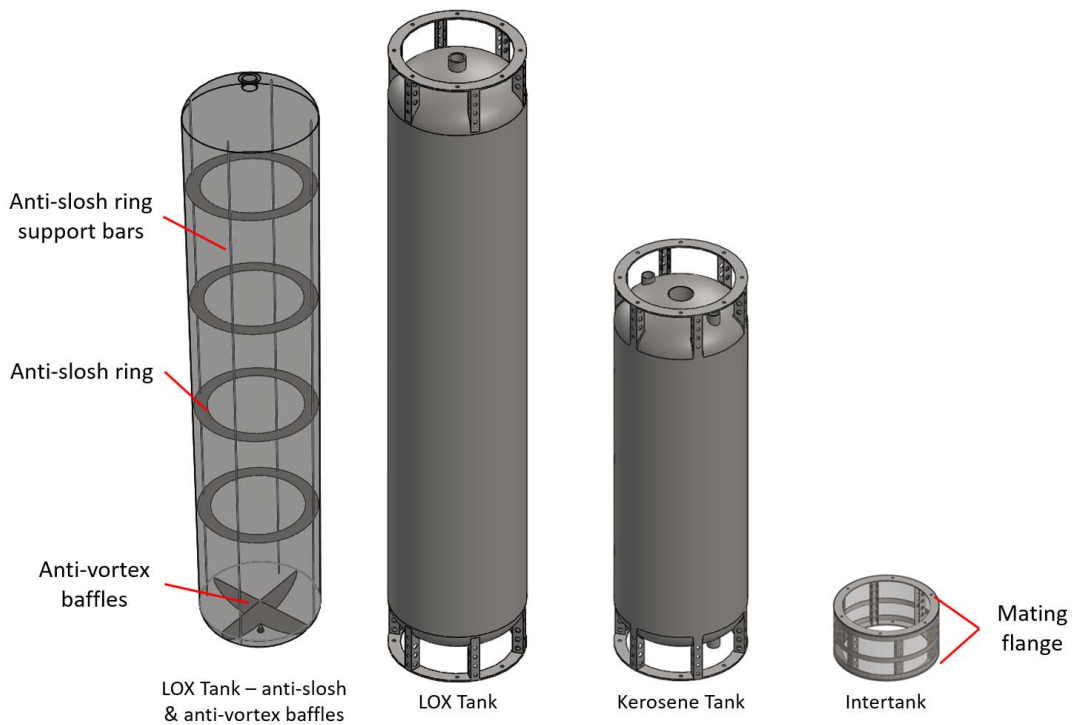


Figure 6-2: STEVE propellant tanks

Since the configuration of the top (LOX) propellant tank feedline running internally of the kerosene tank was adopted, this required a tunnel tube in the kerosene tank to house the LOX

feedline. This LOX feedline configuration eliminates the risks of the propellant evaporating and aerodynamic heating that may occur if the feedline runs externally of the kerosene tank.

The tunnel tube runs concentrically through the kerosene tank, is made from 304 SS and has a diameter of 73 mm (3 inches) illustrated in Figure 6-3. The air gap between the outer surface of the LOX feedline, which is 38 mm in diameter, and the inner surface of the tunnel tube is therefore 18 mm and was determined in a separate study by ASReG to be sufficient to prevent gelling of kerosene during the period of operation. The 301L, 304 and 316L stainless steels are inter-weldable since they are all austenitic stainless steels.

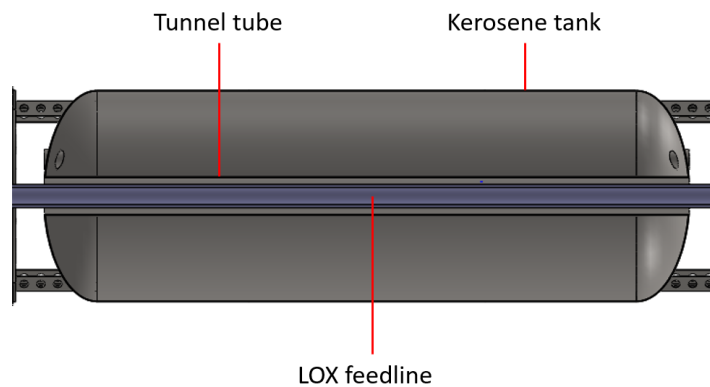


Figure 6-3: Kerosene tank cross-section

6.3. Propellant Tank Flight Loading

The NASA propellant tanks design guidelines recommend that the tank's wall thickness be determined analytically by only considering the internal pressure loading. This wall thickness is then evaluated against the vehicle's flight loads. The evaluation of the tanks against flight loads was conducted using the ANSYS software program. This part of the study aimed to determine the number of struts and the thickness of the flange of the tank skirts. The flight loads considered were the inertial, aerodynamic drag and bending loads, as shown in Figure 6-4. The vehicle's thrust, aerodynamic drag, and weight all act axially along the vehicle's axis.

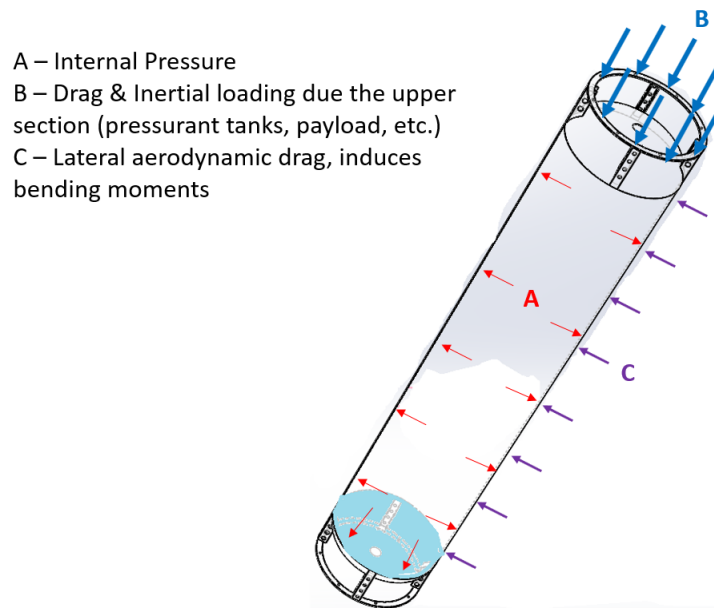


Figure 6-4: Loads experienced by the LOX tank

6.3.1. Vehicle Inertial and Aerodynamic Loads

Six degree-of-freedom flight simulations were performed using ASReG's Hybrid Rocket Performance Simulator (HYROPS) and provided vehicle performance parameters that enabled the above loads to be determined (Chowdhury, 2012). Although the HYROPS software was initially developed for hybrid-sounding rockets, its features also allow for liquid engine rockets to be simulated. The thrust curve data is one of the user input files, and the propellants' depletion rate can be modelled in the software. The time-based vehicle performance parameters obtained were the magnitude of acceleration, velocity magnitude, altitude, dynamic pressure and angle of attack during the flight.

The maximum acceleration and velocity are attained at engine burnout, 31.16 s into the flight, as shown in Figure 6-5 and Figure 6-6. At engine burnout, the dynamic pressure is also maximum.

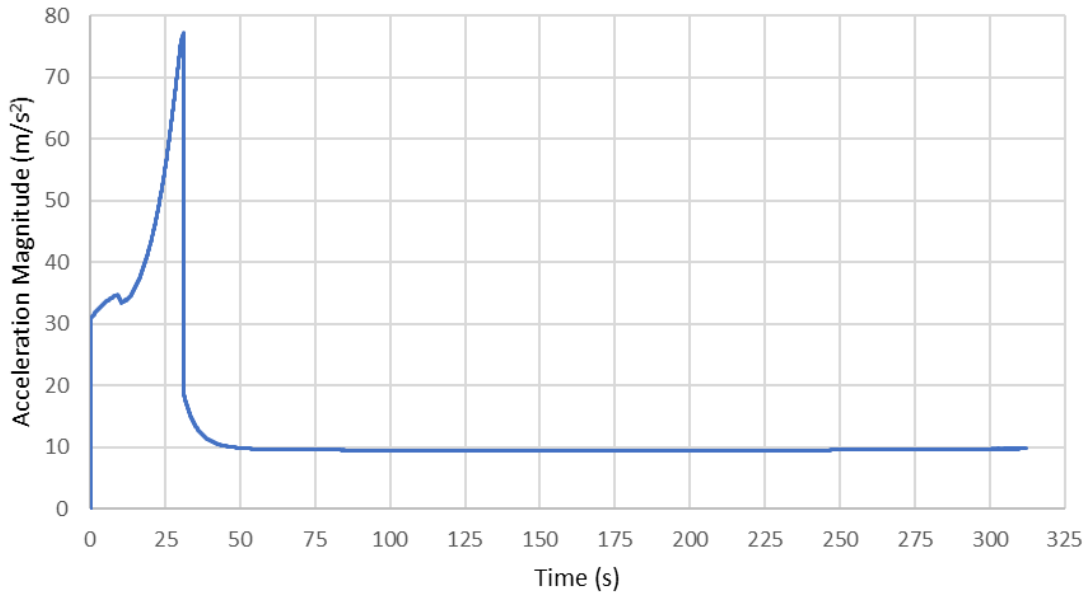


Figure 6-5: STEVE flight acceleration profile

Aerodynamic drag load is proportional to dynamic pressure, a function of the vehicle's velocity. The combination of the thrust, aerodynamic drag and vehicle's weight gives the resulting inertial load (Newlands, et al., 2016).

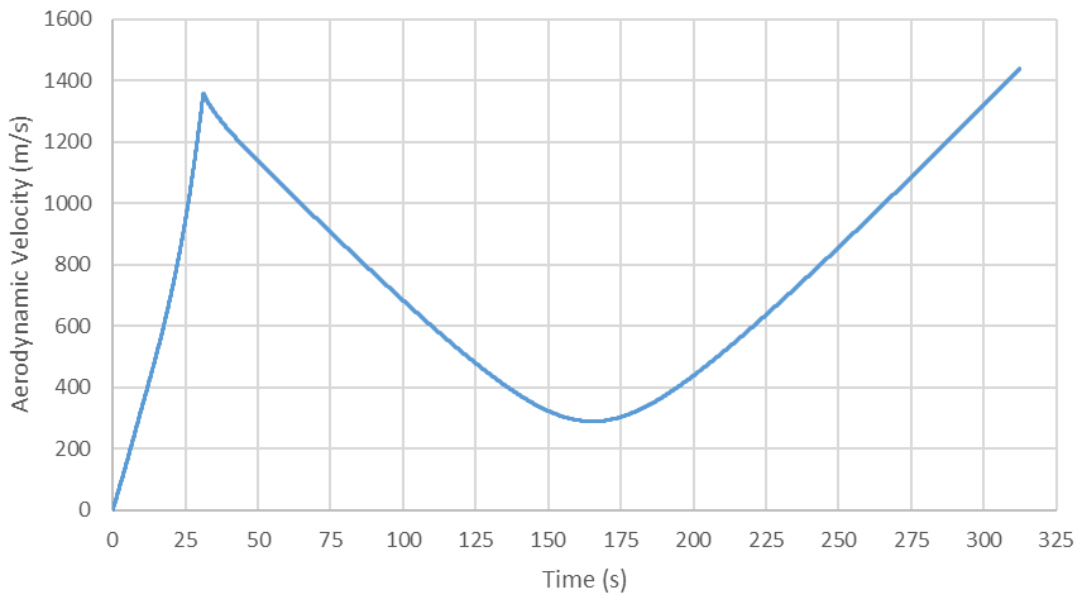


Figure 6-6: STEVE flight velocity profile

The kerosene tank experiences worse inertial loading than the LOX tank. The inertial load on the kerosene tank reaches a maximum of 11 958 N within 4 s of the flight, depicted in Figure 6-7. This figure also demonstrates how the mass above the kerosene tank changes during

flight. The mass variation above the kerosene tank is due to the LOX consumed until the engine burns out at 31 s. The maximum inertial load on the LOX tank is 9 289 N.

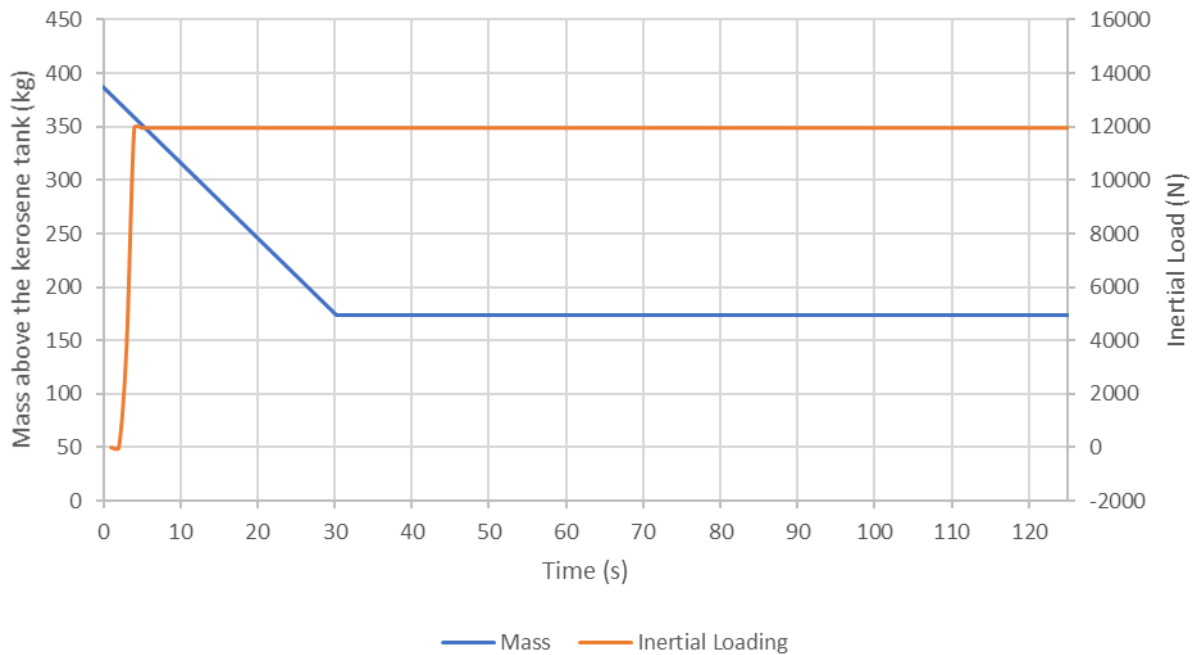


Figure 6-7: Inertial load on the kerosene tank

6.3.2. Vehicle Bending Load

The vehicle is also subjected to bending loads during the flight, which are induced when the vehicle flies at a non-zero angle of attack, which in turn causes lift forces on the vehicle. The lift forces acting on the nose cone, body and fins cause lateral acceleration of the vehicle; hence the vehicle is subjected to bending, which can also be considered a shear load. In order to determine the shear loads at various sections of the rocket's body, the vehicle is treated as a freely-supported beam subjected to lift forces and consequent bending moments (Newlands, et al., 2016). Figure 6-8 illustrates the vehicle's beam model and the location of the lift forces.

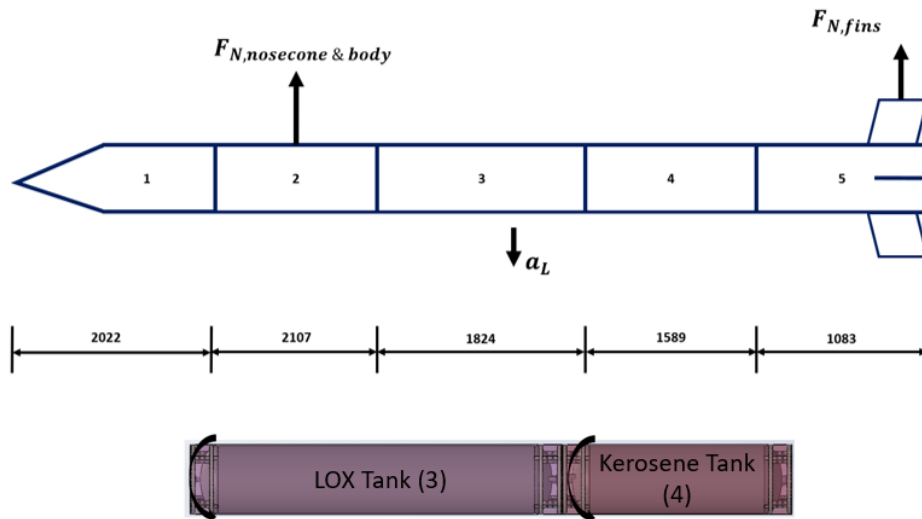


Figure 6-8: STEVE lift forces diagram

The numbered sections of the vehicle are described in Table 6-2. The lift coefficient obtained was for the combination of the nose cone and the rocket's body; hence Figure 6-8 depicts a combined lift force for the rocket's body and nose cone.

Table 6-2: Description of the vehicle's numbered sections

Object Number	Description
1	Nose cone, payload
2	Pressurant, roll control
3	LOX tank
4	Kerosene tank
5	Engine bay, injector, casing

The angle of attack induces the shear load or bending moment on the rocket. The flight performance output shows that motor burnout occurs at 31 s when the air density is 0.06 kg/m³, which is about 95 % of the air density at sea level, as illustrated in Figure 6-9.

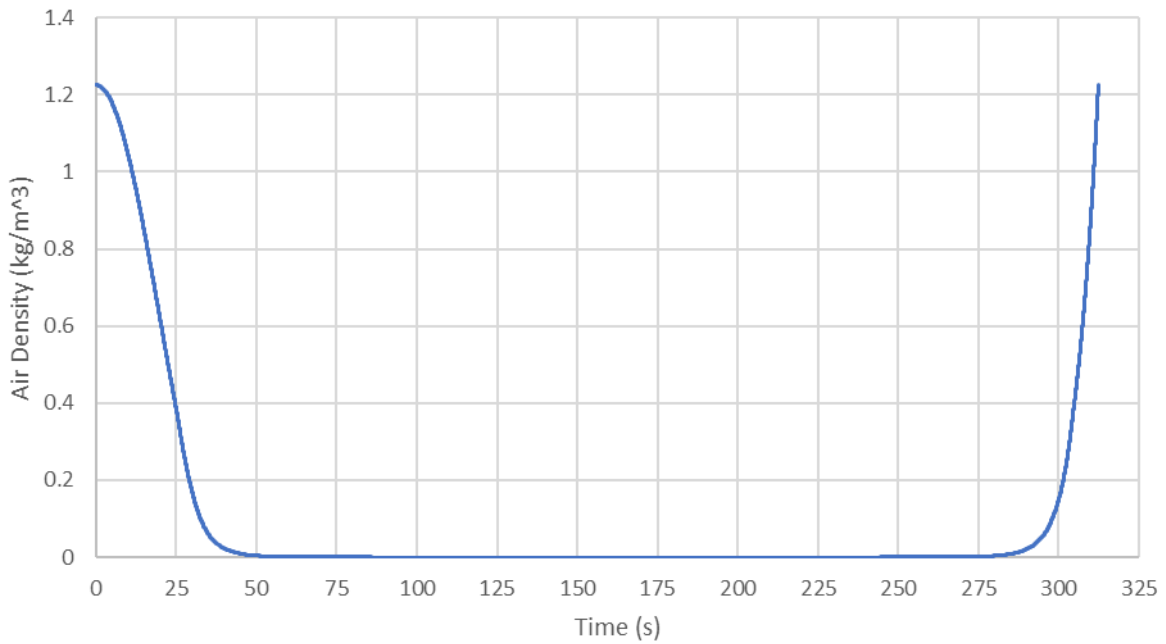


Figure 6-9: Air density vs time profile

As the rocket ascends through the atmosphere, the ambient air density decreases. At the same time, during the boost phase, the velocity increases. Dynamic pressure is directly proportional to the velocity squared and proportional to ambient density. In the period from engine ignition to burnout, the dynamic pressure quickly climbs to a maximum as the velocity increases. Thereafter, however, it rapidly falls back to zero despite continued acceleration as the ambient air density decreases. This dynamic pressure profile during the flight is shown in Figure 6-10.

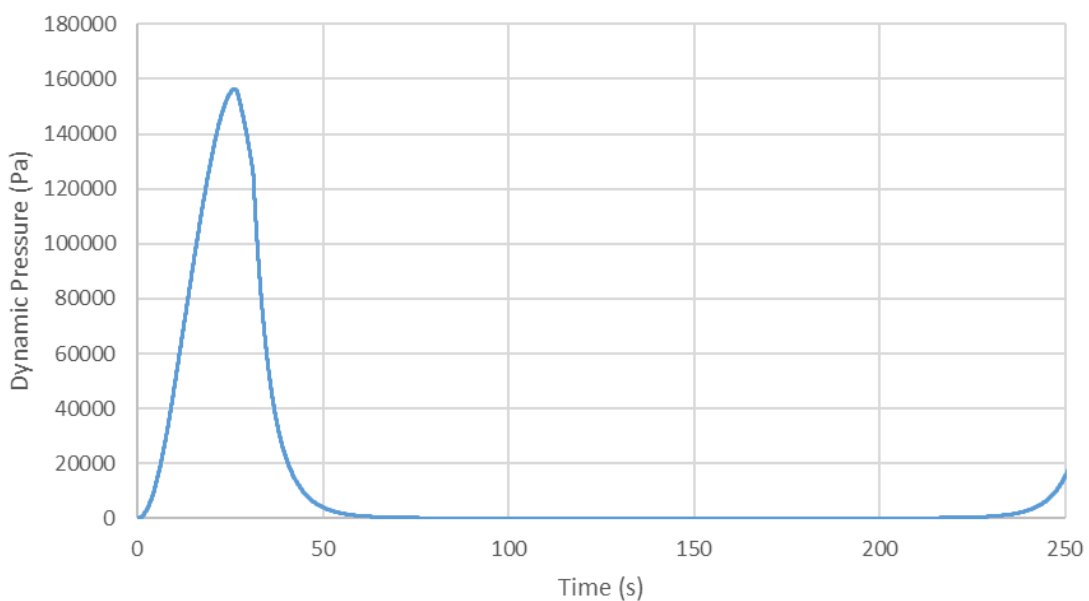


Figure 6-10: Dynamic pressure vs time profile

When there is no dynamic pressure, no aerodynamic forces are acting on the rocket, meaning the fins do not work to reduce the angle of attack. As such, while coasting at a high enough altitude, the rocket's orientation will effectively remain constant, independent of trajectory. This manifests as a sustained and considerable increase in the angle of attack beyond a flight time of approximately 50 s, as depicted in Figure 6-11. The angle of attack during the boosting phase is approximately zero degrees, meaning the lift or normal forces on the vehicle are negligible. The coasting phase begins at 31 s into the flight, whereas the descent phase commences at 164 s.

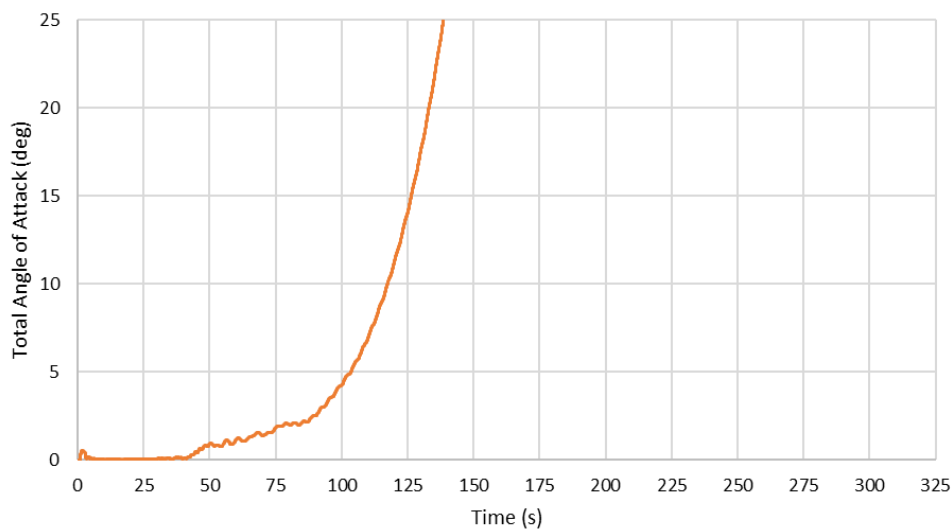


Figure 6-11: STEVE angle of attack profile

Figure 6-12 further illustrates that the rocket's body normal force is negligible during the boosting phase. The centre of pressure is measured from the nose cone tip. The theory behind the COP and associated data for this work is presented in appendix II, section B.2.

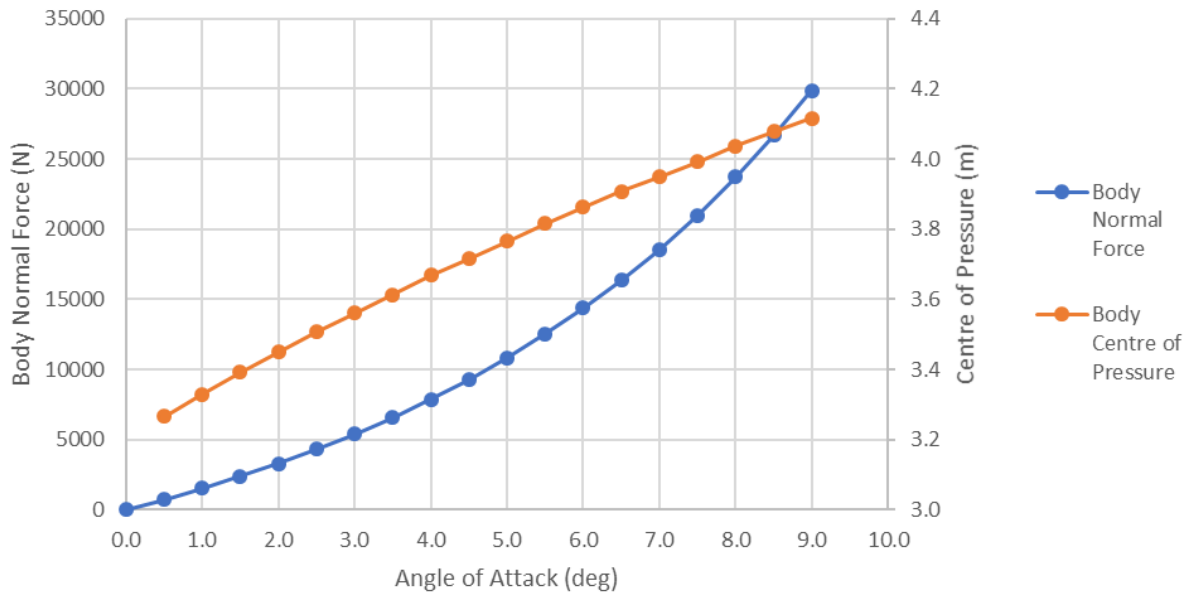


Figure 6-12: Nose cone and rocket's body normal force

For design purposes, a worst-case scenario of a shear wind, meaning a sudden occurrence of the jet stream during the flight, was included in the simulation. The jet stream was assumed to occur at an altitude of 10 km. This results in the angle of attack oscillating between 0 and 2°, as shown in Figure 6-13.

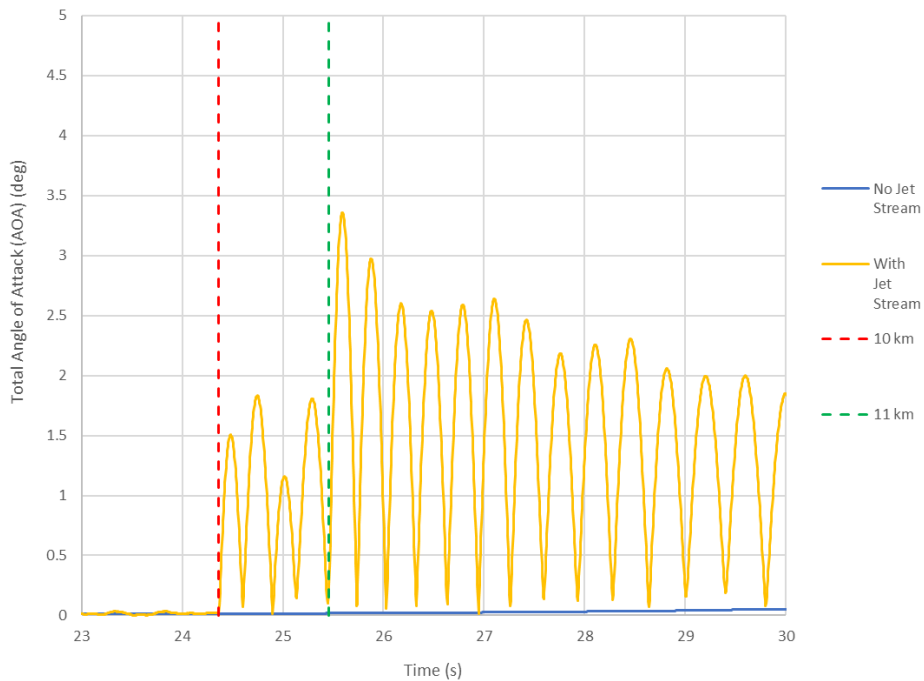


Figure 6-13: STEVE angle of attack profile at induced jet stream

The angle of attack of 2 ° results in the rocket's body and fins lift or normal force of 3 302 N and 8 141 N, respectively. The Fins normal force versus the angle of attack is presented in Figure 6-14. The shear force diagram was computed analytically at the angle of attack of 2 °.

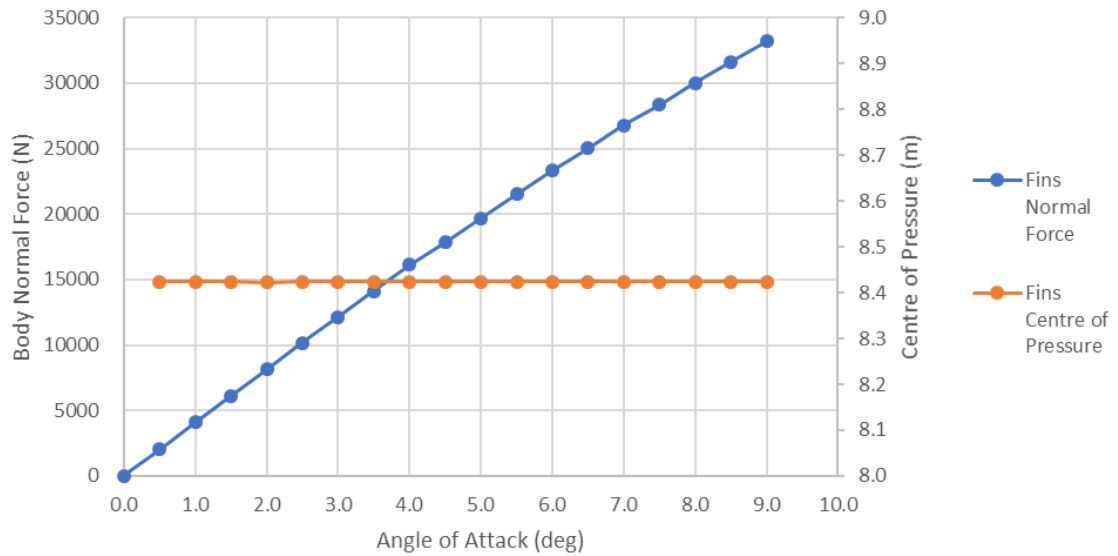


Figure 6-14: Fins normal force and the centre of pressure

The shear force and the bending moment are interchangeable. For simulation purposes, the shear forces were used to analyse the effect of lift forces on the tanks. The vehicle's shear force diagram generated using the normal forces and the vehicle's lateral acceleration is shown in Figure 6-15. The shape of the shear force diagram shows the uniform distributed load between the body and the fins normal force. The uniform distributed load (UDL) sections result from the same lateral acceleration and density within the rocket sections. The shear force on the LOX tank and the kerosene tank is 1 469 N and 3 224 N respectively, as shown by the red circles in Figure 6-15.

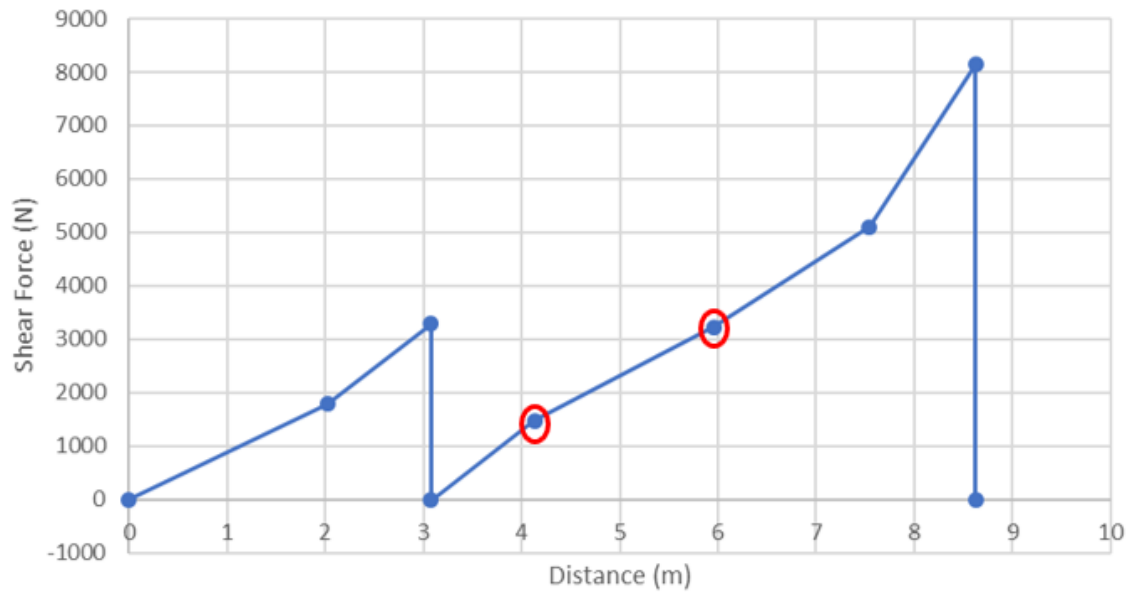


Figure 6-15: STEVE shear force diagram at 2 ° angle of attack

6.4. Finite Element Analysis Setup

The propellant tanks' FEA was conducted using the ANSYS Workbench software program (Sridharan, 2018). This software program allows 3D and 2D geometries to be imported from CAD software programs such as Solidworks, Inventor and Fusion 360. It further enables geometries to be modified in its Spaceclaim built-in extension. This simulation software program has the unique feature of integrating different physics (fluid and solid) into one platform (Sridharan, 2018).

The stages of simulating using static structural analysis include engineering data configuration, geometry importation, simulation model, simulation setup and running the solution, as shown in Figure 6-16. The engineering data enables the user to configure material properties such as the yield and tensile strength, Young's modulus of elasticity, Poisson's ratio and shear modulus. The mechanical properties of the 301L SS properties were configured as per the material certificate in Appendix I. The propellant tanks' geometries were generated using Solidworks and imported to ANSYS Workbench as STEP files.

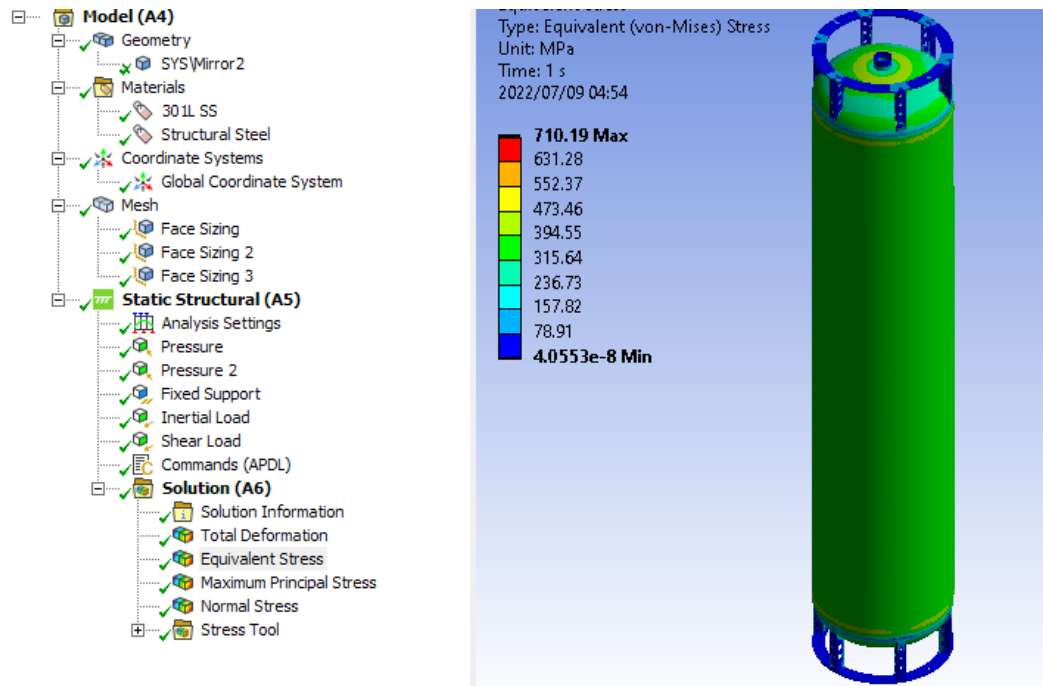


Figure 6-16: Simulation stages of ANSYS static structural analysis

The model feature entails material assignment to the geometry and generating the appropriate mesh. A program-controlled mesh was chosen as this option generates mesh elements based on the simulated geometry while ensuring the solution's accuracy and reducing the computational cost. Face sizing controls were adopted to refine the mesh on tank ends and skirts for improved accuracy. The mesh independence study presented in Figure 6-17 was conducted by iterating the global mesh from 75 mm to 5 mm and iterating the face mesh size between 2 mm and 5 mm. The summary of mesh independence parameters is presented in Table 6-3.

Table 6-3: LOX tank mesh independence study

Global Mesh	Mesh size (mm)		Number of Elements	Max Von Mises (MPa)
	Face Sizing 1	Face Sizing 2		
5	2	2	1053790	657.01
5	5	2	892996	651.97
10	5	2	723095	647.85
15	5	2	564564	651.81
30	5	2	447468	650.22
50	5	2	422375	579.32
60	5	2	418961	512.97
75	5	2	414364	513.88

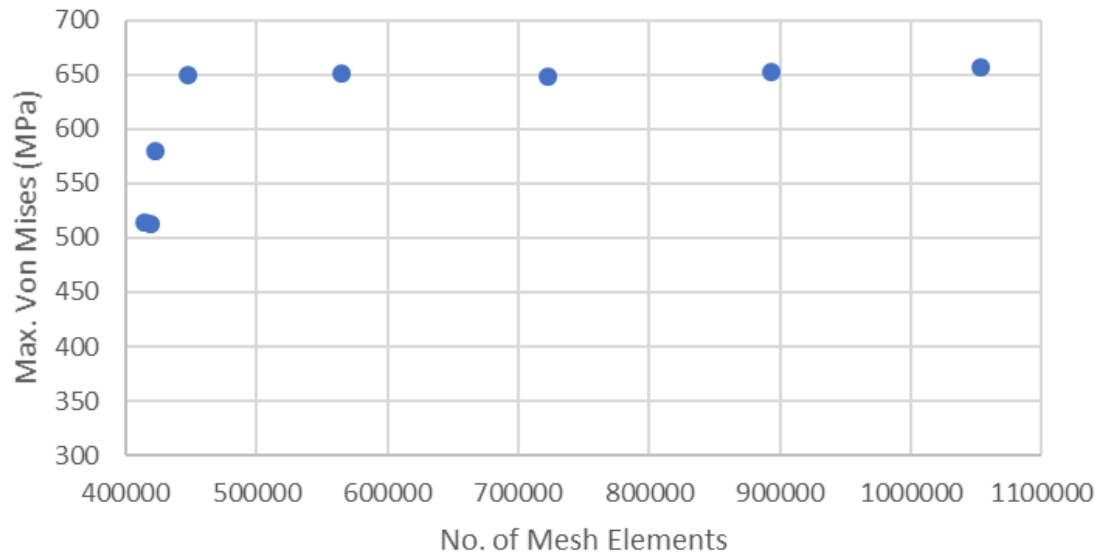


Figure 6-17: LOX tank mesh independence study

The adopted global and face mesh sizes were 5 mm and 2 mm, respectively. This resulted in the LOX tank simulation with 1 053 790 mesh elements and 2 113 674 nodes shown in Figure 6-18.

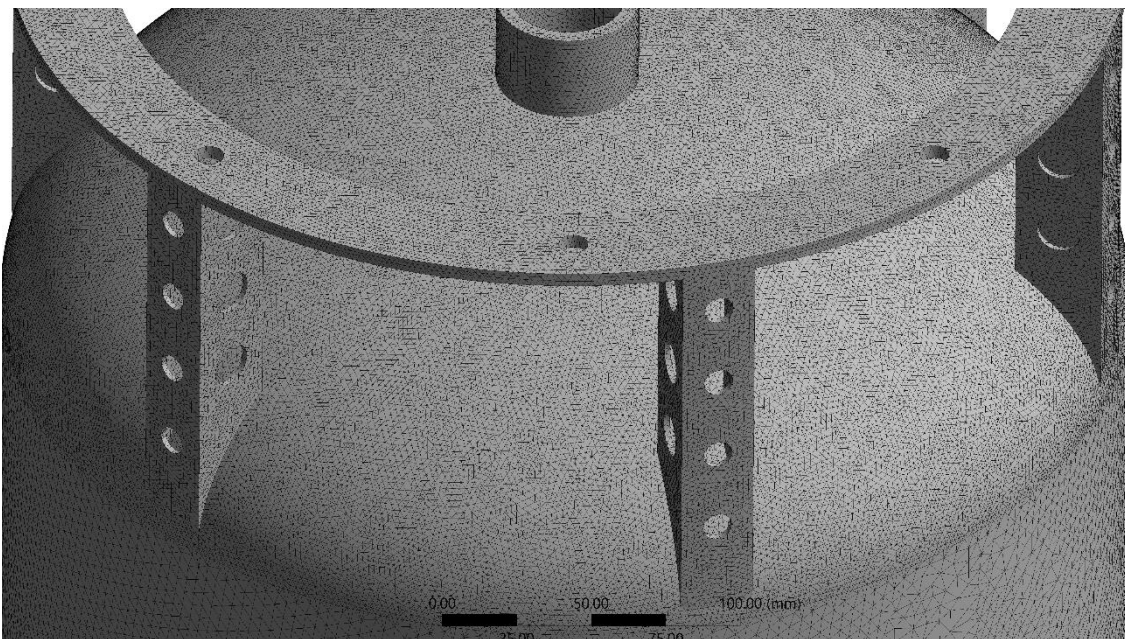


Figure 6-18: LOX tank mesh

The simulation setup entailed assigning load and boundary conditions according to Figure 6-19. The inertial load (F1) is applied on the tank skirt flange axially, with the shear load (F2) applied horizontally on one side of the flange holes. The internal pressure is applied perpendicular to the tank's inner faces. P2 is the pressure that simulates that the closure of

tank ports will result in pressure exerted on the top surface of the tank port mounts. This pressure is computed analytically using equation 6-1. Fixed support (S) was applied to the bottom tank skirt flange. This constrains the flange in three dimensions and represents the frictional contact between the tank and intertank structure.

$$P2 = \frac{P1 \times R_i^2}{R_o^2 - R_i^2} \quad 6-1$$

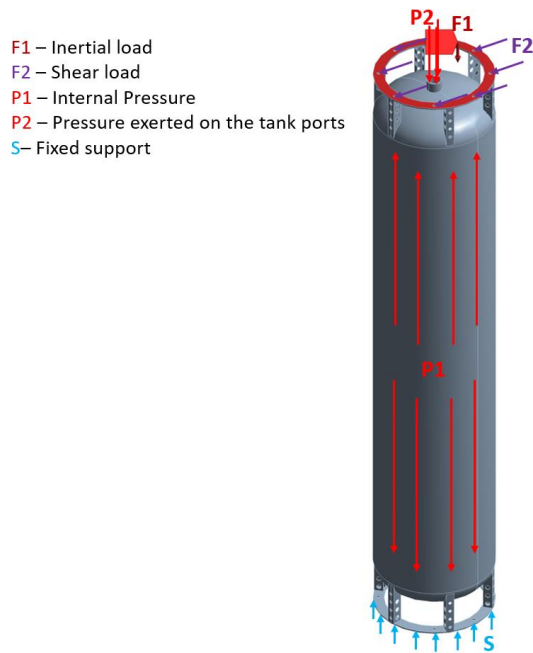


Figure 6-19: LOX tank simulation setup

These boundary conditions are valid for both propellant tanks, with only the inertial and shear load values varying accordingly. The summary of the flight loads simulated is presented in Table 6-4.

Table 6-4: Simulation loads for the propellant tanks

Load Type	LOX Tank	Kerosene Tank
Internal Pressure (P1), bar	43.75	43.75
Tank Port Pressure (P2), bar	73.5	153.2
Inertial Load, N	9 289	11 958
Shear Load, N	1 469	3 224

6.5. Finite Element Analysis Results

6.5.1. LOX Tank FEA Results

Finite element analysis was conducted on the LOX tank to evaluate its structural response to internal pressure and flight loading. The collection of internal pressure, inertial, and shear loading is referred to as combined loading. The maximum equivalent stress (Von-Mises) increases by 8 % due to combined loading, as shown in Figure 6-20. This increase in stress attributed to the flight loads is uniform in all the tank regions.

This maximum equivalent stress occurs at the stress concentration point where one strut intersects with the tank end. The mesh was not refined further since the maximum equivalent stress was below the material's yield strength. The maximum equivalent stress observed in the flange for the combined loading case is 111.38 MPa. Overall, the equivalent stress at all points within the LOX tank is below the weld and material yield strength.

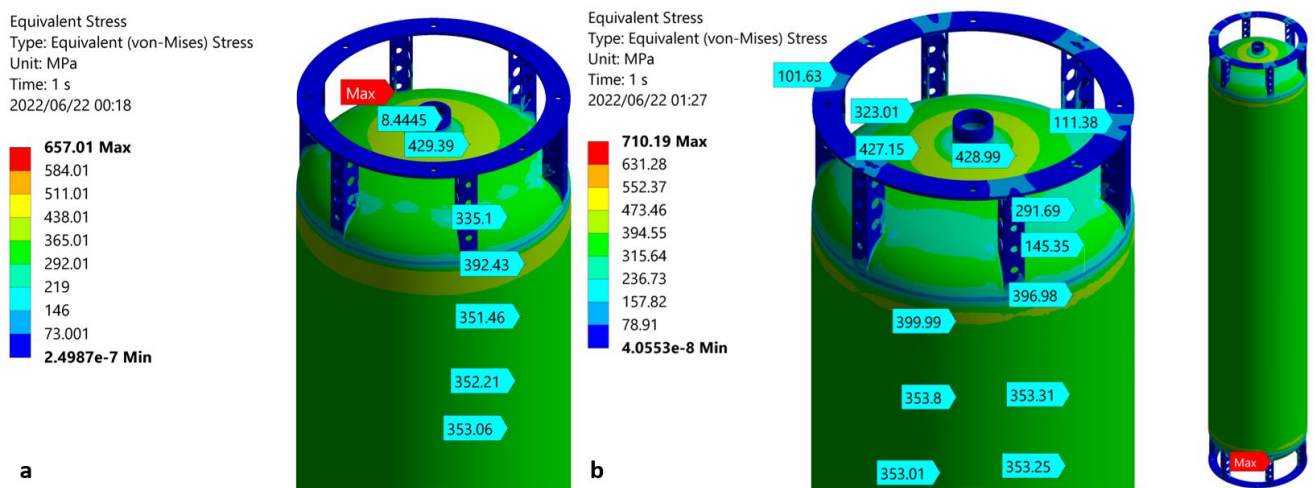
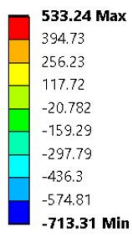


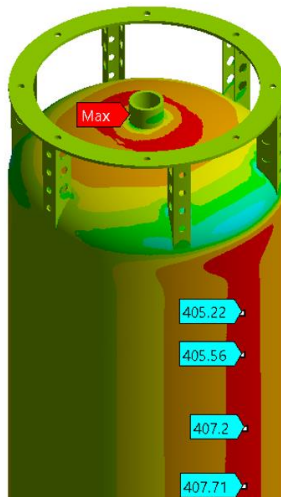
Figure 6-20: LOX tank equivalent stress due to the internal pressure loading (a) and combined loading (b)

The theoretical hoop stress for a 2 mm tank wall thickness is 422 MPa. In both the internal pressure loading (a) and combined loading (b) cases, the predicted hoop stress is below this theoretical value when sampled away from the tank ends, as illustrated in Figure 6-21. The hoop stress was 407 MPa, about 3 % less than the theoretical hoop stress result.

Normal Stress
 Type: Normal Stress(Z Axis)
 Unit: MPa
 Global Coordinate System
 Time: 1 s
 2022/06/22 00:17



a



Normal Stress
 Type: Normal Stress(Z Axis)
 Unit: MPa
 Global Coordinate System
 Time: 1 s
 2022/06/22 01:28



b

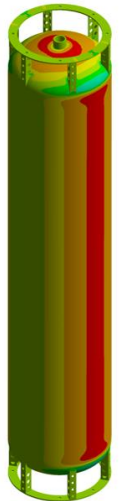
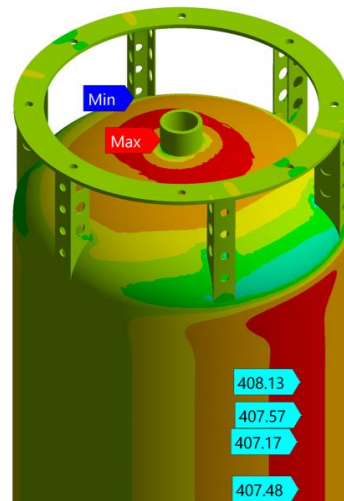
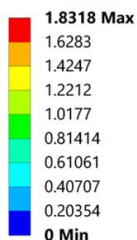


Figure 6-21: LOX tank hoop stress due to the internal pressure loading (a) and combined loading (b)

The maximum total deformation increases by 12 % for the combined loading case compared to the internal pressure loading case, as shown in Figure 6-22. The increase in total deformation is also visible in the flange due to the shear and inertial loading. The total deformation is the magnitude of deformations in all three directions. The maximum deformation occurs in the tank ends. The fixed constraint in the bottom flange causes the deformation to accumulate from the bottom flange to the tank's top section. This can be observed by zero deformation in the bottom tank end. In practice, both tank ends will deform evenly; hence the maximum will be almost halved.

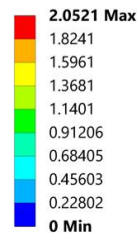
Total Deformation
 Type: Total Deformation
 Unit: mm
 Time: 1 s
 2022/06/22 00:19



a



Total Deformation
 Type: Total Deformation
 Unit: mm
 Time: 1 s
 2022/06/22 01:27



b

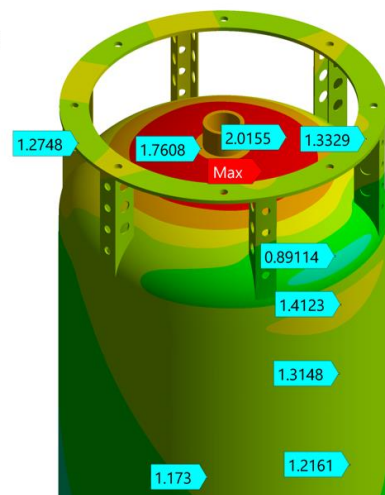


Figure 6-22: LOX tank total deformation due to the internal pressure loading (a) and combined loading (b)

Figure 6-23 shows the safety factor distribution determined based on the material yield strength and equivalent stress. Hence the safety factor distribution is similar to the equivalent stress of the tank illustrated in Figure 6-20. The minimum value of the safety factor occurs at stress concentration points. The weld efficiency of 70 % results in a safety factor of 1.5 in the tank's cylindrical section. It is still above the recommended safety factor for launch vehicles propellant tanks which is 1.100 (Huzel & Huang, 1967).

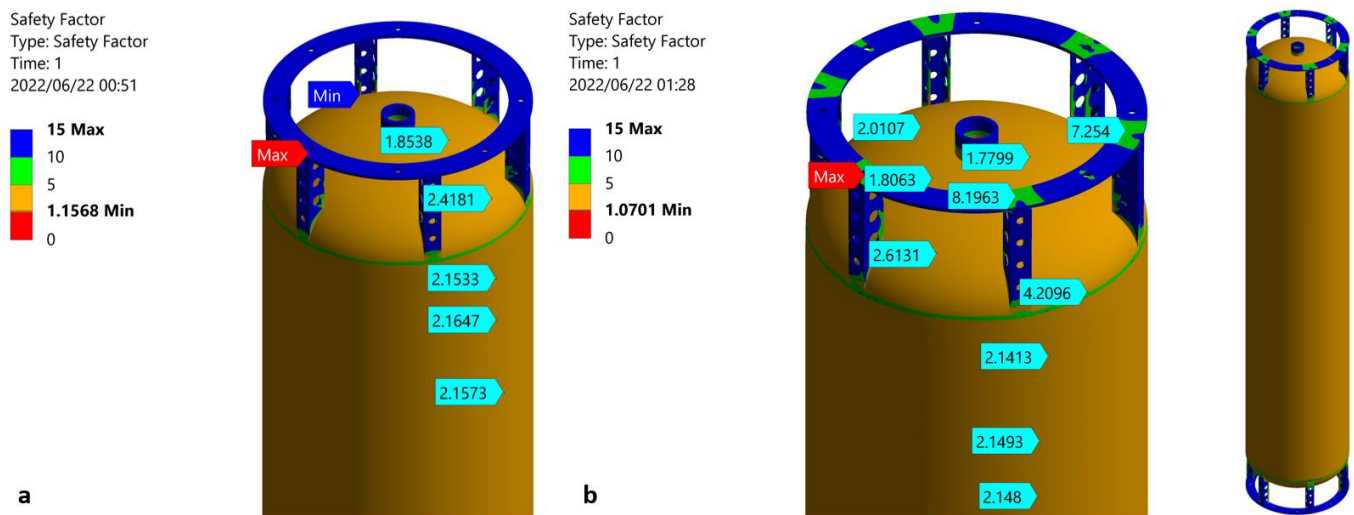


Figure 6-23: LOX tank safety factor against the internal pressure loading (a) and combined loading (b)

6.5.2. Kerosene Tank FEA

The mesh settings used for the LOX tank were still valid for the kerosene tank. These included the global and face mesh sizes set to 5 mm and 2 mm, respectively. The boundary conditions applied are the same as the LOX tank with a different magnitude of the flight loads. Recall that the kerosene tank consisted of separate tank ports (venting, pressurisation, filling/dumping, and feedline) to evaluate their effect on stress distribution.

The equivalent stress on the kerosene tank's cylindrical section shown in Figure 6-24 is about 120 MPa higher than that of the LOX tank. The maximum equivalent stress on the LOX and kerosene tank top flange is 111 MPa and 132 MPa, respectively, for the combined loading case. Hence, the substantial increase in the equivalent stress of the kerosene tank is attributed to the tunnel pipe, which restricts the tank from expanding freely.

The maximum equivalent stress on the kerosene tank of 824 MPa for the combined loading (b) case also occurs at the exact location (strut) as it does in the LOX tank. This results in a stress concentration factor of 1.25, which is less than 3, the maximum allowable stress

concentration factor for pressure vessels (Moss, 2004). This result is accepted as the maximum equivalent stress is below the material's tensile strength.

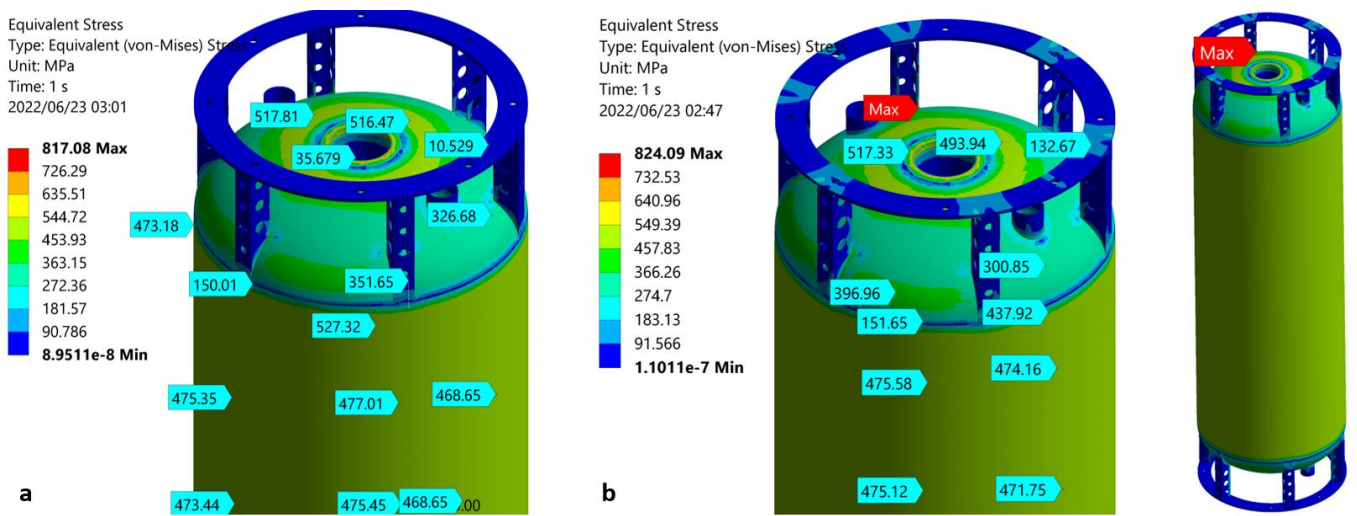


Figure 6-24: Kerosene tank equivalent stress due to the internal pressure loading (a) and combined loading (b)

The resulting hoop stress from two loading cases (a) and (b), shown in Figure 6-25, is higher than the theoretically predicted hoop stress since the tunnel pipe constrains the tank. The kerosene tank configuration does not subscribe to the pressure vessel theory since the derivation of pressure vessel theory formulas does not consider obstructions such as the tunnel pipe in this case. The hoop stress for the kerosene tank is about 136 MPa higher than that of the LOX tank.

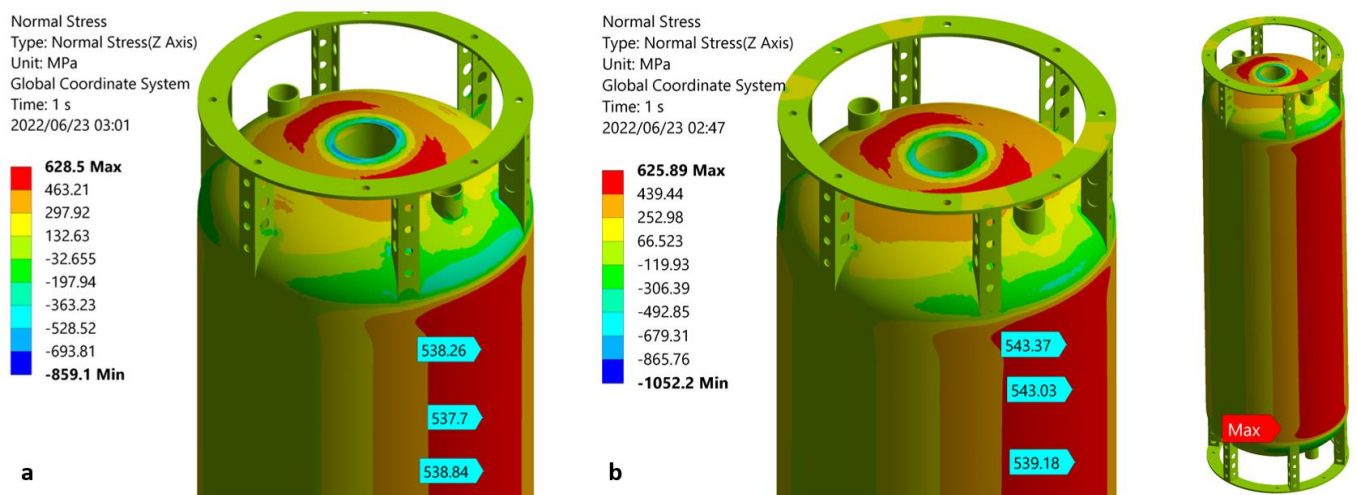


Figure 6-25: Kerosene tank hoop stress due to the internal pressure loading (a) and combined loading (b)

The maximum total deformation of the kerosene tank is about 7 % less than that of the LOX tank for the pressure loading case. Figure 6-26 shows the total deformation maximum in the tank ends region surrounding the tunnel pipe. This further shows that the tunnel pipe restricts the tank from deforming, as observed from both loading cases.

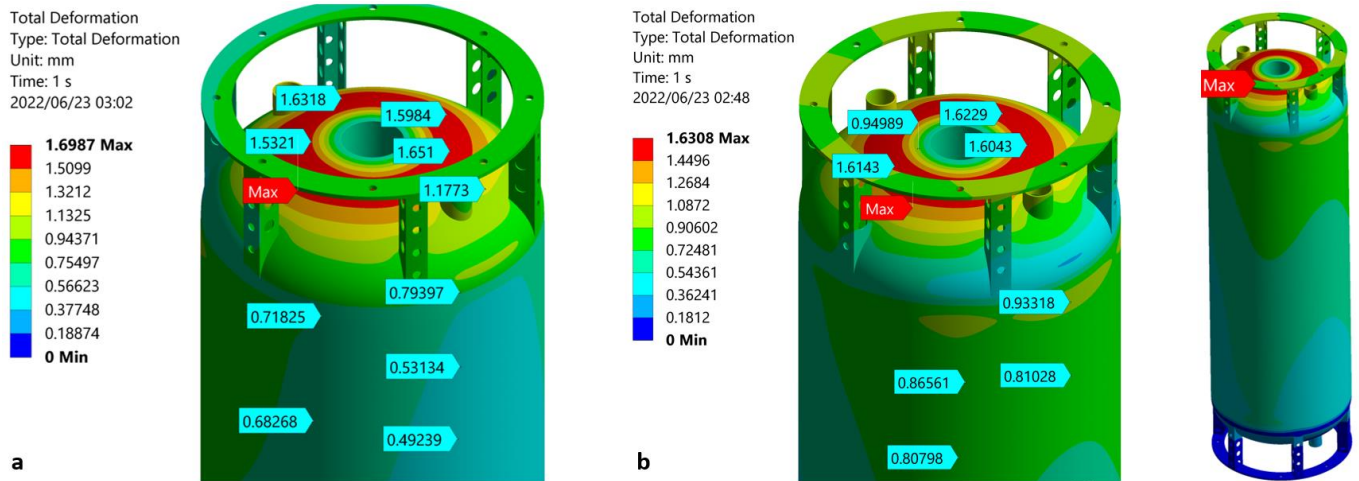


Figure 6-26: Kerosene tank total deformation due to the internal pressure loading (a) and combined loading (b)

The kerosene tank is severely loaded, apparent from the results of the tank's safety factors against internal pressure loading (a) and combined loading (b) cases, as depicted in Figure 6-27. This is shown by the safety factor of 1.60 in the kerosene tank's cylindrical section compared to the safety factor of 2.10 for the LOX tank. The weld efficiency of 70 % results in a safety factor of 1.12 in the tank's cylindrical section.

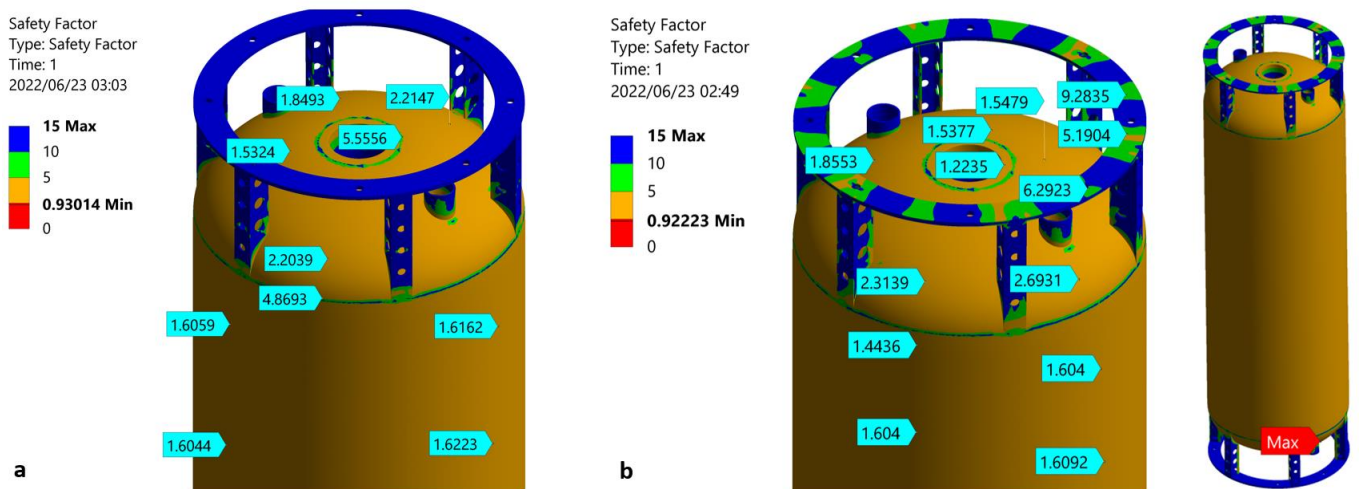


Figure 6-27: Kerosene tank safety factor against internal pressure loading (a) and combined loading (b)

6.6. Tank Buckling

The tank's critical stress for buckling is evaluated theoretically using equations 2-27 and 2-29 for unpressurised and pressurised cases, respectively. The critical stress for unpressurised and pressurised cases was calculated as 724 MPa and 1593 MPa, respectively. The worst-case axial loading occurs during the flight when the tanks are pressurised. From the theoretical results, it is evident that tank pressurisation improves its resistance to buckling. Tank pressurisation to 43.75 bar improves the resistance to buckling by 2.216 times. The high rigidity of the stainless steel also plays a crucial role in improving the critical stress against buckling failure.

The buckling analysis of the propellant tanks was conducted using the ANSYS Workbench software program. This analysis uses the static structural analysis results above as the input, specifically total deformation results. The simulation results showed a maximum total deformation of 1.0 mm at the centre region of the tanks' cylindrical section, as depicted in Figure 6-28. For buckling analysis, the program provides a load multiplier value for all possible failure modes. The load multiplier is similar to a safety factor in this case. The safety factor against buckling was found to be 1.82. Hence, the tanks are deemed safe against buckling failure as the load multiplier is greater than 1.

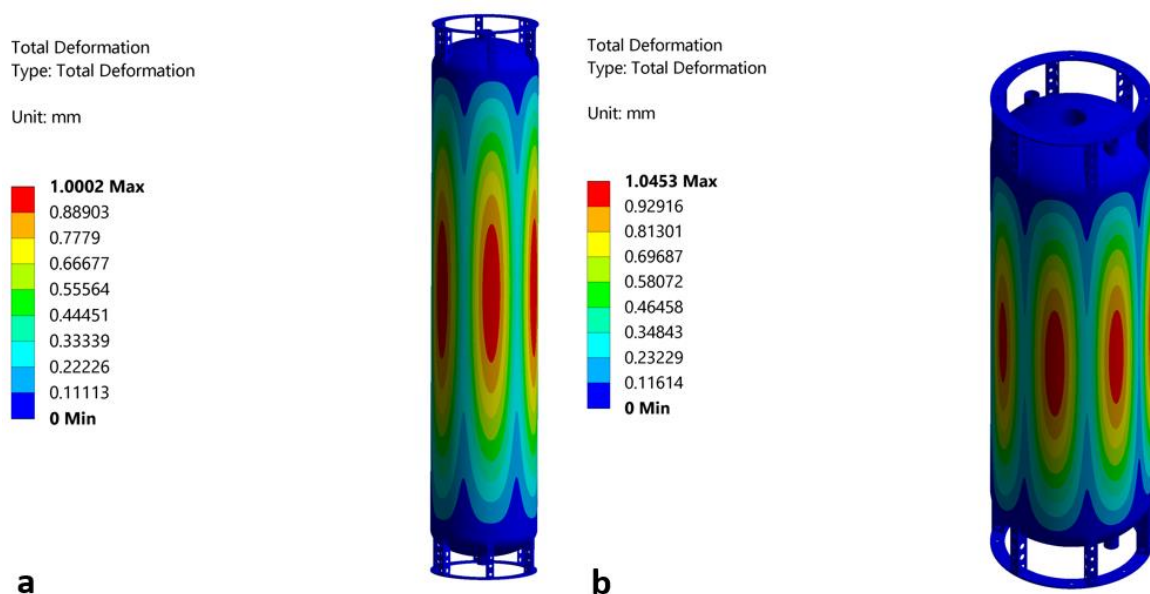


Figure 6-28: Total deformation due to buckling for the LOX (a) and kerosene (b) tanks

6.7. Summary

The final tank design is based upon evaluating the tank's required wall thickness when subjected to flight loads such as aerodynamic and inertial loads. The aerodynamic loads exert lift forces and compressive loading on the vehicle. The propellant tanks must withstand inertial loading, bending moments, and buckling. The minimum weld efficiency of 70 % results in a tank wall thickness of 2 mm. The tanks are joined together by the intertank structure. Its height is subject to the ground equipment system design and the launch gantry.

The tank ports are to be made of 316L SS Swagelok weld fittings. 316L SS is also suitable for operating under cryogenic conditions. An air gap of 18 mm is made to feature between the tunnel pipe in the kerosene tank and the LOX feedline to prevent kerosene from gelling. A solution for anti-sloshing baffles was obtained from experimental data from the literature to mitigate the effect of propellant oscillation due to the vehicle's lateral accelerations during flight.

Propellant oscillations may cause instability of the vehicle hence hampering its performance or even leading to a flight failure. The tank designs call for anti-slosh rings to be placed at 386 mm intervals, having a width and thickness of 40 mm and 2 mm, respectively. Anti-vortexing baffles are incorporated into the tanks to eliminate the gysering effect, which may cause combustion instabilities in the rocket's engine.

From HYROPS simulation results, the kerosene tank experiences the worst inertial loading within 4 s of the flight. The maximum dynamic pressure, acceleration and velocity occur at motor burnout, 31.16 s into the flight. The bending moment and shear force on the vehicle is induced by the angle of attack. A sudden jet stream was assumed to occur at an altitude of 10 km to induce the worst-case angle of attack. This resulted in the worst angle of attack of 2 °. The LOX tank is designed for the inertial and shear load of 9 289 N and 1 469, respectively. In comparison, the kerosene tank is designed for the inertial and shear load of 11 958 N and 3 224 N, respectively.

From the theoretical and FEA results, a tank wall thickness of 2 mm provided a structurally sound propellant tank for welds with a minimum efficiency of 70 %. The kerosene tank is worst-loaded due to the severe inertial loading being imposed upon it. The tunnel pipe in the kerosene tank braces the tank, hence minimising the deformation of the tank. Conversely, the hoop stress's theoretical formulas are invalid as the tunnel pipe causes discontinuity. The pressure vessel theory formulas are not valid for a configuration such as that of the kerosene

tank. Recall these formulas do not predict stress at the attachment points and stress concentration points.

The safety factor in the weld region for a weld efficiency of 70 % is 1.5 and 1.12 on the LOX and kerosene tank, respectively. Since safety factors in both tanks are above the design safety factor of 1.1, a 2 mm wall thickness for the propellant tanks was accepted. Tank pressurisation also improves tank resistance to both bulking and axial compression during flight, and the 301L SS tanks are self-supporting during ground operations. The analytical and FEA results show the propellant tanks to be against buckling failure. The safety factor against buckling was obtained to be 1.82.

7. Propellant Test Tank Manufacture

7.1. Introduction

The manufacture of the propellant test tank aimed to validate the preliminary tank design and welding procedure and subsequently to validate the weld efficiency through pressure testing. It also presented an opportunity to learn about additional considerations related to the manufacturing that should be included in the design phase. For example, thickness reduction during metal spinning requires the starting sheet thickness to be increased slightly more than the design output thickness.

The test tank was evaluated during the testing phase. It was designed to the exact dimensions as the kerosene tank, with a diameter and cylindrical length of 386 mm and 1 000 mm, respectively, except that the tunnel tube was not included. It was made from a 301L SS sheet of 1.5 mm thickness. Different manufacturing techniques were used to construct the tank, including spinning to make the tank end, rolling and welding to make the tank's cylindrical section, and welding to join the tank components.

The tank included six struts and a flange at its lower end, laser cut from 304 SS sheet and then bent using a CNC machine. The tank ports were made from 316L SS and welded to the tank ends. The associated manufacturing drawings are included in appendix III.

7.2. Tank End Spinning

The tank ends were manufactured using the spinning process as it is affordable and suitable for manufacturing small quantities. The manufacturing was performed manually using a non-CNC lathe; hence parameters such as the number of tool passes, the offset of each pass from the other, the tool feed ratio, roller nose radius, and friction cannot be precisely monitored. The geometric accuracy of the resulting tank ends primarily depended on the operator's skill level.

During the process, a 301L stainless steel blank sheet was clamped against a die of the desired shape (elliptical), as illustrated in Figure 7-1. Note that the die in the figure is for different geometry and size. The blank was then plastically deformed by forcing it against the die by the rolling tool. This tool was powered by a hydraulic actuator and controlled by the operator. The lubricant was continuously applied between the rolling tool and the blank sheet. A gauge and visual inspection were used to determine when the process was complete.



Figure 7-1: Spinning process typical setup at Metspin

An image of one of the completed tank ends is shown in Figure 7-2. The difference in a surface finish observed across the external surface is a consequence of the increase in rolling tool force required towards and beyond the knuckle. The different surface finish between the two regions signifies a difference in work hardening rates of the material due to the changing geometry along the tool path. Significant metal thinning and springback occurred in the region, showing higher reflectivity, as depicted in the right-hand side figure.



Figure 7-2: 301L SS test tank elliptical end

It is important to note that the spinning operation needed to be interrupted as the tool approached the knuckle in order for the semi-finished part to be annealed via heat treatment and for the operation to continue without damage occurring in the part. The annealing process's undesirable effect was that the material's original strength and strength gained during the first spin were substantially reduced.

Since the annealing was followed by further spinning, some strength would have been recovered across and beyond the knuckle due to further cold working. Naturally, this would

have significant implications for the structural performance of the tank ends under pressure loading, as a large portion would have significantly reduced yield strength compared to the rest of the tank.

7.2.1. Tank End 3D Scan

Three tank ends were manufactured through the spinning process, and two had to be selected to construct the test tank. The selection criteria applied were the concentricity of each tank end and the dimensional consistency of each potential pair. 3D scanning characterised each tank end's as-built dimensions and geometry. The scanning was performed by the Reinforced and moulded plastics technology station at the Durban University of Technology using a PC-DMIS scanning machine, illustrated in Figure 7-3. The machine was used to measure the surface coordinates along XZ and YZ planes over the interior and exterior of each tank end. After that, interior and exterior surface geometries, shown in Figure 7-4, were generated using these coordinates by employing machine-specific software.

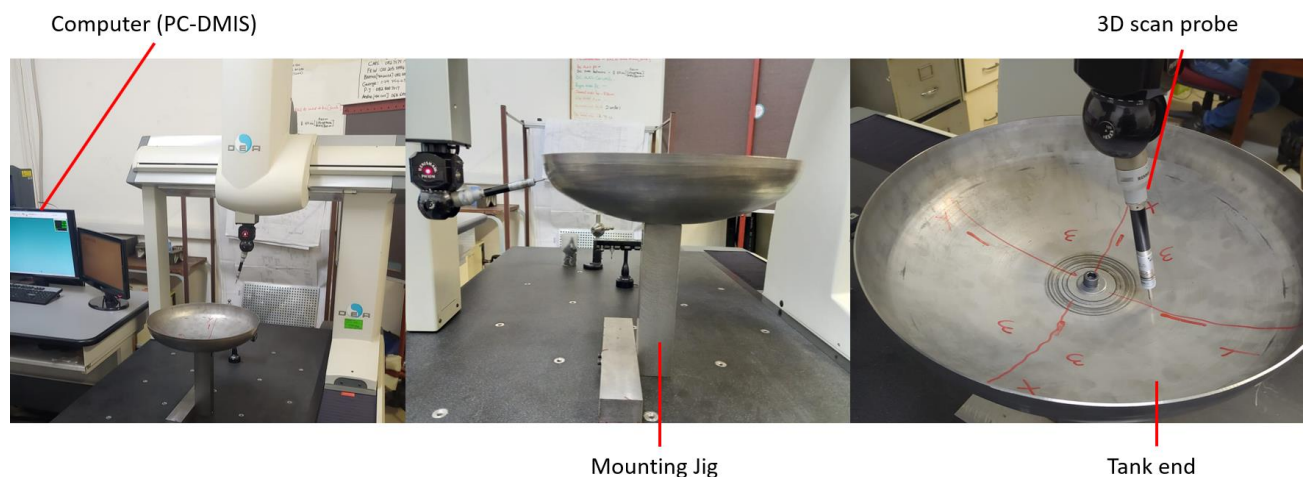


Figure 7-3: PC-DMIS 3D scan setup

The measurement software supports coordinate measuring machines (CMMs), allowing manufactured parts to be measured precisely and accurately. Compared to manual open setup inspections, CMMs can measure parts with improved repeatability and reduced uncertainty (Gopa, 2011). The probe and software program employed can achieve measurement resolution as low as 0.0001 mm. The cross-sectional curves shown in Figure 7-4 were generated by the points recorded at close intervals to capture the geometry of the tank end and thickness.

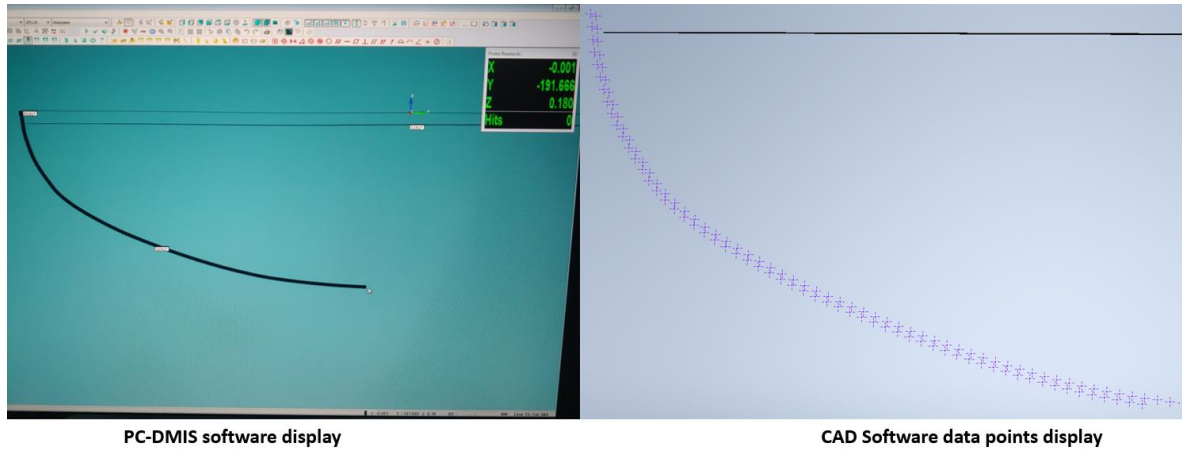


Figure 7-4: Tank end geometry generated by PC-DMIS

The scanning results indicated that tank ends 2 and 3 possessed the highest level of concentricity and dimensional similarity. Key results are presented in Table 7-1, showing the major diameters (inner and outer) in the xz and yz planes for each tank end. These tank ends were subsequently selected to manufacture the propellant test tank.

Table 7-1: Tank Diameter 3D Scan Results

Diameter	Tank End 1	Tank End 2	Tank End 3
Inner (mm)	381.83 / 382.31	383.03 / 382.24	382.68 / 382.98
Outer (mm)	384.45 / 386.23	385.87 / 385.90	385.76 / 386.68

Figure 7-5 and Figure 7-6 further illustrate the measured geometries of each tank end in respect of each measurement plane. Tank ends 2 and 3 were indicated to have better accuracy since their outer curves were found to coincide better than tank end 1. Tank end 1 was spun first; hence the elliptical curve is not uniform, and sectors are not perfectly symmetric. The “Neg” description on Figure 7-5 and Figure 7-6 legends refer to curves that lie in the negative plane. Each tank end plot consists of curves in all four planes to evaluate symmetry.

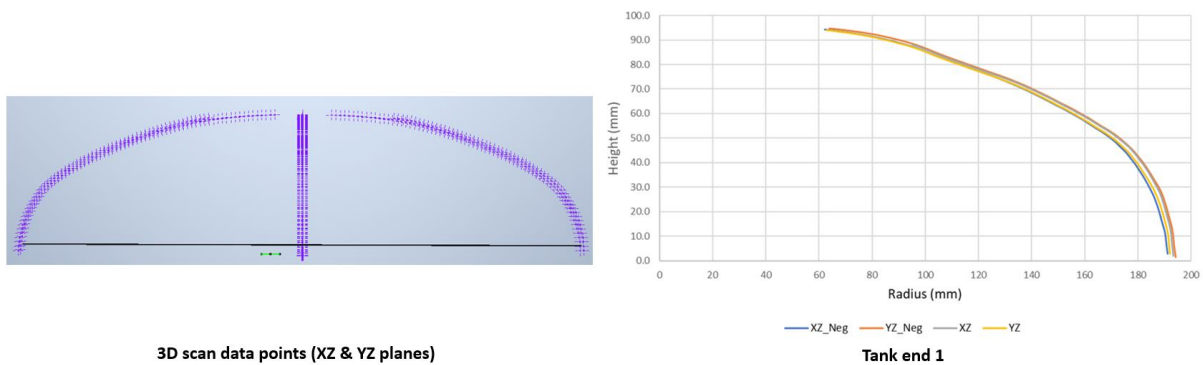


Figure 7-5: 3D scan results for tank 1

The deviation of the tank ends from the spinning mandrel could not be established as the mandrel could not be 3D scanned since 3D scanning was performed at Durban, whereas the spinning mandrel belonged to Metal Spinings (Pty) Ltd based in Randburg, Gauteng.

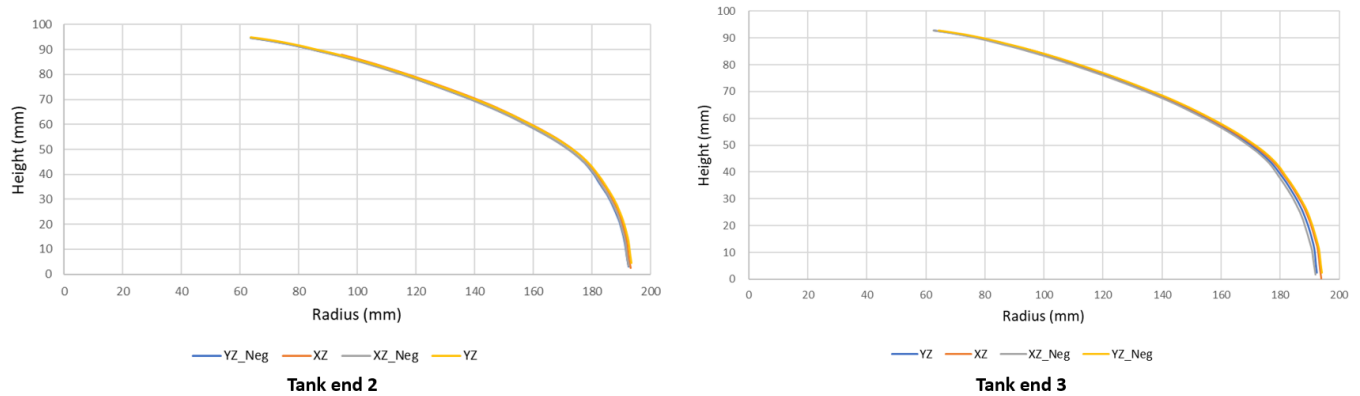


Figure 7-6: 3D scan results for tank end 2 and 3

The work-hardening that would have occurred during the spinning process is due to the corresponding reduction in part thickness as a consequence of plastic deformation. Part thinning was found to be most substantial in the vicinity of the knuckle, as demonstrated in Figure 7-7. The lowest thickness recorded was 1.0452 mm, corresponding to a roughly 30 % reduction in the starting thickness of the blank.

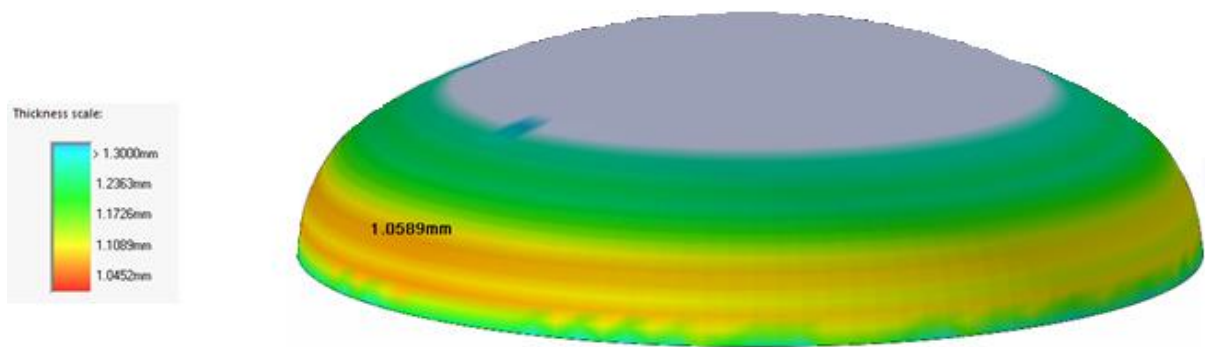


Figure 7-7: 3D scan results for tank end 2

7.3. Tank Cylindrical Section Rolling

The tank's cylindrical section was fabricated through the rolling process, commonly used in the fabrication of pressure vessels, tanks, and other round and hollow structures. Rolling is often performed using a three-roll forming machine and introduces a certain degree of hardening work on the material, although to a lesser extent than spinning.

In the case of the test tank, the rolling diameter was set to 386 mm to ensure dimensional matching with both tank ends. A preliminary rolling trial was conducted on a sheet 500 mm in length to determine if the chosen rolling diameter was compatible with the tank ends. This was done to assess if rolling would produce the desired results. Also, to check if the diameters obtained from 3D scanning were accurate. The cylindrical section which resulted is shown in Figure 7-8.

The test tank's cylindrical section length and diameter were specified to be 1 000 mm and 386 mm, respectively. Following initial rolling, the 1000 mm cylindrical section was observed to exhibit significant springback - seemingly as a consequence of its greater length. The second round of rolling employing larger rollers was subsequently performed to improve the concentricity of the 1 000 mm cylindrical section and eliminated springback.



Figure 7-8: Trial 500 mm cylindrical section

7.4. Tank Strut Laser Cutting and CNC Bending

The tank strut and flange assembly serve as a structure to facilitate coupling with other structures of the STEVE rocket. The struts were manufactured by laser cutting profiles from a 2 mm thick annealed 304 SS sheet, then CNC bending each profile into the desired shape. Struts were laser cut with the lightening holes detailed in the manufacturing drawings attached in appendix III. This process resulted in struts having excellent geometric precision. Associated manufacturing drawings are presented in appendix III.

The flange component incorporated holes for the M10 bolts that are expected to be used to join the tanks to upper and lower structures. It was laser cut from a 5 mm thick annealed 304 SS sheet. The flange and tank struts were then united by welding, as illustrated in Figure 7-9.

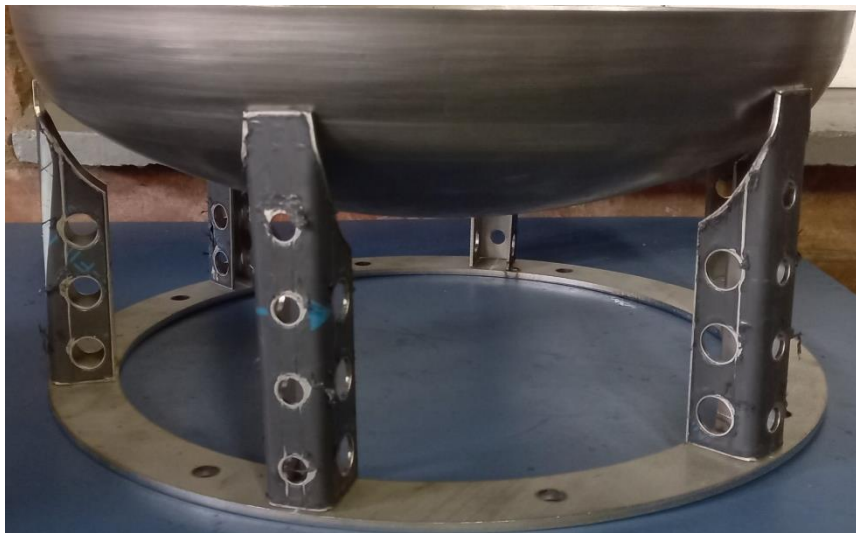


Figure 7-9: Tank skirt/support

As discussed above, these curves were generated from the as-built external tank end surface geometry measured via 3D scanning. This was done to ensure accurate alignment of the tank with the main vehicle axis.

7.5. Tank Welding

The sequence of welding the test tank involved welding the tank's skirt structure and the tank's cylindrical section separately before welding them together. The tank's cylindrical section was tack welded before performing the continuous full penetration weld, as Figure 7-10 illustrates.



Post weld

Tack welds

Figure 7-10: Welding tank's cylindrical section showing post-weld geometry (LHS) and tack welds (RHS)

The tank's cylindrical section was re-rolled following welding to ensure concentricity. The tank ports were to be used to transfer water into and out of the tank during pressure testing and also for pressurisation. These ports were welded into the corresponding tank ends. After that, the bottom tank end was welded to the cylindrical section's lower end, followed by the tank skirt assembly being welded to the bottom tank end. Finally, the top tank end was welded to the upper end of the cylindrical section. The final test tank assembly is presented in Figure 7-11. Tank ports (3) of ½ inch made from 316 SS were procured from Swagelok.



Final welded tank

Top tank ports

Figure 7-11: Test propellant tank showing final construction (LHS) and top tank end (RHS)

The use of low heat input (38 - 40 A) and low welding speed eliminated warpage and distortion of the tank's cylindrical section while resulting in sufficient weld penetration. Argon gas was used to purge the welds to mitigate oxidation. Furthermore, since the final propellant tanks will form integral structures of the vehicle, extensive care was taken in developing a subcomponent joining methodology for the test tank, which would be suitable for future use.

The welds should be checked for any defects present prior to pressure testing the test tank for failure. The radiographic test report is presented in Chapter 8, the propellant tank testing section.

7.6. Summary

The propellant test tank manufacture was based on the preliminary tank design. It formed a crucial step in evaluating the design procedure for stainless steel propellant tanks and eventually evaluating the welds' strength. The test tank structure was manufactured from a half-hard 301L SS sheet of 1.5 mm thickness, with the tank skirt/support structure made from annealed 304 SS. The three ½ inch Swagelok weld fittings purchased to serve as tank ports were supplied in annealed 316 SS. The test tank is the same size as the kerosene tank, except it does not have the tunnel tube.

Tank end spinning introduced several challenges, primarily arising from excessive work-hardening in the knuckle region and the subsequent need for mid-operation annealing of the semi-finished tank end. Hence, large regions of the tank are expected to have suffered significant degradation in yield strength as a consequence of the annealing process. Unfortunately, the extent of this degradation could not be quantified. Of significance, the post-annealing spinning process was found to have resulted in significant part thinning across the knuckle region, with the highest degree of thinning measured to be in the vicinity of 30 %.

The rolling of the 1 000 mm long ½ hard 301L SS sheet presented springback challenges; hence a machine with larger rollers was eventually used. The tank skirt's struts curvature generated post-manufacturing tank end from 3D scan enabled accurate alignment of the test tank. The test tank was welded using low heat (38 – 40 A) input parameters, and no distortion and warpage were observed. Welding using low current eliminated the need for copper backing bars.

Lessons learnt from the manufacture of the test tank indicate that there must be thickness variation in the sections of the final propellant tanks. Due to thickness reduction during metal spinning, the starting thickness of the final tank end blank sheet should be 3 mm for a 2 mm tank wall thickness.

8. Propellant Tank Testing

8.1. Introduction

The test tank was hydrostatically pressure tested to verify its structural integrity, especially with respect to as-built weld strength. Overall, pressure testing of the tank is used to evaluate the adopted propellant tank design procedure as per NASA guidelines (Douglass, et al., 1974). The pressure test procedure is based on ASTM standard E1003 and modified accordingly to achieve the research project objectives. In this section, the tank pressure testing procedure and results are presented. A radiographic test was performed on the longitudinal and circumferential welds to identify other possible causes of tank failure besides the testing pressure.

8.2. Pressure Test Procedure

ND Engineering also facilitated the pressure testing of the propellant test tank in addition to welding the tank. The hydrostatic pressure testing apparatus comprises the pressure relief valve, pressure pump, liquid test medium, pressure hoses and fittings, emergency pressure shut-off valve, and a trapped air valve. Water was used as the testing medium.

The pressure was slowly applied to the fluid until the prescribed pressure was attained. The pressure was held for the required period to locate leaks or early failures. The main objective of this test was to locate the yield point of the tank. Hence, the corresponding tank pressure was estimated on the basis of the yield and tensile strength of the material and the weld's strength.

Using the equation for the equivalent (Von-Mises) stress, equation 8-1 for a biaxial loading case, testing pressures were calculated from equation 8-2 for the following material conditions:

1. Considering the mechanical properties of the ½ hard 301L SS sheet of 1.5 mm thickness and weld strength.
2. Considering the material properties of the ½ hard 301L SS sheet of 1.0 mm thickness and weld strength. The 1.0 mm thickness results from thickness reduction during metal spinning.
3. During tank end spinning, the tank end was subjected to intermediate annealing before the knuckle region was spun. This resulted in the tank end having regions with annealed and work-hardened mechanical properties. Hence, the pressure is computed based on annealed mechanical properties for the 301L SS sheet of 1.00 mm and 1.5 mm thickness.

$$\sigma_e = \sqrt{[\sigma_1^2 + \sigma_2^2 - \sigma_1\sigma_2]} \quad 8-1$$

$$P = \frac{2\sigma_e t}{\sqrt{6}r} \quad 8-2$$

Where σ_e , σ_1 and σ_2 in the above equations are the equivalent, hoop and circumferential stresses, respectively. The calculated testing pressures for the material conditions mentioned above are presented in Table 8-1.

Table 8-1: Hydrostatic testing pressures

Case	Material state	Testing Pressure (bar)	Wall thickness (mm)
1	Yield strength	48.2	1.5
	Weld yield strength	33.8	
	Tensile strength	64.7	
	Weld tensile strength	55.0	
2	Yield strength	32.1	1.0
	Weld yield strength	22.3	
	Tensile strength	43.2	
	Weld tensile strength	36.7	
3	Annealed yield strength	11.6	1.0
	Annealed tensile strength	31.9	
	Annealed yield strength	17.5	1.5
	Annealed tensile strength	47.9	

The above testing pressures were rounded off to the nearest 0.5 bar, and during each test, the pressure was raised at increments of 0.5 bar. ASTM standard, E1003, recommends that the pressure pump be disconnected after reaching the testing pressure to allow the pressure in the system to normalise for about 10 min or at 6 min/cm of the tank thickness. The normalised (holding) time for a tank of 1.5 mm thickness is 54 s. After raising the tank pressure by the test increment, tank pressure was recorded once it was normalised. However, the pressure pump was not disconnected at the working pressure (43.75 bar); instead, the pressure was monitored on the pressure gauge to determine if it had normalised. Based on the material's tensile strength, the maximum pressure for this test was expected to be 65 bar.

The test apparatus included three digital dial gauges to detect deformation on the tank's cylindrical section as well as the top tank end, as illustrated in Figure 8-1. Two measuring tapes were located 100 mm below the top tank end (1) and at the centre of the cylindrical section (2). These measuring tapes were used to evaluate changes in tank circumference.

The two pressure gauges at the bottom and top of the tank ensured verification of the pressure readings.



Figure 8-1: Pressure test setup showing the tank prior to the test (LHS) and during the testing procedure (RHS)

The tank circumference at each test pressure level was measured before and after depressurisation using a measuring tape to detect material yielding in the hoop direction. A dial gauge measurement was taken at a location on the top tank end's exterior surface to record the tank's vertical displacement (1). Two dial gauges (2 and 3) were placed on the cylindrical section to detect the change in diameter. After fully depressurising the tank, the above measurements were re-recorded. This process was repeated for all test pressures accordingly. Once the yielding point had been determined experimentally, the tank was pressurised to failure.

8.3. Pressure Test Results

Based on the material condition cases mentioned in Chapter 8.2, the calculated testing pressures and associated testing results are presented in Table 8-2. Three dial and two measuring tape readings were recorded at each test pressure. That is why there are only two readings of measuring tapes while there are three readings of dial gauges at each test pressure.

Table 8-2: Pressure test results

Test Pressure (bar)	Holding Time (Min)	No.	Dial Gauge Deflection (mm)		Measuring Tape (mm)	
			Pressurised	Depressurised	Pressurised	Depressurised
10.0	2	1	0.57	0.00	1215	1215
		2	0.66	0.09	1216	1216
		3	1.73	0.00		
20.0	2	1	3.55	1.52	1216	1215
		2	3.23	0.73	1217	1216
		3	1.73	0.38		
24.0	2	1	6.49	4.20	1217	1215
		2	5.79	3.76	1218	1216
		3	3.17	1.56		
32.0	2	1	12.95	10.93	1218	1216
		2	9.46	9.50	1218	1216
		3	7.93	3.56		
40.0	10	1	-	-	1218	1216
		2	-	-	1220	1218
44.0	10	1	-	-	1220	1217
		2	-	-	1220	1218
50.0	10	1	-	-	1220	1218
		2	-	-	1222	1220
55.0	10	1	-	-	1222	1220
		2	-	-	1222	1220
57.0	10	1	-	-	1223	1220
		2	-	-	1225	1221
60.0	-	1	-	-	1225	1222
		2	-	-	1225	1223

At the testing pressure of 10 bar, the readings on the dial gauges return to zero deflection after depressurising, showing that yielding has not occurred. Dial gauge (1) is placed at the highest point of the tank end, where the thickness is 1.5 mm. At 20 bar test pressure, dial gauge (1) depicts a permanent deformation of 1.52 mm after depressurising of the tank. As indicated in Table 8-1, the test pressure corresponding to the yield strength of the 301L SS sheet in the annealed condition is 17.5 bar. On this basis, it is clear that the yield strength of the upper tank end was significantly reduced from a work hardened state by the annealing process

employed in its manufacture. Since the lower tank end was manufactured in the same manner, it is expected that it would have exhibited similar behaviour.

From the test pressure of 20 bar onwards, the tank ends were yielding continually. The deformation of 0.73 mm and 0.38 mm on dial gauges 2 and 3 at 20 bar are negligible. This shows that yielding had not occurred as the measuring tapes (1 and 2) still reflected the starting circumference after depressurising. Figure 8-2 shows tank end 1 and tank end 3 post-testing.



Figure 8-2: Tank end 1 and tank end 3 post-test

The final geometry of the tank ends, 3D scanned after pressure testing, is presented in Figure 8-3. Final geometry of the tank end is closer to a torispherical shape than an elliptical one with a maximum height of 131.75 mm. The initial elliptical height was 97.34 mm. This shows that the tank end maximum height was plastically deformed by 34.41 mm at the pressure test of 60 bar. The final geometry shows that the tank end was in the annealed condition as it deformed uniformly.

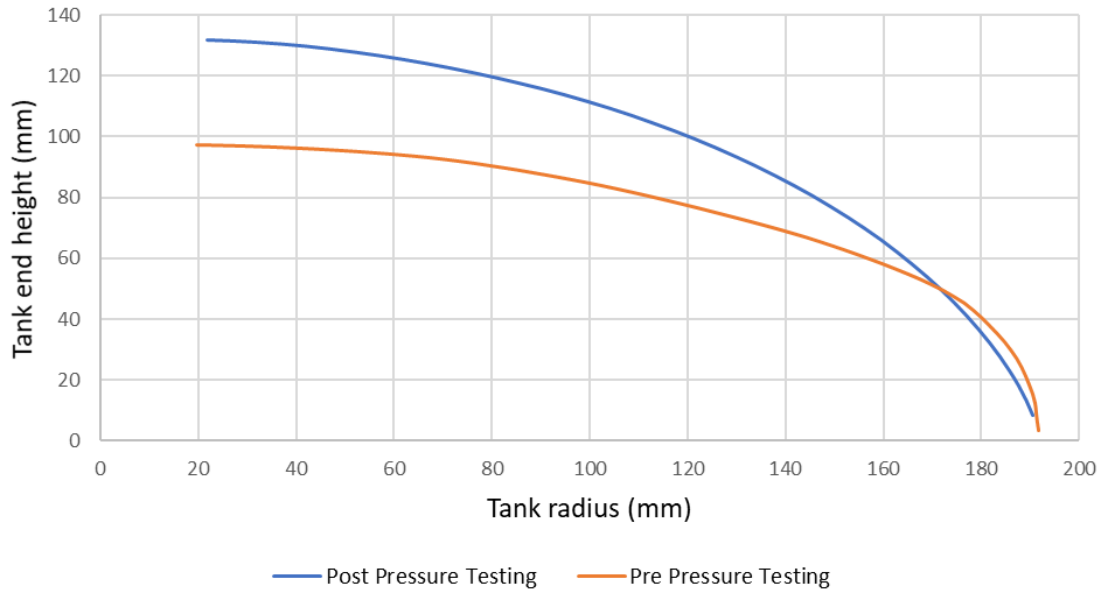


Figure 8-3: Tank end 2 geometry after pressure testing

The yielding of the tank ends at 20 bar shows that the safety factor against the design pressure is 0.45. This safety factor comes as a result of the annealed material condition that exists in the tank ends due to exposing them to annealing temperatures during metal spinning. The test tank was designed based on the ¼ hard mechanical properties, not annealed properties.

The tank was initially tested mounted upon its bottom tank skirt flange, as depicted in Figure 8-1. Since the tank skirt flange was welded to the test stand, this induced a tensional force between the test stand and tank skirt causing the tank to tilt. The tack welds eventually failed, as shown in Figure 8-4. This is why dial gauges 2 and 3 detected deformation more excessively than the measuring tapes from 20 bar test pressure. This tilting effect became evident at the test pressure of 40 bar. Thus, the tank was tested in the horizontal orientation, as shown in Figure 8-5. No dial gauge readings were recorded at this horizontal orientation.



Figure 8-4: Tank skirt flange welded to the test stand

Analytical calculations show that weld starts to yield at a pressure of 33.8 bar for a tank of 1.5 mm thickness. From the pressure test results, the measuring tapes (1 and 2) readings show that the yielding of the cylindrical section starts at the test pressure of 32 bar. At this test pressure, the circumference changed from 1215 mm to 1216 mm.

From 40 bar testing pressure onwards, the time to allow the pressure to normalise was changed from 2 min to 10 min. This was done to account for the fact that the final propellant tanks will be pressurised for the flight duration of 5.3 min. At the test pressure of 44 bar, which corresponds to the tank design pressure of 43.75 bar, the tank's circumference was found to have extended by 2 mm on both measuring tapes.

The test tank eventually failed at 60 bar in the longitudinal weld, as depicted in Figure 8-5. The cylindrical section yielded by 7 mm to the final circumference of 1222 mm at this test pressure. The tank was expected to fail within the longitudinal weld since it is weaker than the circumferential weld based on the pressure vessel theory. Recall from appendix II that the tank's cylindrical section thickness is obtained based on the hoop stress formula and is greater than crown wall thickness and elliptical tank end thickness.



Figure 8-5: Test tank fails on the seam weld

The radiographic test results of the longitudinal weld show a lack of fusion (LOF) at about 710 mm (71 cm) from the bottom tank end. The failure occurred at the centre of the longitudinal weld within the area where the radiographic test detected the lack of fusion. The radiographic test report can be accessed in Figure A-3 of appendix I. The visual inspection shows the heat-affected zone to be shiny compared to the rest of the tank, and thickness variation could be felt from the HAZ to the tank. The weld failure region and heat-affected zone are shown in Figure 8-6.

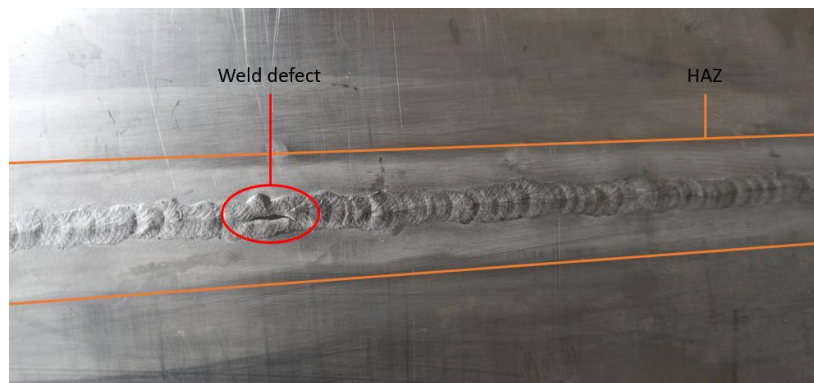


Figure 8-6: Test tank weld failure and heat-affected zone (HAZ)

The tank's cylindrical section yielded at 32 bar, resulting in the weld efficiency of 73 % against the parent material's yield strength. At the same time, failure of the tank at 60 bar results in the weld efficiency of 93 % against the parent material's tensile strength. From the material testing in Chapter 5, the weld efficiency against yield and tensile strengths was found to be 54 % and 76 % when welding using low heat input parameters. A substantial increase in the weld efficiencies shows that the tank is not axially loaded like the tensile test specimens.

The safety factor of the tank's cylindrical section against yield failure at 32 bar is 1.35. In comparison, the safety factor against tensile/ultimate failure is 1.23. Recall that the design safety factor against yield and tensile failure is 1.1 and 1.35, respectively. The seam weld at 60 bar resulted in the safety factor below the recommended value. Overall, the tank's cylindrical section is safe against yield failure.

301L SS strength improves under cryogenic conditions, and ductility is maintained. This means the LOX tank will have a safety factor and weld strength than the kerosene tank.

8.4. Summary

The aim for pressure testing the propellant test tank to destruction was to evaluate the adopted design procedure for metallic tanks as per the NASA guidelines. The critical testing pressures were determined based on the varying mechanical properties of the tank. This included pressure corresponding to the reduced yield and tensile strength at the parent material and weld region. Also, a test pressure relates to the material's anneal strength. All the material conditions cases were evaluated for 1.00 mm and 1.50 mm tank wall thickness.

The tank ends began to deform permanently at 20 bar testing pressure with a deformation of 1.52 mm recorded by a dial gauge. This shows that the $\frac{1}{2}$ hard mechanical properties were lost when the tank end was subjected to the furnace during metal spinning. The resulting safety factor against the design pressure was found to be 0.45. This safety factor below the recommended safety of 1.1 is because the tank was designed based on $\frac{1}{2}$ hard mechanical properties, not annealed properties. This resulted in the tank ends deforming substantially during the pressure test. Subsequently, the final tank end height at 60 bar testing pressure was 131.75 mm from the pre-test height of 97.34 mm

The yielding of the seam weld occurred at 32 bar testing pressure. This results in the weld efficiency and safety factor of 73 % and 1.35 against yield strength. The test tank failed in the seam weld at 60 bar test pressure. The radiographic test results show that failure was initiated by the weld defect caused by the lack of fusion (LOF). The resulting weld efficiency and safety factor against tensile/ultimate strength are 93 % and 1.23, respectively. The tank was designed against yield failure; hence these safety factors are accepted.

9. Conclusion

9.1. Satisfaction of Aims and Objectives

The work reported on in this thesis forms a fundamental element of the Aerospace Systems Research Group's efforts to develop the Suborbital Test Vehicle (STEVE) – its first liquid propellant rocket. To conclude the study, the present chapter evaluates if the research objectives outlined in Chapter 1.2.1 were achieved and to what extent. These objectives are discussed as follows:

- *Develop the design procedure for metallic liquid propellant tanks*

The procedure upon which the STEVE propellant tanks were designed is based on NASA's *Propellant Tank Guidelines* (Douglass, et al., 1974) (Huzel & Huang, 1967). The design input parameters are highly dependent on the properties of the construction materials, both in parent and welded form—the weld efficiency of 301L stainless steel butt weldments needed to be determined.

As outlined in Chapter 5, this was determined experimentally to be 70 % and 81 % with respect to the yield and tensile strength for the high heat-input welding parameters. The low heat-input welding parameters resulted in the weld efficiency of 54 % and 76 % against yield and tensile strength, respectively. The actual weld efficiency enabled the determination of an acceptable tank wall thickness. The proposed design methodology presented in Chapter 3 was deemed suitable for the specific case of STEVE tank development.

- *Generate a suitable design for each propellant tank*

A suitable wall thickness for both 301L stainless steel tanks was found to be 2 mm after establishing the design procedure for the metallic liquid propellant tanks. The weld efficiencies relating to the high heat-input welding parameters were used for the design. Ellipsoidal tank ends were selected based on the spin-forming tooling (mandrel) available to the manufacturer.

As evidenced in Chapter 6, a 2 mm wall thickness is expected to be sufficient for the tank to resist the combined loading anticipated during the flight of the vehicle without plastic deformation. The vehicle's liquid oxygen tank will be positioned above its kerosene tank, with the liquid oxygen feedline passing centrally through the kerosene tank. This configuration improves the vehicle's stability margin and reduces mass by minimising the length of the LOX feedline.

- *Manufacture a test propellant tank*

The test tank was manufactured from the ½ hard 301 stainless sheets of 1.5 mm thickness, as presented in Chapter 7. The tank's major components, which are the tank ends and cylindrical section, were manufactured by spinning and rolling, respectively, prior to being joined by TIG welding. The welding procedure developed in conjunction with the welding and testing service provider ensured a full penetration of high-quality welds, highly dependent on the welder's skill and experience.

Metal spinning required intermediate annealing of the tank ends, resulting in the pre-knuckle surface of the tank ends having annealed mechanical properties. Also, the tank ends were found to have varying thicknesses, with the knuckle region having a thickness of approximately 1 mm. This material thinning made welding the struts to the tank ends' knuckle region challenging, as it posed a risk of pin-holing in the welds.

- *Pressure test the test tank to verify the acceptability of the tank design procedure*

The pressure test was conducted to validate the proposed welding procedure and qualitatively evaluate the performance of the as-built welds. The test also enabled the characterisation of the behaviour of the tank ends when subjected to internal pressure loading. On the basis of pressure vessel theory, the longitudinal seam weld on the cylindrical section of the tank would be subjected to the highest level of stress during the test.

The ultimate failure mode of the tank occurred on the longitudinal weld at a test pressure of approximately 60 bar, which is thus consistent with this expectation. The radiographic test results revealed a lack of fusion (LOF) in the area where the weld failed. The actual safety factor of the weld was found to be 1.35 against the yield failure. This safety factor is about 25 % more than the recommended design safety factor of 1.1. The test further confirmed the presence of annealed material properties in the pre-knuckle region of each tank end, arising from the intermediate annealing stage during the tank end spinning operation. This is based on the fact that the top tank end began yielding at approximately 20 bar below the design pressure of 43.75 bar. The maximum height of the tank end at 60 bar was 131.75 mm from the pre-pressure test height of 97.34 mm.

9.2. Recommendations

The following recommendations concerning critical challenges associated with the design and manufacture of 301 stainless steel rocket propellant tanks are made for further consideration:

Weld efficiency

Considering that low heat-input welding parameters eliminated distortion and warpage of the welds at the expense of the weld efficiency. Hence, further experiments should be conducted to determine the optimum welding parameters, which will result in improved weld efficiency with no distortion or warpage occurring. The heat input resulting from these welding parameters will range between 40 to 80 A (DC).

Laser shock peening should be investigated to improve the weld efficiency of 301 stainless steel weldments. Basically, laser shock peening is a technique where a laser beam is pulsed onto a metal surface. The surface layer is ionized and vaporized by the laser energy, forming a plasma that absorbs the excess laser pulse energy (Ahmad & Fitzpatrick, 2015). Laser shock peening has been used in austenitic stainless steel welds to improve their strength, hardness and fatigue life (Lu, et al., 2020). It has proved to be capable of refining the surface grains and inducing high magnitude residual compressive stress. Refined grains impart ductility in the weld region. Locally, the CSIR's African Laser Centre has performed laser peening for energy and aerospace applications in the past and could be approached in this regard (Tshabalala, 2022).

Metal spinning

- To mitigate the need for intermediate annealing of the tank ends during the spin forming process, it is recommended that they be manufactured from a stainless steel sheet in the annealed condition. In this way, the finished tank ends may possess improved strength, on average, due to the work hardening imparted by the spinning operation itself. Further testing would need to be conducted to establish if the tank ends could be manufactured without annealing.
- Another option would be to manufacture the tank ends using the press forming method. However, the drawback of this approach would be the high tooling cost. However, this disadvantage is somewhat offset by absence of any appreciable thickness reduction or significant springback of the metal sheet compared to metal spinning.
- If the tank end spin forming procedure must include annealing, its impact on material strength could be mitigated by changing the sequence by which the tank skirt is joined to the tank end. In this approach, the tank ends could be welded to the tank's cylindrical

section after spin-formed. The tank could then be hydrostatically pressurised to just above the design pressure, following which the tank skirts could be attached to the tank ends. In this way, plastic deformation that would occur as the tank is pressurised to the designated pressure would not reoccur thereafter, provided that the tank pressure was limited to the design value. Thus, the tank ends could be “stretched” into a stable shape before the tank skirt structure is attached.

Lastly, to cater to the wall thickness reduction in the knuckle region of the tank ends during the spinning process, the tank end blank sheets could be thicker than the sheet from which the tank’s cylindrical section is rolled.

9.3. Future Work

Since the STEVE launch vehicle development process is still in the design phase, other aspects of tank components still need to be finalised as they depend on components and subsystems of the vehicle for which designs have not yet been finalised. These include the following:

Ground support equipment (GSE)

ASReG currently has the ground support equipment for launching hybrid sounding rockets, including the launching platform and the propellant filling and venting systems. These systems, in particular, directly influence the design of the propellant tanks by determining the configuration of the tank propellant and pressurant ports; potential configurations include the use of a single port for pressurisation and venting, a single port for filling or dumping, or separate tank ports for each propellant and pressurant. The requirement for additional ports beyond those considered in this study would have the effect of increasing the number of stress concentrations located on the tank ends and may require a redesign of these elements on each tank. Therefore, the configuration of the tank ports will need to be finalised as the design of the propellant and pressurant handling systems are finalised.

Integration of the propellant tanks to other vehicle’s structures

Although the tank skirt structure was designed to enable the integration of the tanks with the mating structure, no detailed considerations were made to evaluate if the tank skirt structure would be viable with other vehicle components. For example, mounting the engine to the kerosene tank and LOX tank to the upper airframe. This means the tank skirt design will need to be finalised once these structures are designed.

Flight Termination System

During flight tests of high-velocity flight vehicles, such as sounding rockets or launch vehicles, the flight termination system is crucial for range safety. Range safety laws demand that erroneous flights or flights beyond the safety launch footprint be immediately terminated, either by an RF flight termination signal from ground stations or by an autonomous decision-making system onboard (Aktas, et al., 2016). For STEVE, the location of the flight termination's explosive charge on the vehicle will have to be determined. Two potential locations that could be evaluated are 1) within the intertank structure, between the propellant tanks, or 2) above the LOX tank where the roll control system hardware will be positioned.

References

- Ahmad, B. & Fitzpatrick, M. E., 2015. *The Effect of Laser Shock Peening on Hardness and Microstructure in a Welded Marine Steel*, Milton Keynes: The Journal of Engineering.
- Aktas, M., Ertugrul, C. & Karakus, C., 2016. Onboard Flight Termination System with Electronic Safe&Arm Mechanism: A Rapid Solution for High Velocity Flight Vehicles. *European Telemetry and Test Conference*, I(36), pp. 188-195.
- Allen, J., 2021. *Distortion Control - Prevention by Fabrication Techniques*. [Online] Available at: <https://www.twi-global.com/technical-knowledge/job-knowledge/distortion-control-prevention-by-fabrication-techniques-036> [Accessed 18 October 2021].
- ASTM Standard, 2013. *Standard Test Methods for Tension Testing of Metallic Materials*, West Conshohocken: American Society for Testing and Materials International.
- ASTM, 2003. *Standard Specification for Annealed or Cold-Worked Austenitic Stainless Steel Sheet, Strip, Plate, and Flat Bar, A 666 - 03*, West Conshohocken: ASTM International.
- ATI, 2014. *301 Stainless Steel: Austenitic*, Pittsburgh: Allegheny Technologies Inc..
- Balmogim, U., 2017. *Design and Development of the Phoenix-1B Hybrid Rocket*, Durban: University of KwaZulu-Natal.
- Barrowman, J., 1967. *Calculating The Center of Pressure of a Model Rocket*, Phoenix: Centuri.
- Basu, R. I., Kirkhope, K. J. & Srinivasan, J., 1996. *Guidelines for Evaluation of Finite Element and Results*, Washington D.C,: National Technical Service Springfield.
- Berger, E. & Mahlmann, T., 2019. *Ars Technica*. [Online] Available at: <https://arstechnica.com/features/2019/09/after-starship-unveiling-mars-seems-a-little-closer/> [Accessed 7 April 2020].
- Bert, C. W. & Hyler, W. S., 1962. *Design Considerations in Selecting Materials for Large Solid-Propellant Rocket Motor Cases*, Columbus: Battelle Memorial Institute.
- Borogove, R., 2021. *Space Exploration*. [Online] Available at: <https://space.stackexchange.com/questions/10649/what-are-the-criteria-to-put-the-oxygen-tank-above-or-below-the-fuel-tank-for-a/10664> [Accessed 26 June 2021].
- Bowersock, D. C., Gardner, R. W. & Reid, R. C., 1960. Pressurized Transfer of Cryogenic Liquids. *Advances in Cryogenic Engineering*, IV(6), pp. 342-356.
- Boyer, H. E. & Gall, T. L., 1985. *Spinning: Metals Handbook*, Park: American Society for Metals.

- Braeuning, R. A., 2008. *Rocket & Space Technology*. [Online] Available at: <http://www.braeunig.us/space/propel.htm> [Accessed 15 March 2020].
- Broughton, K. M., 2018. *Motor Design for a Suborbital Hybrid Rocket*, Durban: University of KwaZulu-Natal.
- Budynas, R. G. & Nisbett, J. K., 2015. *Shigley's Mechanical Engineering Design*. 10th ed. New York: McGraw-Hill.
- Bullens, D. K., 1949. *Steel and Its Heat Treatment*. 5th ed. New York City: John Wiley & Sons.
- Cerro, J. A., 1996. *A Computer Program to Calculate Running Loads for Integral-Tank Aerospace Vehicle Fuselages*, Hampton: VA: Lockheed Martin Engineering & Science Services.
- Chowdhury, S. M., 2012. *Design and Performance Simulation of a Hybrid Sounding Rocket*, Durban: University of kwaZulu-Natal.
- Christian, J. L. et al., 1963. Compatibility of Metals and Cryogenic Liquids. *Metal Progress*, I(56), pp. 83-100.
- Christian, J. L., Gruner, J. D. & Girton, L. D., 1965. *The Effects of Cold Rolling on the Mechanical Properties of Type 310 Stainless Steel at Room and Cryogenic Temperatures*, Washington DC: General Dynamics.
- Clark, V., 2015. *Modelling of Propellant Management Systems in Early-Phase Launcher Development*, Bremen: 6th European Conference for Aerospace Sciences.
- Cotton, E., 2020. *Starship SN8 | 12.5 Kilometer Hop*. [Online] Available at: <https://everydayastronaut.com/starship-sn8-12-5-kilometer-hop/> [Accessed 18 July 2021].
- Douglass, W., Bailey, M. M. & Wagner, W. A., 1974. *Liquid Rocket Metal Tanks and Tank Components*, Cleveland: NASA.
- Dumont, E., Ludwig, C., Kopp, A. & Sippel, M., 2011. *Advanced TSTO Launch Vehicles*. Bremen, European Conference for Aerospace Sciences.
- El-Khabeery, M. M., Fattouh, M., El-Sheikh, M. N. & Hamed, O. A., 1991. On The Conventional Simple Spinning of Cylindrical Aluminium Cups. *International Journal of Machine Tool and Manufacture*, 31(2), pp. 203-219.
- Fletter, P. R., 1995. *Metal Spinning Tutorial*, Milwaukee: Church Metal.
- Fritz, J., 2020. *Practical Guidelines for the Fabrication of Austenitic Stainless Steels*. 2nd ed. London: International Molybdenum Association.
- Gasparini, 2018. *Stainless Steel fabrication chart*. [Online] Available at: <https://www.gasparini.com/en/blog/stainless-steel-fabrication-chart/> [Accessed 13 August 2021].

GI Metal Spinning, 2019. *Stainless Steel Metal Spinning*. [Online] Available at: <http://www.gimetalspinning.com/stainless-steel-metal-spinning.html> [Accessed 8 August 2021`].

Gopa, K., 2011. *Calibration of CMM Probe Qualification Sphere*, Rochester: Transcat Inc..

Greenfield, S., 1960. Dilution of Cryogenic Liquid Rocket Propellants During Pressurized Transfer. *Advances in Cryogenic Engineering*, III(1), pp. 136-148.

Guo, W. et al., 2015. Microstructure and Mechanical Properties of Laser Welded S960 High Strength Steel. *Materials and Design*, I(1), pp. 534-548.

Gyasi-Agyei, P. K., 2021. *Preliminary Design Considerations for a Liquid Rocket Commercial Launch Vehicle Upper Stage*, Durban: University of KwaZulu-Natal.

Hanson, M. P., 1961. *Smooth and Sharp-Notch Tensile Properties of Cold-Reduced AISI 301 and 304L Stainless Steel Sheet*, Cleveland: NASA.

Hearn, H. C., 1982. Evaluation of Bipropellant Pressurization Concepts for Spacecraft. *AIAA*, 19(4), pp. 320-325.

Hearn, H. C., 1995. Design and Development of a Large Bipropellant Blow-down Propulsion System. *AIAA`*, 11(5), pp. 986-997.

Hedström, P., 2005. *Deformation Induced Martensitic Transformation of Metastable Stainless Steel AISI 301*, Luleå: Luleå University of Technology.

Henson, G. & Jone, C. S., 2018. *Materials for Launch Vehicle Structures*, Westlake: NASA.

Hitchcock, R. B. & Jordan, D. E., 2007. *Guideline for The Welded Fabrication of Nickel-Containing Stainless Steels for Corrosion Resistant Services*, Toronto: Nickel Development Institute.

Hiuhu, J., 2015. *Shear Spinning of Nickelbased Super Alloys and Stainless Steel*, Trollhättan: University West.

Honkawa, D. Y., 2020. *Modular Liquid Propellant Launch Vehicle Design*, Long Beach: California State University.

Hutchinson, V. L., 2004. *Analytical Structural Weight Estimation of Conceptual Launch Vehicle Fuselage Components with the Georgia Tech Structural Tool for Rapid Estimation of Shell Sizes (GT-STRESS)*, Atlanta: Georgia Institute of Technology.

Huzel, D. K. & Huang, D. H., 1967. *Design of Liquid Propellant Rocket Engines*, Washington DC: NASA.

Huzel, D. K. & Huang, D. H., 1967. *Design of Liquid Propellant Rocket Engines*. 1st ed. Washington DC: NASA.

Huzel, D. K. & Huang, D. H., 1992. *Modern Engineering for Design of Liquid-Propellant Rocket Engines*, Reston: American Institute of Aeronautics and Astronautics.

Huzel, D. K. & Huang, D. H., 1992. *Modern Engineering for Design of Liquid-Propellant Rocket Engines*, Reston: AIAA.

INCO, 1962. *Austenitic Chromium-Nickel Stainless Steels at Ambient Temperatures - Mechanical and Physical Properties*, New York City: Nickel Institute.

Kendall, E. G., 1964. *Metals and Alloys for Cryogenic Applications - A Review*, El Segundo: Aerospace Corporation.

Kimzey, J. H., 1970. *Review of Factors Affecting Ignition of Metals in High Pressure Oxygen Systems*, Houston: NASA.

Kotecki, D. & Armao, F., 2003. *Stainless Steels Welding Guide*, Cleveland: The Lincoln Electric Company.

Lange, K., 1985. *Metal Spinning: Handbook of Metal Forming*. 1st ed. Southfield: Society of Manufacturing Engineers.

Lee, J. C. & Ramirez, P., 1975. *Pressurization Systems for Liquid Rockets*, Cleveland: NASA.

Leffler, B., 1996. *Stainless Steels and Their Properties*, Stockholm: Avesta Sheffield AB Research Foundation.

Lepsch, R. A., Stanley, D. O. & Unal, R., 1995. Dual-Fuel Propulsion in Single-Stage Advanced Manned Launch System Vehicle. *Journal of Spacecraft and Rockets*, III(32), pp. 417-425.

Lula, R. A., 1986. *Stainless steel: Metals Park*, Ohio: ASM.

Lu, Z. et al., 2020. *Effect of Laser Shock Peening on Stress Corrosion Sensitivity of 304 Stainless Steel C-ring Weld Specimens*, Bristol: Materials Research Express.

Mann, D. B., 1978. *LNG Materials and Fluids*, Colorado: National Bureau of Standards.

Marshall, G. C., 1969. *Saturn V launch Vehicle Flight Evaluation Report-AS-503 Apollo 8 Mission*, Washington D.C: NASA.

Martinez, I., 2020. *Spacecraft Propulsion*. [Online] Available at: <http://webserver.dmt.upm.es/~isidoro/bk3/c17/Spacecraft%20propulsion.pdf> [Accessed 19 March 2020].

Mazmudar, C. P. & Patel, K., 2014. Effect of Laser Welding process parameters on Mechanical Properties of Stainless Steel-316. *International Journal of Advance Engineering and Research Development*, I(5), pp. 1-11.

McClintock, M. R. & Gibbons, H. P., 1960. *Mechanical Properties of Structural Materials at Low Temperatures*, Washington D.C.: USA National Bureau of Standards Monograph 13.

McHenry, H. I., 1983. The Properties of Austenitic Stainless Steel at Cryogenic Temperatures. In: R. P. Reed, ed. *Austenitic Steels at Low Temperatures*. Colorado: USA National Bureau of Standards, pp. 1-27.

Michael, I., 2009. *Saturn V Stage I (S-IC) Overview*, Houston: NASA.

Miller, 2017. *Tips for Welding Sheet Metal With MIG or TIG*. [Online] Available at: <https://www.millerwelds.com/resources/article-library/successfully-welding->

sheet-metal-with-mig-and-tig

[Accessed 18 September 2021].

Miller, R. P., 1969. *Experimental Bending Strength of an Atlas LV-3C Booster Beyond Compressive Skin Wrinkling*, Cleveland: NASA.

Miniwatts Marketing Group, 2020. *Internet Users Statistics for Africa*. [Online] Available at: <https://www.internetworldstats.com/stats1.htm> [Accessed 23 April 2020].

Morton, B., Elgersma, M. & Playter, R., 1990. *Analysis of Booster Vehicle Slosh Stability During Ascent to Orbit*, Washington D.C.: AIAA.

Moss, D. R., 2004. *Pressure Vessel Design Manual*. 3rd ed. Burlington: Elsevier.

Muraca, R. F. & Whittick, J. S., 1972. *Materials Data Handbook: Stainless Steel Type 301*. 2nd ed. California: NASA.

Newlands, R., Heywood, M. & Lee, A., 2016. *Rocket Vehicle Loads and Airframe Design*, London: Aspire Space.

Nicholson, C., 2019. *Rocket Steel*. [Online] Available at: <https://www.core77.com/posts/91400/Rocket-Steel> [Accessed 7 April 2020].

Nickel Development Institute, 1991. *Design Guidelines for the Selection and Use of Stainless Steel*, Toronto: American Iron and Steel Institute.

Nickel Institute, 2021. *The Nickel Advantage*. [Online] Available at: <https://nickelinstitute.org/about-nickel/stainless-steel/the-nickel-advantage/> [Accessed 31 July 2021].

Niesley, J. E., 1981. *Centaur for the 1980's*, San Diego: The Space Congress Proceedings 4.

Niesley, J. E., 1981. *Centaur for the 1980's*. San Diego, The Space Congress.

Orlianski, Z., 2020. *Fundamentals of laser welding*. [Online] Available at: <https://www.ee.co.za/article/fundamentals-laser-welding.html> [Accessed 5 June 2020].

Pedersen, T., 2019. *Spica Tanks*. [Online] Available at: <https://copenhagensuborbitals.com/spica-tanks/> [Accessed 19 December 2021].

Pérez, J. G., Parks, R. A. & Lazor, D. R., 2012. *Validation of Slosh Model Parameters and Anti-Slosh Baffle Designs of Propellant Tanks by Using Lateral Slosh Testing*, Huntsville: NASA.

Pierre-Jean, C., 2007. *The Welding of Stainless Steels*, Arlon: Euro Inox.

Pinjara, I., 2021. *Procedure for Pressure Test*. [Online] Available at: <https://letsfab.in/hydrotest-procedure/> [Accessed 16 February 2022].

Pocha, J. J., 1986. Propellant Slosh in Spacecraft and How to Live with It. *Aerospace Dynamics*, XX(3), pp. 26-31.

Polyblank, J. A. & Allwood, J. M., 2015. Parametric toolpath design in metal spinning.. *CIRP Annals - Manufacturing Technology*, 64(1), pp. 301-304.

Puhn, F. & Ollusky, J., 1965. *External Design Loads - Operational Centaur Vehicles*, San Diego: General Dynamics Convair Division.

Raina, D. K. & Awasthi, A., 2020. Micro Structure Analysis of TIG Welded HSS 301 Alloy. *International Research Journal of Engineering and Technology (IRJET)*, VII(1), pp. -435.

Read, D. T., McHenry, H. T., Steinmeyer, P. A. & Thomas, R. D., 1980. Metallurgical Factors Affecting the Toughness of 316L SMA Weldments at Cryogenic Temperatures. *Weld Journal*, I(59), pp. 104-113.

Roylance, D., 2001. *Pressure Vessels*, Cambridge: Massachusetts institute of Technology.

Sabbagha, J., 2022. *Conceptual Aerodynamic and Aerostructural Design and Trajectory Prediction for a Single Stage, High Altitude Liquid Rocket*, Durban: University of KwaZulu-Natal.

Sandberg, J. & Laren, M., 2004. *The Avesta Welding Manual*, Avesta: Avesta Welding.

Scroochy, H., 2020. *Starship Compendium*. [Online] Available at: <https://www.elonx.net/super-heavy-starship-compendium/> [Accessed 11 January 2022].

Shanley, F. R., 1960. *Weight-Strength Analysis of Aircraft Structures*. 2nd ed. New York City: Dover Publications.

Slugg, J., 2020. *Preliminary Design of Composite Overwrapped Pressure Vessels for a Suborbital Pressure Fed Liquid Rocket*, Raleigh : North Carolina State University.

Smithsonian, I., 2018. *Looking Closer at the Saturn V*. [Online] Available at: <https://airandspace.si.edu/stories/editorial/looking-closer-saturn-v> [Accessed 14 July 2021].

SpaceX, 2020. *Starship Users Guide*, Chicago: Space Exploration Technologies Corp. .

Sridharan, S., 2018. *ANSYS Workbench 19.2 Updates*, Canonsburg: ANSYS Inc..

Stal, 2018. *Type 301*, Shanghai: Stal Precision Stainless Steel Co..

Stephens, D. G. & Scholl, H. F., 1967. *Effectiveness of Flexible and Rigid Ring Baffles for Damping Liquid Oscillations in Large-scal Cylindrical Tanks*, Washington D.C.: NASA.

Sugar, P., Šugárová, J., Morovič, L. & Zemko, P., 2012. Analysis of Dimensional Accuracy of Spun Parts by Taguchi Approach. *Applied Mechanics and Materials*, 217(1), pp. 2423-2426.

Šugár, P., Šugárová, J. & Petrovič, J., 2016. Analysis of the Effect of Process Parameters on Part Wall Thickness Variation in Conventional Metal Spinning of Cr-Mn Austenitic Stainless Steels. *Journal of Mechanical Engineering*, III(62), pp. 171-178.

Sutton, G. P. & Biblarz, O., 2001. *Rocket Propulsion Elements*. 7th ed. New York City: John Wiley & Sons, Inc..

Sutton, G. P. & Biblarz, O., 2010. *Rocket Propulsion elements*. 8th ed. Hoboken: John Wiley & Sons, Inc..

SVFEW Group, 1967. *Saturn V Launch Vehicle Flight Evaluation Report-AS-503 Apollo 8 Mission*, New York: NASA.

Tam, W. H., Ballinger, I. & Jaekle, D. E., 2006. Conceptual Design of Space Efficient Tanks. *AIAA*, I(42), pp. 1-13.

Technoman, 2011. *Manufacturing Processes - Different Fusion Welding Processes*. [Online] Available at: <https://discover.hubpages.com/technology/Fusion-Welding> [Accessed 31 July 2021].

Tomlinson, L. E. & Keller, R. B., 1973. *Liquid Rocket Regulators, Relief Valves, Check Valves, Burst Disks, and Explosive Valves*, Washington D.C.: NASA.

Tshabalala, L., 2022. *Laser-based Manufacturing Facility*. [Online] Available at: <https://www.csir.co.za/laser-based-manufacturing-facility> [Accessed 23 June 2022].

Wang, L. et al., 2011. Effects of The Roller Feed Ratio on Wrinkling Failure. *Journal of Engineering Manufacture*, 225(11), pp. 1991-2006.

Whipple, T. A. & Kotecki, D. J., 1981. Weld process Study for 316L Stainless Steel Weld Metal for Liquid Helium Service. In: *Materials Studies for Magnetic Fusion Energy Applications at Low Temperatures*. Colorado: USA National Bureau of Standards, pp. 303-321.

Whitwam, R., 2019. *Extreme Tech*. [Online] Available at: <https://www.extremetech.com/extreme/284346-elon-musk-explains-why-the-starship-will-be-stainless-steel> [Accessed 7 April 2020].

Williams, D. R., 2019. *Development of a Composite Oxidiser Tank for The Phoenix - 1B Mk. II Hybrid Rocket*, Durban: University of KwaZulu-Natal.

Wood, A., 2015. *Copenhagen Suborbitals dreams Big with Spica Rocket*. [Online] Available at: <https://newatlas.com/copenhagen-suborbitals-spica-rocket/39004/> [Accessed 19 December 2021].

Wood, J. D., 1961. *Survey on Missile Structural Dynamics*, Los Angeles: Space Technology Laboratories, Inc..

Wunderlin, N., Martin, D., Pitot, J. & Brooks, M., 2021. *Design Options for a South African Small-Satellite Launch Vehicle*, Durban: American Institute of Aeronautics and Astronautics.

Xin, T., Wang, H., Cui, C. & Zhao, J., 2019. An Optimal Design Model for The Wall Thickness of The Propellant Tank. *Journal of Aerospace Engineering*, 11 July, pp. 1-12.

Yang, H. Q., 2015. *Predicting Baffled Propellant Tank Slosh for Spacecraft*. [Online] Available at: <https://www.nas.nasa.gov/SC15/demos/demo12.html> [Accessed 5 January 2022].

Yang, H. Q., Peugeot, J. W. & West, J. S., 2017. *A Computational Fluid Dynamics Study of Swirling Flow Reduction by Using Anti-vortex Baffle*, Grapevine: AIAA.

Yaoyi SS, 2021. *SUS 301 Stainless Steel: The Ultimate Guide*. [Online] Available at: <https://stainlesssteelfoil.com/products/301-stainless-steel/> [Accessed 31 February 2021].

A. Appendix I

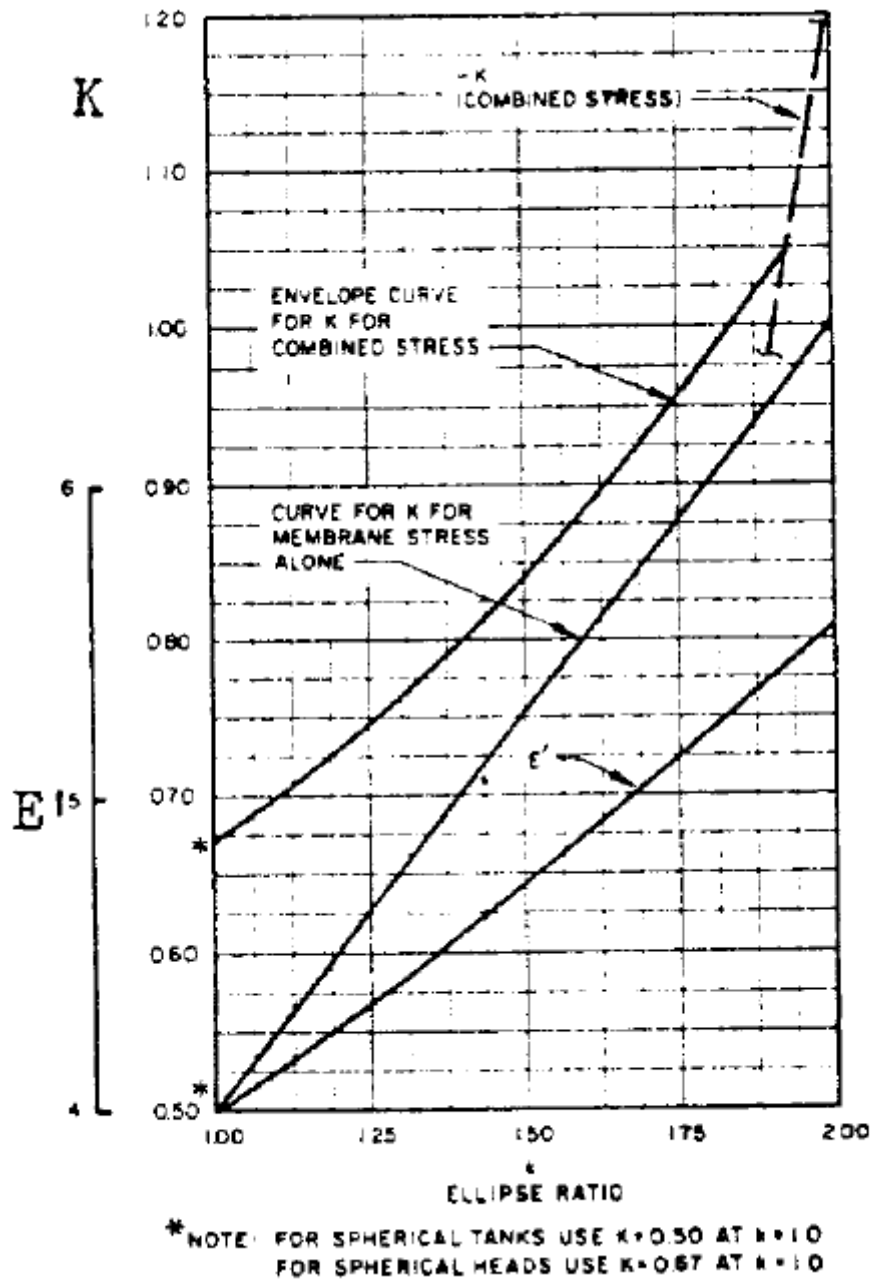


Figure A-1: Ellipse ratio, k versus knuckle stress factor k, compression stress -K and parameter E' (Douglass, et al., 1974)

 COLUMBUS STAINLESS <small>(Pty) Ltd</small> P O Box 133 Middelburg 1050 South Africa Switchboard +27 13 247 9111 Fax +27 13 246 1681 Website: http://www.columbusstainless.co.za A Subsidiary of ACERINOX S.A.		INSPECTION CERTIFICATE 3.1 ACCORDING TO EN 10204															
CERTIFICATE NO 3474998		Rev 1		ISSUE DATE 2021-01-31													
MANUFACTURER'S MARK 		INSPECTOR'S STAMP 		MELTING PROCESS		E/AOD											
CUSTOMER MACSTEEL VRN ROODEKOP 17 BERRY ROAD ROODEKOP South Africa		ORDER No. LP43946		ITEM No. 1		DELIVERY NOTE No. DEL177509											
		CUSTOMER ORDER No. 4501022613/december		PART No. N/A													
		REQUIREMENTS															
SPECIFICATIONS Alatom DTRF150233-C ASTM A666-15		MATERIAL GRADE RSSA301L 301L		CASE MATERIAL MASS QTY PPAS001957 4284042AA10 1084 Kg 28 PPAS002141 4284042AA02A01 1070 Kg 28 PPAS002168 4284042AA01A01 1046 Kg 28 PPAS001954 4284042AA07 1081 Kg 28													
TOLERANCE ASTM A480/A480M				HEAT No. 428404		TYPE											
PRODUCT HT Cold rolled, annealed, descaled followed by a hard temper roll stainless steel sheet				QUANTITY 112		TOTAL MASS 4281 Kg											
DIMENSIONS 1.5 mm x 1330 mm x 2420 mm																	
CHEMICAL COMPOSITION(%)																	
	C	S	P	Mn	Si	Cr	Ni	N									
Min						16.0	6.0										
Max	0.030	0.030	0.045	2.00	1.00	18.0	8.0	0.20									
Heat	0.023	0.003	0.035	1.55	0.42	17.4	6.5	0.11									
MECHANICAL PROPERTIES																	
TEMPERATURE	DIRECTION	POSITION	Rp0.2	Rp1.0	Rm	A50	HRC	HRC max	Bend								
			MPa	MPa	MPa	%	HRC	HRC									
Ambient	Transverse	Requirement	Min	700		1001	22										
			Max	921		1151		36	36								
Ambient	Transverse	Head	748	840	1007	24	35	36	PASS								
		Tail	717	866	1029	25			PASS								
INTERGRANULAR CORROSION			Columbus Stainless (Pty) Ltd. certifies that the analysis and material on this certification is correct and meets the specifications stated. This document is issued without alteration or ensure and may only be reproduced in full. Made and melted in South Africa. This Material is PMI Tested. Visual and dimensional control: no exceptions. The delivery is in accordance with the order. This material is free from mercury contamination. The radition level exhibited by this material is not greater than the normal background level. This material meets the Facsimile requirement of NACE MR0175 / ISO 15156-3 : 2020 & NACE MR0103 / ISO 17945 : 2015 Columbus Stainless is ISO 9001:2015 & ISO 14001:2015 Certified.														
TEST		RESULT															
ASTM A262 Practice E		PASS															

Figure A-2: 301L SS material certificate



GLOBAL NDT & INSPECTION SOUTH AFRICA

Unit 6, Kingfisher Park,
25 Marseilles Crescent
Brairdene, Durban,
4051

P. O. Box 74006
Rochdale Park
Durban, KZN
4034

Office Tel: 031-5632286/2094
Cell: +27 824553924

RADIOGRAPHIC TEST REPORT

TASK NO.: TR-R80JQR **JOB NO.:** 22/2815 **ISSUE DATE:** 2022-02-28 14:04:55 **REVISION:** 0

CLIENT INFORMATION

CLIENT: ND ENGINEERING **MANUFACTURER:** ND ENGINEERING
LOCATION: HAMMARSDALE WORKSHOP **REPORT NO.:** RT-085-22

COMPONENT INFORMATION

TEST PROCEDURE: RT 001 ASME V REV 0 **ACCEPTANCE CRITERIA:** ASME VIII DIV1 2021
COMPONENT DESCRIPTION: LONG WELD
WELDING PROCESS: GTAW **MATERIAL:** SA 106 GRB/SA234
SIZE: N/A **SURFACE TEMPERATURE:** 22 DEG
THICKNESS: 1.2mm **THERMOMETER SERIAL NO.:** 985700147
EQUIPMENT: N/A **DRAWING NO.:** N/A

TECHNIQUE INFORMATION

TECHNIQUE USED: S.W.S.I	IQI TYPE: 10 FEEN	IQI POSITION: SOURCE SIDE
RADIATION SOURCE: IR 192	SOURCE ACTIVITY: 26Ci	SOURCE SERIAL NO.: CO249
DENSITOMETER SERIAL NO.: GD 2591	RADIATION MONITOR SERIAL NO.: 77990	FILM MAKE: FUJI
FILM TYPE: FUJI 50	FILM SIZE: 100mm X 400mm	S.F.D: 114.3mm
EXPOSURE TIME: 30 SEC	INTENSIFYING SCREEN: Pb 0.1mm	HEAT TREATMENT: N/A

TEST REPORT

WELD NO.	W/S	W/P	AREA	RESULT	BZ	DENS	ACC/REJ
LW3	SA	GTAW	0-30	NRD	14	2.7	Accept
.	.	.	30-60	T/INCL 0.5mm , LOF 2mm @71cm	14	2.7	Reject
.	.	.	60-90	NRD	14	2.7	Accept
.	.	.	90-END	NRD	14	2.8	Accept
.
.

Figure A-3: Radiographic test of the longitudinal weld

B. Appendix II

B.1. Tank Design

The analytical design calculations for the LOX tank are shown in this section. The input parameters are presented in Table B-1.

Table B-1: LOX tank design input parameters

Description	Unit	Value
Tank's cylindrical section radius (r)	m	0.1930
Elliptical tank end minor radius (b)	m	0.0965
Tank's cylindrical section length (l_c)	m	1.720
Maximum working/internal pressure (P)	MPa	4.375
301L SS density (ρ)	kg/m ³	8 000
Poisson's ratio (ν)	-	0.290
Weld efficiency (e_w)	%	85.0
301L SS yield strength (S_y)	MPa	760
301L SS tensile strength (S_u)	MPa	1035

Tank design ratios

$$k = \frac{r}{b} = \frac{0.193}{0.0965} = 2$$

$$R = kr = 2 \times 0.193 = 0.386 \text{ m}$$

$$K = 1.00$$

$$E' = 2k + \frac{1}{\sqrt{k^2 - 1}} \ln \frac{k + \sqrt{k^2 - 1}}{k - \sqrt{k^2 - 1}} = (2 \times 2) + \frac{1}{\sqrt{2^2 - 1}} \ln \frac{2 + \sqrt{2^2 - 1}}{2 - \sqrt{2^2 - 1}} = 5.52$$

The maximum working stress

Working stress based on the yield strength:

$$S_w = \frac{S_y}{1.1} = \frac{760}{1.1} = 690.9 \text{ MPa}$$

Working stress based on tensile strength:

$$S_w = \frac{S_u}{1.35} = \frac{1035}{1.35} = 766.7 \text{ MPa}$$

The allowable stress, S_w , is 690.9 MPa.

Tank's wall thicknesses

Cylindrical Tank Section wall thickness:

$$t_c = \frac{Pr}{S_w e_w} = \frac{4.375 \times 0.193}{690.9 \times 0.85} = 1.438 \text{ mm}$$

Knuckle wall thickness:

$$t_k = \frac{KPr}{S_w e_w} = \frac{1.00 \times 4.375 \times 0.193}{690.9 \times 0.85} = 1.438 \text{ mm}$$

Crown wall thickness:

$$t_{cr} = \frac{PR}{2S_w e_w} = \frac{4.375 \times 0.193}{2 \times 690.9 \times 0.85} = 0.719 \text{ mm}$$

Ellipsoidal tank end wall thickness:

$$t_e = \frac{(t_k + t_{cr})}{2} = \frac{\text{Pr} \left(K + \frac{k}{2} \right)}{2S_w} = \frac{4.375 \times 0.193 \left(1.00 + \frac{2.00}{2} \right)}{2 \times 690.9} = 1.222 \text{ mm}$$

Mass of the tank sections

Elliptical tank end:

$$m_e = \frac{\pi r^2 t_e E' \rho}{2k} = \frac{\pi \times 0.193^2 \times 0.001222 \times 5.52 \times 8000}{2 \times 2} = 0.286 \text{ kg}$$

Cylindrical tank section:

$$m_c = 2\pi r l_c t_c \rho = 2\pi \times 0.193 \times 1.720 \times 0.001438 \times 8000 = 7.638 \text{ kg}$$

B.2. Centre of Pressure (COP)

The rocket's stability margin during flight is influenced by the position of the centre of pressure (COP) in relation to the centre of mass (COM) (Barrowman, 1967). For a stable rocket, the position of COP must be aft of the COM measured from the nose cone tip, as illustrated by Figure B-1. The COP of the entire rocket is obtained by determining the COP of individual components such as the nose cone, fuselage, and fins. The CP for STEVE was computed using Missile.com rocket dynamics simulation software.

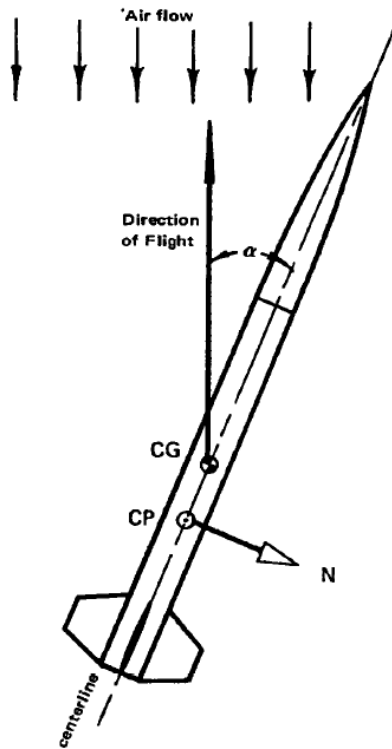


Figure B-1: Rocket's COM (CG) and COP (CP) position during flight (Barrowman, 1967)

Table 1-1 shows CP data for the rocket's body and fins with respect to the angle of attack, alpha generated by Missile.com. The CP values are also given with respect to the rocket's centre of mass and from the nose cone tip. The negative (-) sign on CP shows that CP lies on the aft of the COM.

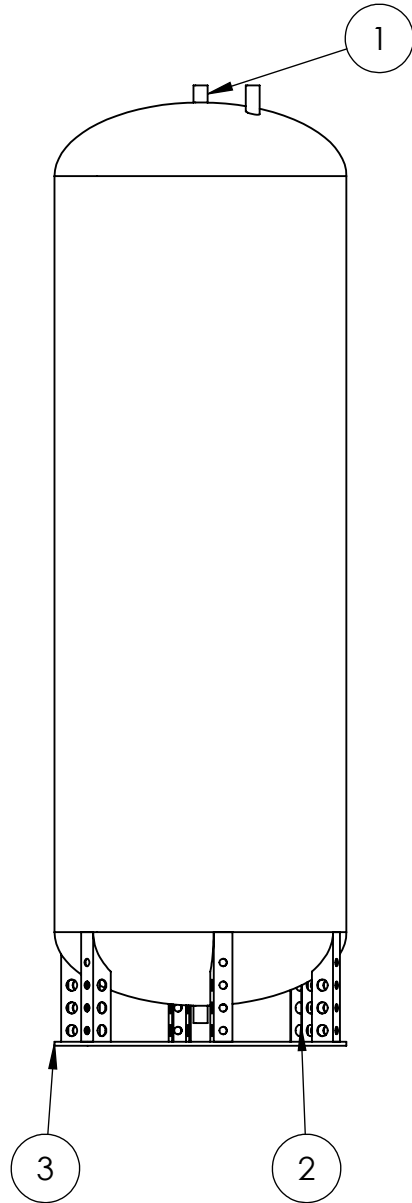
Table B-2: CP Data for STEVE

Alpha	CN	CP (m)	CP from tip (m)	CN_fins	CP_fins (m)	CP_f from tip (m)
0.0	0.0000	0.0000	0.0000	0.0000	0.0000	0.0000
0.5	0.1426	-1.0110	7.0746	0.1053	-2.3602	8.4238
1.0	0.2881	-0.9829	7.0465	0.2102	-2.3601	8.4237
1.5	0.4366	-0.9540	7.0176	0.3146	-2.3601	8.4237
2.0	0.5882	-0.9248	6.9884	0.4185	-2.3597	8.4233
2.5	0.7431	-0.8952	6.9588	0.5217	-2.3601	8.4237
3.0	0.9016	-0.8652	6.9288	0.6245	-2.3598	8.4234
3.5	1.0638	-0.8351	6.8987	0.7266	-2.3600	8.4236
4.0	1.2326	-0.8004	6.8640	0.8283	-2.3599	8.4235
4.5	1.3952	-0.7502	6.8138	0.9182	-2.3598	8.4234
5.0	1.5698	-0.7077	6.7713	1.0129	-2.3598	8.4234
5.5	1.7500	-0.6644	6.7280	1.1061	-2.3599	8.4235
6.0	1.9362	-0.6203	6.6839	1.1977	-2.3599	8.4235

C. Appendix III

Appendix III presents engineering drawings associated with the test tank and final tank designs.

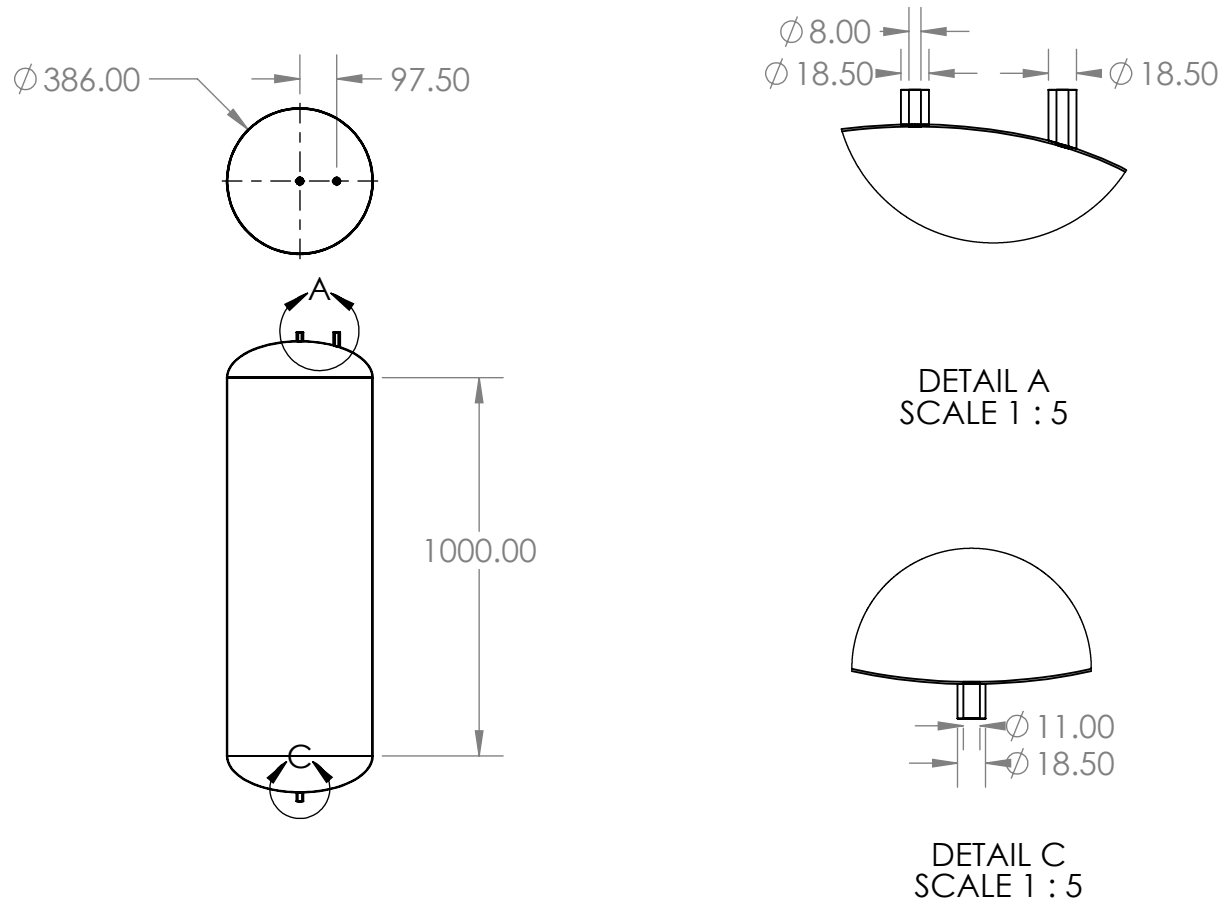
ITEM NO.	PART NUMBER	DESCRIPTION	QTY.
1	Test Tank	AISI 301L	1
2	Tank_Strut	AISI 304	6
3	Tank_Flange	AISI 304	1



UNLESS OTHERWISE
STATED GENERAL
TOLERANCES : ± 0.5 mm
ANGLES : $\pm 1^\circ$

Note: The tank working pressure is 43.75 bar
All tank's components will be supplied by UKZN,
the manufacturer is only responsible for welding.

UNIVERSITY OF KWAZULU-NATAL SCHOOL OF ENGINEERING MECHANICAL ENGINEERING	MAT.: 301L/304	No. REQ.:	SCALE: 1:10	UNITS: mm	PROJECT: Suborbital Test Vehicle, STEVE	No.: 0
		DATE	CHECKED	STUDENT NAME: VULINHLANHLA MCHUNU	TITLE: Test Tank Assembly	
	PROJECT SUPERVISOR			STUDENT No.: 216051647		
	WORKSHOP TECHNICIAN			E-MAIL: mvulinhlanhla@gmail.com		
	TECHNICAL OFFICER			TEL. No.: 072 397 0950		



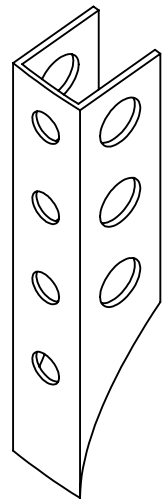
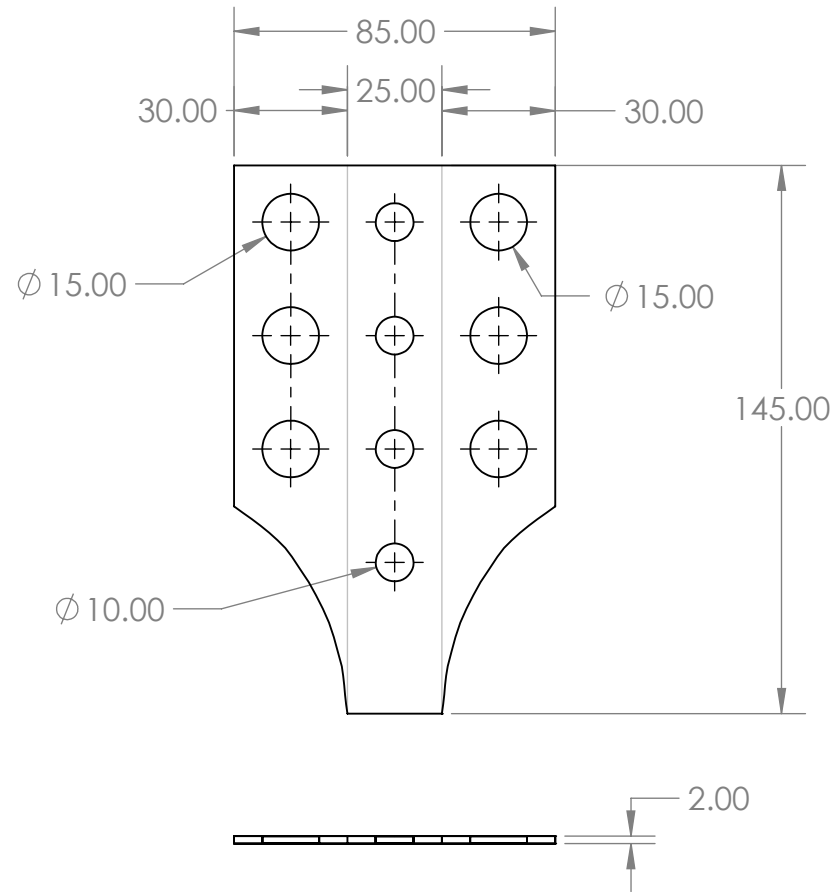
DETAIL A
SCALE 1 : 5

DETAIL C
SCALE 1 : 5

Note: The tank thickness is 1.5 mm
 The working pressure is 43.75 bar
 Tank ports will be supplied by UKZN
 The manufacturer will be responsible for welding

UNLESS OTHERWISE
 STATED GENERAL
 TOLERANCES : ± 0.5 mm
 ANGLES : $\pm 1^\circ$

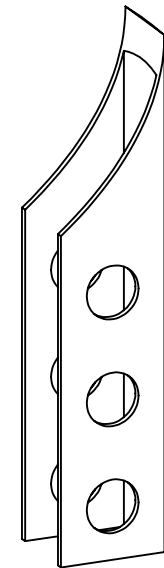
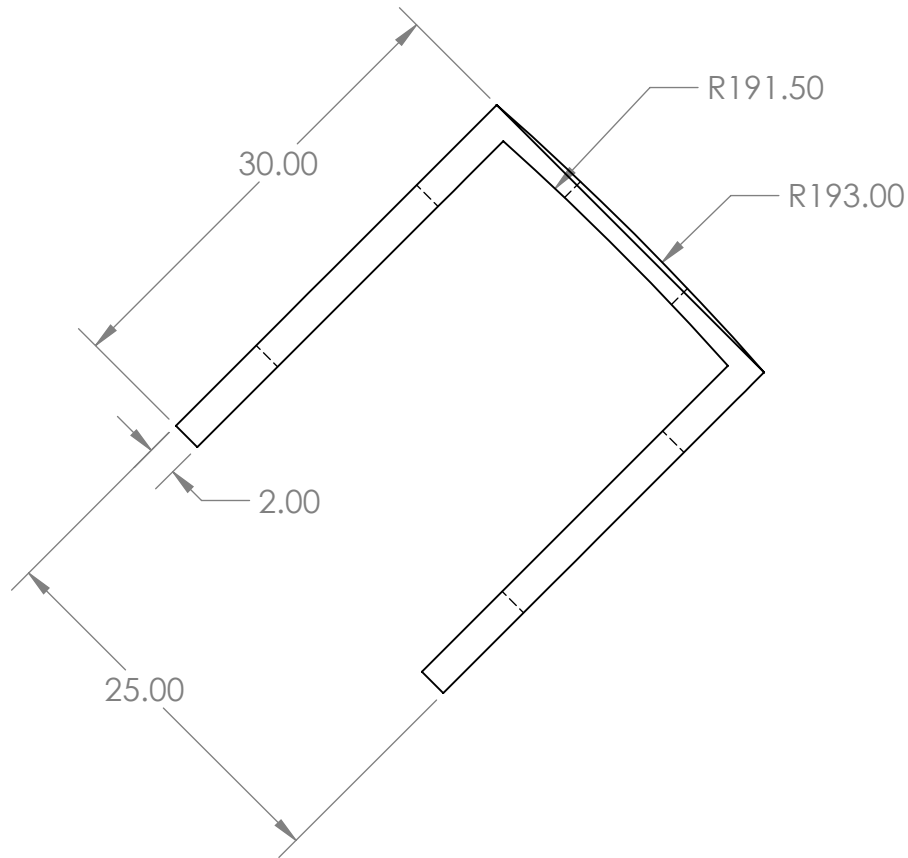
UNIVERSITY OF KWAZULU-NATAL SCHOOL OF ENGINEERING MECHANICAL ENGINEERING	MAT.: 301L SS	No. REQ.: 1	SCALE: 1:20	UNITS: mm	PROJECT: Suborbital Test Vehicle, STEVE	No.: 1
	DATE	CHECKED	STUDENT NAME: VULINHLANHLA MCHUNU			
	PROJECT SUPERVISOR		STUDENT No.: 216051647		TITLE: Test Tank	
	WORKSHOP TECHNICIAN		E-MAIL: mvulinhlanhla@gmail.com			
TECHNICAL OFFICER			TEL. No.: 072 397 0950			



UNLESS OTHERWISE
STATED GENERAL
TOLERANCES : ± 0.5 mm
ANGLES : $\pm 1^\circ$

Note: A 2 mm thick, 304 SS sheet will be laser cut then bent to shape

UNIVERSITY OF KWAZULU-NATAL SCHOOL OF ENGINEERING MECHANICAL ENGINEERING	MAT.: 304 SS	No. REQ.: 6	SCALE: 1:2	UNITS: mm	PROJECT: Suborbital Test Vehicle, STEVE	No.: 2
	DATE	CHECKED	STUDENT NAME: VULINHLANHLA MCHUNU			
	PROJECT SUPERVISOR		STUDENT No.: 216051647		TITLE: Test Tank_Strut	
	WORKSHOP TECHNICIAN		E-MAIL: mvulinhlanhla@gmail.com			
TECHNICAL OFFICER			TEL. No.: 072 397 0950			



UNLESS OTHERWISE
STATED GENERAL
TOLERANCES : ± 0.5 mm
ANGLES : $\pm 1^\circ$

UNIVERSITY OF KWAZULU-NATAL
SCHOOL OF ENGINEERING
MECHANICAL ENGINEERING

MAT.: 304 SS

No. REQ.: 7

SCALE: 2:1

UNITS: mm

PROJECT: Suborbital Test Vehicle,
STEVE

No.:
2-1

PROJECT SUPERVISOR

WORKSHOP TECHNICIAN

TECHNICAL OFFICER

DATE

CHECKED

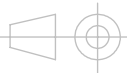
STUDENT NAME: Vulinhlanhla Mchunu

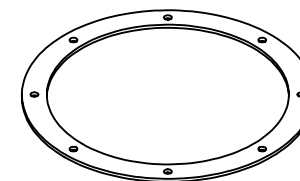
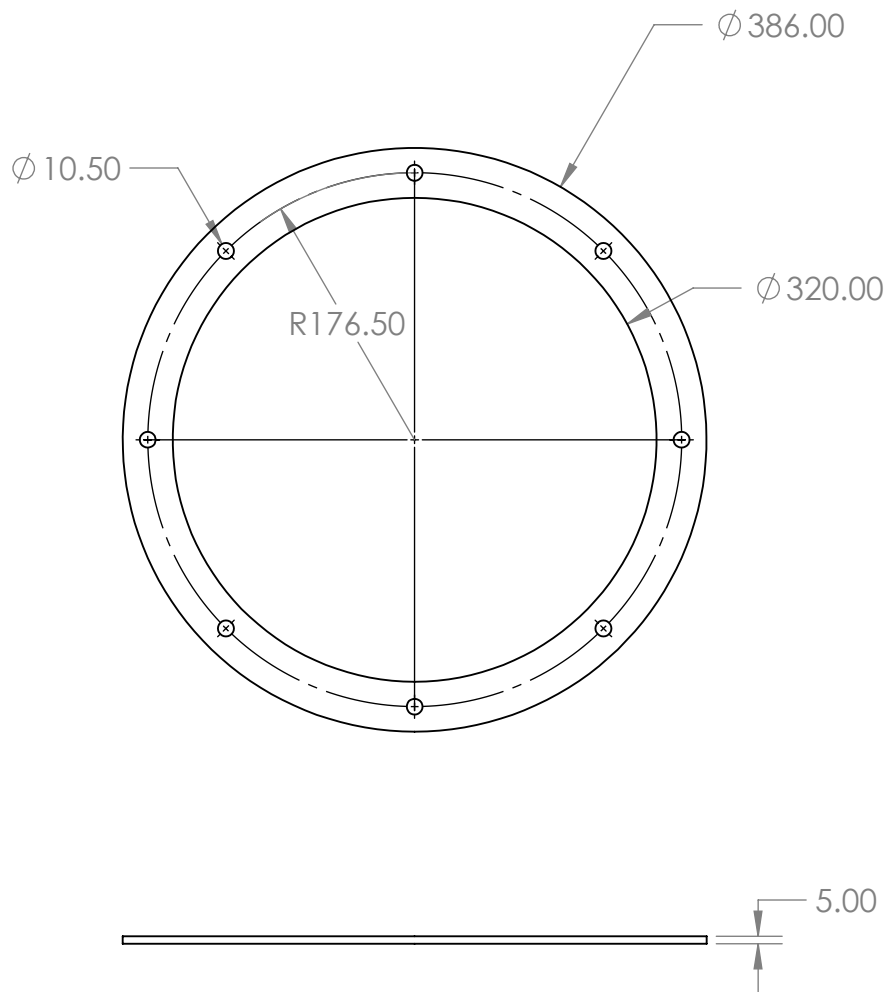
STUDENT No.: 216051647

E-MAIL: mvulinhlanhla@gmail.com

TEL. No.: 072 397 0950

TITLE: Strut Bending





UNLESS OTHERWISE
STATED GENERAL
TOLERANCES : ± 0.5 mm
ANGLES : $\pm 1^\circ$

UNIVERSITY OF KWAZULU-NATAL

SCHOOL OF ENGINEERING

MECHANICAL ENGINEERING

MAT.: 304/316 SS

No. REQ.: 1

SCALE: 1:5

UNITS: mm

PROJECT: Suborbital Test Vehicle,
STEVE

No.:

3

DATE

CHECKED

STUDENT NAME: VULINHLANHLA MCHUNU

PROJECT SUPERVISOR

STUDENT No.: 216051647

WORKSHOP TECHNICIAN

E-MAIL: mvulinhlanhla@gmail.com

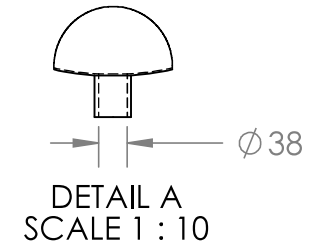
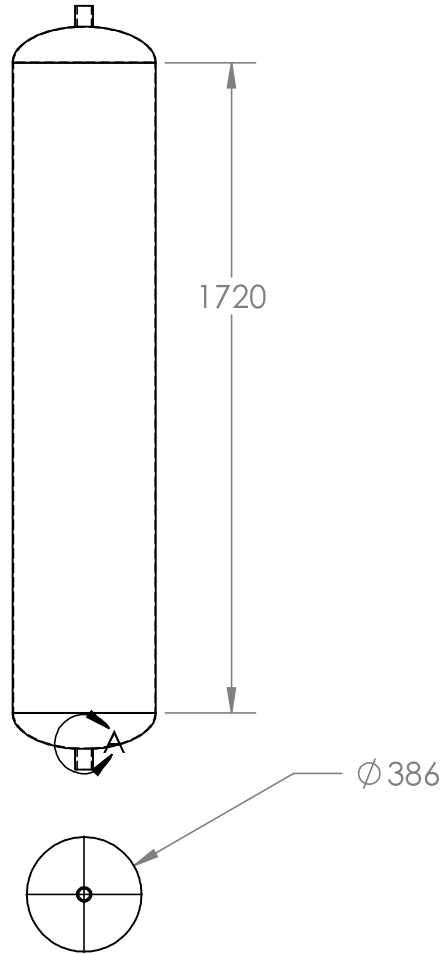
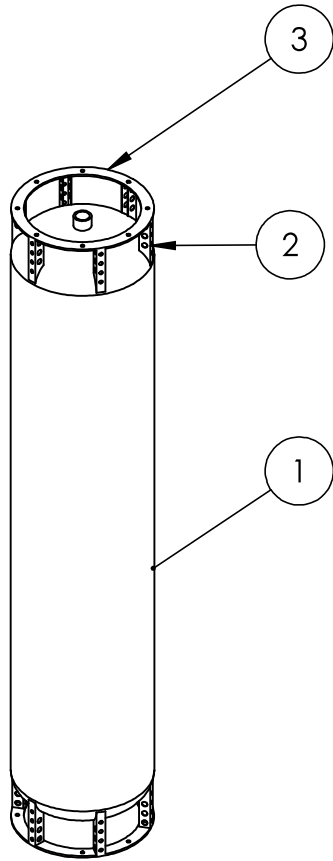
TECHNICAL OFFICER

TEL. No.: 072 397 0950

TITLE: Test Tank_Flange



ITEM NO.	PART NUMBER	DESCRIPTION	QTY.
1	LOX Tant	1/2 hard 301L SS	1
2	Strut	304 SS	12
3	Mating flange	304 SS	2



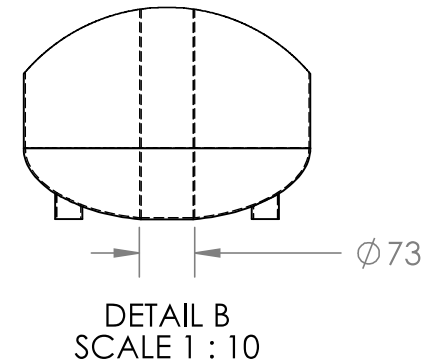
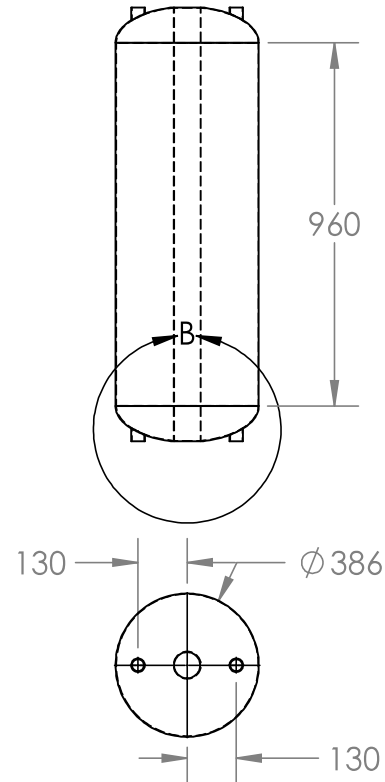
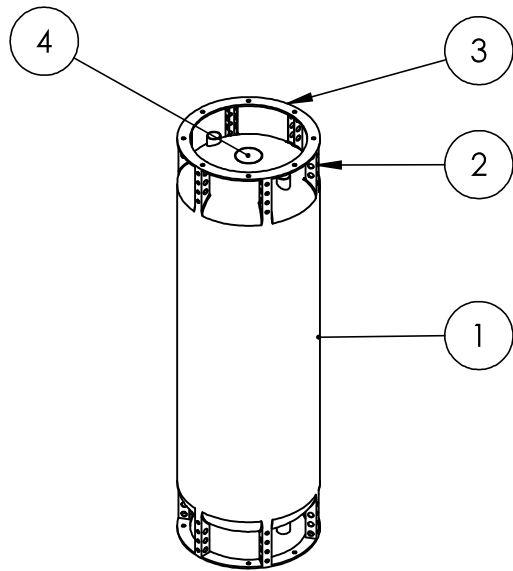
UNLESS OTHERWISE
STATED GENERAL
TOLERANCES : $\pm 0,5$ mm
ANGLES : $\pm 1^\circ$

LOX tank is designed for a 2 mm wall thickness of 1/2 hard 301L SS
The LOX feedline is to be 1.5 inch (38 mm) of 316 SS pipe from Swagelok

UNIVERSITY OF KWAZULU-NATAL SCHOOL OF ENGINEERING MECHANICAL ENGINEERING	MAT.: 301L / 304 / 316 SS	No. REQ.: 1	SCALE: 1:10	UNITS: mm	PROJECT: Suborbital Test Vehicle, STEVE	No.: 4
		DATE	CHECKED	STUDENT NAME: VULINHLANHLA MCHUNU		
		PROJECT SUPERVISOR		STUDENT No.: 216051647	TITLE: LOX Tank	
		WORKSHOP TECHNICIAN		E-MAIL: mvulinhlanhla@gmail.com		
	TECHNICAL OFFICER		TEL. No.: 072 397 0950			



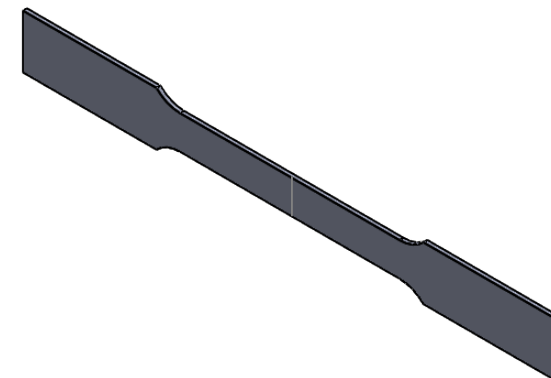
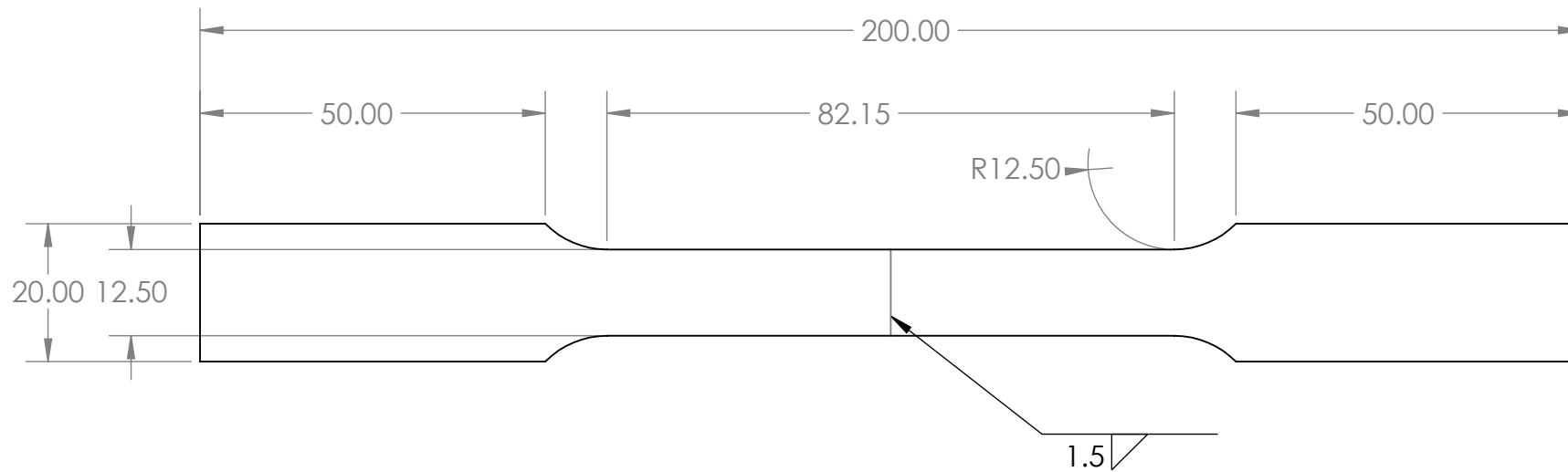
ITEM NO.	PART NUMBER	DESCRIPTION	QTY.
1	Kerosene tank	1/2 hard 301L SS	1
2	Strut	304 SS	12
3	Mating flange	304 SS	2
4	Tunnel pipe	304 SS	1



UNLESS OTHERWISE
STATED GENERAL
TOLERANCES : ± 0.5 mm
ANGLES : $\pm 1^\circ$

The kerosene tank is designed for a 2 mm wall thickness of 1/2 hard 301L SS
The kerosene feedline is to be 1 inch (25 mm) of 316 SS pipe from Swagelok
Whereas, the tunnel pipe is to be 3 inch (73 mm) of 304 SS

UNIVERSITY OF KWAZULU-NATAL SCHOOL OF ENGINEERING MECHANICAL ENGINEERING	MAT.: 301L / 304 / 316 SS	No. REQ.: 1	SCALE: 1:20	UNITS: mm	PROJECT: Suborbital Launch Vehicle, STEVE	No.: 5
	PROJECT SUPERVISOR	DATE	CHECKED	STUDENT NAME: VULINHLANHLA MCHUNU		
	WORKSHOP TECHNICIAN			STUDENT No.: 216051647	TITLE: Kerosene Tank	
	TECHNICAL OFFICER			E-MAIL: mvulinhlanhla@gmail.com TEL. No.: 072 3970 950		



Note: The test specimen thickness is 1.5 mm
 A square butt weld is located at the centre of the specimen
 Two flat sheet pieces must be welded together prior to water-jet cutting

UNLESS OTHERWISE STATED GENERAL TOLERANCES : ± 0.1 mm ANGLES : $\pm 0.5^\circ$

UNIVERSITY OF KWAZULU-NATAL SCHOOL OF ENGINEERING MECHANICAL ENGINEERING	MAT.: 301L SS	No. REQ.: 5	SCALE: 1:1	UNITS: mm	PROJECT: Suborbital Test Vehicle, STEVE	No.: 6
	DATE	CHECKED	STUDENT NAME: Vulinhlanhla Mchunu		TITLE: Tensile Test Specimen_Flat Jaws	
	PROJECT SUPERVISOR		STUDENT No.: 216051647			
	WORKSHOP TECHNICIAN		E-MAIL: mvulinhlanhla@gmail.com			
TECHNICAL OFFICER			TEL. No.: 072 397 0950			